

PL-TR-96-2042

**INVESTIGATIONS IN ATMOSPHERIC DYNAMICS
THROUGH ITS EFFECTS ON DOPPLER-
VELOCITY FLUCTUATIONS IN THE AIRGLOW
STRUCTURE AND ON CRITICAL-LAYER
REFLECTIONS**

**T. F. Tuan
University of Cincinnati
Department of Physics
Cincinnati, OH 45221-0011**

1 February 1996

**Final Report
July 1991-July 1995**

Approved for public release, distribution unlimited

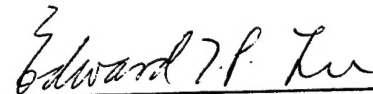


**PHILLIPS LABORATORY
Directorate of Geophysics
AIR FORCE MATERIEL COMMAND
HANSCOM AFB, MA 01731-3010**

19960529 041

DTIC QUALITY INSPECTED 1

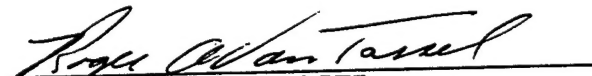
"This technical report has been reviewed and is approved for publication"



EDWARD T.P. LEE
Contract Manager
Simulation Branch



WILLIAM A.M. BLUMBERG
Branch Chief
Simulation Branch



ROGER A. VAN TASSEL
Division Director
Optical Environment Division

This report has been reviewed by the ESC Public Affairs Office (PA) and is releasable to the National Technical Information Service (NTIS).

Qualified requestors may obtain additional copies from the Defense Technical Information Center (DTIC). All other should apply to the National Technical Information Service (NTIS).

If your address has changed, if you wish to be removed from the mailing list, or if the addressee is no longer employed by your organization, please notify PL/IM, 29 Randolph Road, Hanscom AFB, MA 01731-3010. This will assist us in maintaining a current mailing list.

Do not return copies of this report unless contractual obligations or notices on a specific document require that it be returned.

REPORT DOCUMENTATION PAGE			Form Approved OMB No. 0704-0188	
Public reporting burden for this collection of information is estimated to average 1 hour per response, including the time for reviewing instructions, searching existing data sources, gathering and maintaining the data needed, and completing and reviewing the collection of information. Send comments regarding this burden estimate or any other aspect of this collection of information, including suggestions for reducing this burden, to Washington Headquarters Services, Directorate for Information Operations and Reports, 1215 Jefferson Davis Highway, Suite 1204, Arlington, VA 22202-4302, and to the Office of Management and Budget, Paperwork Reduction Project (0704-0188), Washington, DC 20503.				
1. AGENCY USE ONLY (Leave blank)	2. REPORT DATE 1 February 1996	3. REPORT TYPE AND DATES COVERED Final (July 1991-July 1995)		
4. TITLE AND SUBTITLE Investigations in Atmospheric Dynamics Through Its Effects on Doppler-Velocity Fluctuations in the Airglow Structure and on Critical-Layer Reflections		5. FUNDING NUMBERS PE 61102F PR 2310 TA G5 WU AH Contract F19628-91-K-0024		
6. AUTHOR(S) T.F. Tuan				
7. PERFORMING ORGANIZATION NAME(S) AND ADDRESS(ES) University of Cincinnati Department of Physics Cincinnati, OH 45221-0011		8. PERFORMING ORGANIZATION REPORT NUMBER		
9. SPONSORING/MONITORING AGENCY NAME(S) AND ADDRESS(ES) Phillips Laboratory 29 Randolph Road Hanscom AFB, MA 01731-3010 Contract Manager: Edward T.P. Lee/GPOS		10. SPONSORING/MONITORING AGENCY REPORT NUMBER PL-TR-96-2042		
11. SUPPLEMENTARY NOTES				
12a. DISTRIBUTION/AVAILABILITY STATEMENT Approved for public release; distribution unlimited		12b. DISTRIBUTION CODE		
13. ABSTRACT (Maximum 200 words) In this report we investigate: (1) alternative and more direct means of observing gravity waves using optical methods as well as the effects of winds on gravity wave propagation; (2) the effects of gravity-wave critical-layer interactions, and their effects on the nonlinear response of minor species; (3) the guidance of long and short period gravity waves and their implications on some ALOHA data, in particular, the by now well-known and rather unusual "Wall" event. All three investigations are carried out in collaboration with other members of the SOAR program who provide much of the data on which the theoretical analyses are based.				
14. SUBJECT TERMS 3384 Wave and Tides 0310 Airglow and Aurora 3334 Middle Atmosphere Dynamics			15. NUMBER OF PAGES 158	
			16. PRICE CODE	
17. SECURITY CLASSIFICATION OF REPORT Unclassified	18. SECURITY CLASSIFICATION OF THIS PAGE Unclassified	19. SECURITY CLASSIFICATION OF ABSTRACT Unclassified	20. LIMITATION OF ABSTRACT SAR	

CONTENTS

1. Introduction	1
2. Analysis of Air Parcel Motion in the presence of Gravity Waves and Winds; Implications for direct Optical Wave Observations.	8
3. Evidence of Preferential Directions for Gravity Wave Propagation due to Wind Filtering in the Middle Atmosphere	41
4. The Effects of Dissipation on Gravity Waves in the Critical Layer region for Stable and Unstable background Winds; Realistic Background Atmosphere and Winds.	67
5. Application of the Dispersion Formula to Long and Short Period G.W. Modes; Their Transformations among Different Types of Guidance Mechanisms with changing Periods, and comparisons with ALOHA Data	109
6. Nonlinear Response of Minor Atmospheric Species and the OH Emission Layer to Linear Gravity Waves (GW) in presence of Realistic Horizontal Winds; The Effects of Critical Layers on the Response.	136

1 INTRODUCTION

In our original proposal for the 1991 - 1994 period we have suggested three investigations: (1) the investigation of air parcel motion in the presence of gravity waves and winds and the feasibility for making optical wave observations more directly; (2) the directional filtering of gravity waves by critical layers and their effects on the observed airglow wave structure; (3) the analysis of gravity-wave reflections from critical layers by an optical model. All three are part of the SOAR project. (1) involves the University of Western Ontario and the Phillips Laboratories; (2) involves the Utah State University and the Phillips Laboratories whilst (3) primarily involves the Phillips Laboratories and indirectly involves both the University of Western Ontario and the Utah State University.

(1) has been completed and will be submitted for publication pending the supply of further data by a French group; (2) has been published by the Journal of Geophysical Research 98, 6047, (1993); (3) was originally computed for an isothermal atmosphere with simple analytic wind profiles which will not be included in this report. Instead, we are now using more realistic background atmospheres and the wind profiles from NCAR CEDAR Data Base (1990) modified by the tidal winds of Forbes and Vial (1989). We have also extended the scope of our original proposal by using the gravity-wave models, developed originally for part (3), to calculate the OH emission response to a gravity wave in the presence of a critical layer. Both the spatial and the temporal responses have been studied. The horizontal wind has also been found to have a significant effect on the nonlinear response for certain horizontal phase velocities and periods. Above all, the integrated OH airglow emission, a most commonly observed emission in the SOAR program, is found to depend on the direction of gravity wave propagation and this dependence has been analyzed; all this would not occur in the absence of winds. In addition to the above, we have started three new programs: one in partial collaboration with the Utah group; the second is really an extension of the nonlinear perturbation paper of Isler et al(1994) which is still being worked on primarily in collaboration with the Phillips Laboratories; the third deals with both the Utah and the University of Illinois.

The first of these programs deals with computing guided modes which can be used to analyze the short-period middle atmosphere guided modes observed by Taylor et al in the ALOHA

campaign. These are OH and Green line wave structures which appear to cover the entire sky. For example, a period of 4.6 min with a horizontal phase velocity of 75 m/s have been observed and it is almost exactly the same as the theoretically computed guided mode with energy concentrated at 85 to 95 km, a period of 4.6 min and a horizontal phase velocity of 72 m/s. We are now waiting for more results from Utah to analyze. There are reasons to believe that linear wave guidance may not be sufficient to explain these particular observed results. However, there are also basic theoretical questions to answer with respect to partial and full wave-guidance. In general, we have found that (1) all long period guided modes (> 25 min) must be partially guided and that, for fundamental reasons, there are in general far fewer partially guided modes than expected; (2) as the period is shortened the partially guided modes become virtually guided (equivalent to virtual bound states in nuclei, e.g. the Deuteron S-state); (3) as the period is still further lowered, they all become fully guided modes (bound states). For the fully guided modes each pole in the reflection coefficient corresponds to one fully guided mode in contrast to the partially guided modes where only a few poles very close to the real axis contribute significantly to partial wave guidance; the rest just form the general background. The physical reason for this has been explained in a paper by Tuan and Tadic (1982). In that paper, a formula for the G.W. reflection coefficient in terms of all guided and free modes (i.e. a dispersion formula, not to be confused with a dispersion relation) has been derived.

The second of these programs deals with an extension of the nonlinear perturbation paper to include the horizontal winds which do seem to have a strong effect. We have found that the wave-induced vertical drift velocity first found in our original windless paper can be strengthened by wind. The wind has an especially significant effect on the spatial fluctuations as against temporal fluctuations.

The third of these programs deals with the effect of the critical-layer blocking of gravity waves and the apparent anomalous temperature rise in a particular ALOHA event. For once, we do have simultaneously observed meridional and zonal wind profiles, observed gravity wave propagation directions and periods and observed temperature profiles, all at the same Universal times, but covering a total time period of about 7 hours. The problem deals with an inexplicable observed temperature rise over a very narrow

vertical height range (2 km half-width) and time period (about 2-3 hours). The narrow temperature peak subsides slowly after 12:00 UT. The suggestion has been made (Dewan, private communication) that the rather large turbulence immediately below a critical layer can produce a very localized heating resulting in a local temperature rise around the critical layer region and that as soon as the critical layer disappears which it does after 12:00 UT, the temperature peak subsides as indeed it does after 13:00 UT.

All these programs are being worked on but are current and will not be included in this report.

In Section 2 we present our analysis of Air Parcel Motion in the presence of winds and G.W. We have found that (1) the air parcel trajectory in the rest frame depends uniquely on two observable parameters: the period and the horizontal phase velocity; (2) the trajectories are elliptical with so high an eccentricity that they may be considered as straight-line motion for all practical purposes; their inclination to the zenith varies from 35° for a 6 min. period wave with a horizontal phase velocity of 25 m/s to nearly 90° (i.e. nearly horizontal) for a 90 min period wave with a horizontal phase velocity of 150 m/s; (3) the semi-major axis is close to being horizontal for periods above 20 min and is almost independent of horizontal phase velocity. The near straight-line motion offers a convenient method for making direct measurements of G.W. velocities through measuring the Doppler-shifted frequency of airglow produced by the minor species which has the same velocity as the major species. This should be an improvement over studies which analyze G.W. behavior through airglow intensity fluctuations which in turn depends on the minor species density fluctuations; minor species which produce the airglow. The latter fluctuation can be far greater than the major species that carry the G.W. and may even be locally nonlinear with awkwardly varying phase relationship to the G.W. A feasibility study for the more direct velocity observations has been made and recommendations provided.

In Section 3 we analyze the directional filtering of G.W. by critical layers through the construction of blocking diagrams. These diagrams give the areas in which G.W. from a low altitude source is blocked by the critical layers. The G.W. presence was established by the OH airglow observations of M. J. Taylor's group at Utah State. The observation site was located at the Mountain Research Station (40.0°

N, 105.6° W) in Colorado and the observations were made during May, June and July (1988). In the absence of direct wind observation data we use the background zonal winds of Fleming et al. (1988), Fleming and Chandra (1989) and Chandra et al (1990). The meridional background wind components are then taken to be the meridional geostrophic wind computed from the geopotential height (Barnett and Corney (1985). "Geostrophic" is used here to mean steady-state approximation. These background winds are then added to the tidal winds mentioned earlier to provide the resultant zonal and meridional wind profiles. The results show surprisingly good agreement between our theory and Taylor's experiment. There is only one doubtful event when a gravity wave appears to propagate within the forbidden region. Later on, after this was published in J.G.R., we discovered that we need to backtrack the blocking diagrams by a couple of hours in order to take into account the changing wind pattern with time. When this is done, the agreement is total with no exceptions.

Part of the reason that we have succeeded in getting such good agreement at Colorado, even without backtracking, is that at Colorado the wind pattern changes very slowly with time at night. This is not true at Hawaii in the ALOHA Campaign where the wind pattern changes very rapidly so that backtracking becomes very important.

In Section 4 we use realistic background atmosphere and realistic wind profiles for computing the reflection coefficient as a function of G.W. propagation direction and horizontal phase velocity. We have found absorption resonances where the successive valleys correspond to a 2π change in the phase of the wave solution. We also take up the extension of (3) to include the computation of OH emission response to G.W. encountering critical layers. In this project we initially used a simple analytic wind profile, assumed a uniform isothermal background atmosphere and used a constant (i.e. independent of horizontal phase velocity of the G.W.) instability range below the critical layer. In the present computation we use realistic background atmosphere and realistic horizontal winds. We have also extended a theory by Fritts and Geller (1976) for computing the range of the instability region below the critical layer; a range which depends on both the horizontal phase velocity of the G.W. and the wind profile projected along the propagation direction

of the wave. This latter modification changes the reflection coefficient and the G.W. solution rather significantly. The presence of a critical layer within the width of the luminosity profile changes its spatial and integrated temporal response to G.W. quite drastically. We are still in the process of computing the integrated OH airglow intensity. The old calculation for the integrated intensity with isothermal background atmosphere and analytic wind profiles clearly show a considerable dependence on propagation direction of the wave.

Since there should be no such variation with propagation direction if there were no background wind, an analysis of the variation can be used to provide information on the direction and magnitude of the wind at OH height levels. We therefore would like to suggest that simultaneous all-sky camera and photometric airglow measurements be made.

In Section 5 we have obtained one set of the ALOHA data which shows OH and the 557.7 OI green line G.W. patterns that cover almost the entire sky. Furthermore, the wave appears to be guided within a very narrow vertical height range. The one photographic example obtained by Mike Taylor that we have shows that both airglow structures exhibit a period of 4.6 min., and a horizontal phase velocity of 75 m/s. There are reasons to believe that more than a linear guided mode may be involved for this particular set of experiments. Our work would, however, find other applications, since it deals with some basic questions concerning guided modes.

To analyze such short-period guided modes, their relation to the long-period guided modes and the dispersion formula (Tuan and Tadic, (1982)), we computed, using a COSPAR model atmosphere, the poles for the reflection coefficient in the complex k_z -plane. Each pole corresponds to a solution (we use the solution for pressure variation) of the linearized hydrodynamic equations satisfying the radiation boundary condition in the upper atmosphere and the rigid surface condition at the ground level (Reddy, (1969)). We then explicitly constructed the dispersion formula by computing the residues for the poles in addition to the pole positions using the general symmetry properties of the reflection coefficient. The phase shift for the reflection coefficient can then be computed from the dispersion formula and indeed we have found that for long period waves there are only two partially guided modes: the Lamb mode and the S₂ mode. This result is in agreement with Francis' paper (1972). Our

calculation proves explicitly that the number of partially guided modes is much less than the number obtained just from applying the radiation boundary condition to the solutions. A number of papers (Friedman (1966), Midgley and Liemohn (1966) and Reddy (1969)) exist which determine G.W. guidance solely from the radiation condition. In these calculations the number of partially guided modes would be exactly the same as the number of complex poles (rather than purely imaginary poles). However, once we substitute these poles into the dispersion formula, one can easily show that the principal contribution to two occurrences of a relatively sudden phase shift of π in the reflection coefficient come from two particular poles very close to the real axis and that the rest merely contribute to the background in the reflection coefficient. From basic scattering theory a sudden change in the phase of the reflection coefficient by π provides the ultimate criterion for partial wave guidance. Francis (1972) has used and discussed this criterion without explicitly mentioning its connection to scattering theory.

Our next step is to vary the period by shortening it. The complex poles would then migrate to the negative imaginary axis where they can be physically interpreted as virtually guided modes. They then begin to move up the imaginary axis until they form fully guided modes when they arrive at the positive imaginary axis. Many of the poles which did not contribute significantly to partial wave guidance (except to the background), do all, without exception, contribute to full-wave guidance at short periods. This means that overall we get far more fully guided short-period modes than long period partially guided modes. We trace through the journey for the S1 and S2 partially guided modes to determine what kind of fully guided modes they become at short periods.

In Section 6 we extend the OH response to G.W. to include the nonlinear second and third order perturbation terms. We have shown (preprint, (1994)) that the effect of these terms on a windless uniform isothermal atmosphere has already been considered and we have found the possibility of wave-induced diffusion from these higher order terms. We then extend these results to include realistic horizontal winds, but still using an isothermal background atmosphere, to show that the winds can have a strong effect on the higher order terms, both spatially and temporally. Also, the quantitative features of the spatial fluctuations, with the higher order terms included, differ considerably from just the linear

response at different times during a G.W. cycle. Our next step is to consider the effect of a more realistic background atmosphere. We intend to use the multi-layer model so that the basic analytic formulae can be retained for each layer.

2 Analysis of Air Parcel Motion in the presence of Gravity Waves and Winds; implications for direct Optical Wave Observations

1. Introduction

A principal objective of this report is to examine the air parcel motions for gravity waves with wave periods ranging from a few minutes to well over one hour and for horizontal phase speeds ranging from a few meters per sec. to well over one hundred meters per sec. It is well known that fluid trajectories in the presence of waves should be elliptical. Our purpose is to determine quantitatively the dependence of the air parcel trajectory on the gravity wave parameters. We have found that for the overwhelming majority of gravity waves (G.W.) the eccentricities of the elliptical trajectories are so large that the air parcels essentially engage in straight-line oscillations. This behavior is almost independent of the periods which can cover the entire range mentioned above. For gravity waves with periods greater than 20 min. the near straight-line oscillations take place along close to horizontal directions ranging from a zenith angle of 75° to close to 90° . The surprising phenomena is that the above results are almost independent of the horizontal phase speed which can range from 5 m/s to 150 m/s. The aspect ratio is also relatively independent of both the period and the phase speed until we approach the smaller end of the period spectrum for the G.W.

In section 2 we derive the air parcel trajectory for the windless case in terms of the horizontal and vertical displacements. We provide a formula for the aspect ratio and show that it depends only on the G.W. period and the horizontal phase speed. We also show that for most small-scale G.W. phase speeds (5m/s to 150 m/s) the aspect ratio is less than 5%. A formula for the zenith angle of the semi-major axis is derived in terms of the wave period and the phase speed and the results show just how this angle varies with the period and phase speed. We find that not only is the semi-major axis close to being horizontal, but the spread of the zenith angle for vastly different phase speeds (again, 5 m/s to 150 m/s) at a 20-min period is only about 4 degrees; this spread decreases monotonically to about 1 degree at a period of 150 min.

In section 3, we consider our second objective which is to apply some of these findings (in particular the orientation of the near straight line motion) in combination with horizontal winds to obtain a more direct optical measurement of gravity wave motion. We begin by defining a brightness weighted velocity along the line-of-sight. This velocity includes the gravity-wave velocity and the wind velocity and is expressed in terms of the zenith and azimuthal angles of the gravity-wave velocity, the zenith and azimuthal angles of the line of sight and the azimuthal angle of the horizontal wind. We neglect the variation of horizontal wind velocity along the vertical direction since the vertical displacement of the air parcel trajectory is only about 1 km.

The usual optical airglow measurements can be difficult to interpret due to (1) the shifting in the phase of the minor species (which produce the airglow) response from the major species at different height levels and (2) the importance of the nonlinear response, again at certain height levels. Investigations of atmospheric dynamics are often made using typical ground-based instruments such as radars, lidars, photometers and interferometers. In the case of radar and resonance lidar, we observe either microwave reflections or resonant optical scattering as a function of height; the observations allow us to determine the G.W. induced fluctuations at these height levels. Usually the observed fluctuations depend on the fluctuations in some minor species (neutral or charged) density. The same is true in the case of photometers or of optical interferometers except that it is the integrated rather than local minor species density fluctuations that are being observed.

It is well known that range-resolving instruments such as radar or lidar which can be used for observing local fluctuations can often observe far greater minor species density fluctuations at certain locations than any reasonable estimates of the fluctuations in the major species which carry the G.W. This is especially true at the bottom side of a layered structure in the minor species where its concentration gradient is opposite in sign to the major species [1- 5]. It is also well known that the relative phases of the minor and major species density oscillations depend on the relative density gradients of their respective unperturbed profiles varying from 180° out of

phase with each other at the bottom side of a layer to in phase somewhere on the top side. It may also be true, although the point is still being debated, that due to the possible importance of the vertical diffusion of the minor species molecules among the major species, the integrated airglow response to a linear G.W. can contain important non-linear components [6,7] which do not reflect gravity-wave behavior but are strictly a consequence of the response mechanisms.

In contrast to the disparity in density, the particle velocity of the minor species is approximately the same as the particle velocity of the major species. Since the minor species concentration is such a very tiny fraction of the major species concentration, their mutual collision frequency is orders of magnitude greater than the collision frequency of minor species molecules among themselves, [4]. The mean velocities of the minor and major species must therefore be approximately the same. As a result, the measurement of minor species velocity through optical Doppler-shift measurements of airglow can provide immediate information on the velocity field of the G.W. without the need to worry about possible phase difference or non-linearity. In this case, any non-linearity detected would be the non-linearity of the G.W. itself.

In section 4 we present the general discussion. We make a quantitative investigation on the air parcel motions for a wide range

of G.W. and then use some of their common characteristics to look into the possibility of making ground-based Doppler airglow measurements to obtain the velocity of the minor species which produce the airglow. Since, as already mentioned, this velocity is, for all practical purposes, the velocity of the air parcel in the G.W., we can directly obtain the G.W. velocity amplitude and the phase as well as other G.W. properties.

2. Air Parcel Trajectory: Windless Case

We first consider the windless case. The trajectory for air parcel motion in an isothermal atmosphere due to a plane linear monochromatic gravity wave in the absence of winds may be obtained from the horizontal and vertical velocity fields, u and w [8], for steady-state motion. In such a case, the horizontal and vertical displacement fields l and h are related to u and w in the linear approximation by

$$\begin{aligned} u &= i\omega l \\ w &= i\omega h \end{aligned} \tag{1}$$

where ω is the frequency; l and h are functions of x , z , ω and t . Thus, in the linear approximation, at the point $x = \xi$ and $z = \zeta$, the actual trajectory is given by

$$\begin{aligned}x &= \xi + l(\xi, \zeta, \omega, t) \\z &= \zeta + h(\xi, \zeta, \omega, t)\end{aligned}\tag{2}$$

We may, without loss of generality, choose $\xi = 0$. By taking real parts of l and h , we obtain,

$$\begin{aligned}\text{Re } l &= l_o \cos(\omega t - k_z \zeta + \theta_2) \\ \text{Re } h &= h_o \cos(\omega t - k_z \zeta + \theta_1)\end{aligned}\tag{3}$$

where

$$\begin{aligned}l_o &= A k_x k_z c_s^2 (1 + \bar{\eta}^2 / k_z^2)^{1/2} e^{\zeta/2H} \\ h_o &= A k_x^2 c_s^2 \left[1 - \left(\frac{c}{c_s} \right)^2 \right] e^{\zeta/2H} \\ \bar{\eta} &= -\frac{1}{2} \left(\frac{g}{c_s^2} - \frac{\omega_b^2}{g} \right) \\ c &= \frac{\omega}{k_x} = \text{horizontal phase velocity} \\ \theta_1 &= \pi / 2 \\ \theta_2 &= \tan^{-1}(\bar{\eta} / k_z) - \pi / 2\end{aligned}$$

and ω , k_x , k_z , H , c_s , g , ω_b and A have their usual meaning [8]. From (1) h_o/l_o is not only the ratio of the vertical and horizontal

displacements, but also the ratio of the corresponding velocities. By eliminating $\omega t - k_z \zeta$ from (3), we obtain

$$\left(\frac{h}{h_o}\right)^2 - 2\left(\frac{h}{h_o}\right)\left(\frac{l}{l_o}\right)\cos(\theta_1 - \theta_2) + \left(\frac{l}{l_o}\right)^2 = \sin^2(\theta_1 - \theta_2) \quad (4)$$

where now we have set $h = \text{Re } h$ and $l = \text{re } l$. Eq. (4) gives an ellipse in the l - h plane with its center at O and ζ . The geometry is shown in Figure 1, where r_1 , r_2 and $\bar{\alpha}$ are defined to be the semi-major and semi-minor axes and zenith angle of the semi-major axis respectively. Figure (1) is deliberately not drawn to scale to show the geometric parameters more clearly. The ratio of the semi-minor axis, r_2 , to the semi-major axis, r_1 , is given by

$$\frac{r_2}{r_1} = \left\{ \frac{\left[h_o^2 + l_o^2 \right] - \left[h_o^4 + l_o^4 + 2l_o^2 h_o^2 \cos(2 \tan^{-1}(\bar{\eta} / k_z)) \right]^{1/2}}{\left[h_o^2 + l_o^2 \right] + \left[h_o^4 + l_o^4 + 2l_o^2 h_o^2 \cos(2 \tan^{-1}(\bar{\eta} / k_z)) \right]^{1/2}} \right\}^{1/2} \quad (5)$$

For small-scale G.W. for which k_x and k_z are relatively large and $\eta \ll k_z$, (5) becomes

$$\frac{r_2}{r_1} \approx \left(\frac{h_o l_o}{h_o^2 + l_o^2} \right) \left(\frac{\bar{\eta}}{k_z} \right) \quad (6)$$

Thus, since $\eta \ll k_z$, $r_2/r_1 \ll 1$, and the ellipses would appear to be very elongated, becoming a straight line in the hydrostatic limit.

The angle of inclination, $\bar{\alpha}$, of the semi-major axis, r_1 , to the zenith is given by

$$\cos 2\bar{\alpha} = \frac{h_o^2 - l_o^2}{\left[h_o^4 + l_o^4 + 2l_o^2 h_o^2 \cos(2 \tan^{-1}(\bar{\eta} / k_z)) \right]^{1/2}} \quad (7)$$

Again, for $\bar{\eta} \ll k_z$ (small-scale G.W.)

$$\bar{\alpha} \approx \frac{1}{2} \cos^{-1} \left(\frac{h_o^2 - l_o^2}{h_o^2 + l_o^2} \right). \quad (8)$$

It is often more useful to express Eq.(5) in terms of more easily observable parameters such as ω , the frequency, and c , the horizontal phase velocity. By making use of the dispersion relation, we obtain (see Appendix A)

$$\frac{r_2}{r_1} = \left[\frac{1 - \sqrt{1 - B}}{1 + \sqrt{1 - B}} \right]^{1/2} \quad (9)$$

where

$$B = \frac{4 \left(\frac{\omega}{\omega_b} \right)^2 \left(\frac{c}{c_s} \right)^2 \left[\left(\frac{\omega_a}{\omega_b} \right)^2 - 1 \right]}{\left[1 - \left(\frac{\omega}{\omega_b} \right)^2 \left(\frac{c}{c_s} \right)^2 \right]^2}$$

$$\omega_a = \frac{\gamma g}{2c_s} = \text{acoustic cut-off frequency}$$

$$\omega_b = \frac{(\gamma - 1)^{1/2} g}{c_s} = \text{Brunt frequency}$$

In this particular explicit form, we can easily show that for either the long period, or the small scale, or the simultaneous long period and small scale G.W. we obtain:

$$\frac{r_2}{r_1} \approx \left(\frac{\omega}{\omega_b} \right) \left(\frac{c}{c_s} \right) \left[\left(\frac{\omega_a}{\omega_b} \right)^2 - 1 \right]^{1/2} \quad (10)$$

The angle $\bar{\alpha}$ (see Appendix A) is given by

$$\cos 2\bar{\alpha} = \frac{\left(\frac{\omega}{\omega_b}\right)^2 \left[2 - \left(\frac{c}{c_s}\right)^2\right] - 1}{\left\{1 + \left(\frac{\omega}{\omega_b}\right)^2 \left(\frac{c}{c_s}\right)^2 \left[2 - 4\left(\frac{\omega_a}{\omega_b}\right)^2 + \left(\frac{\omega}{\omega_b}\right)^2 \left(\frac{c}{c_s}\right)^2\right]\right\}^{1/2}} \quad (11)$$

For the long period but not necessarily small scale G.W. we obtain:

$$\cos \bar{\alpha} \approx \left(\frac{\omega}{\omega_b}\right) \left\{1 - \left(\frac{c}{c_s}\right)^2 \left(\frac{\omega_a}{\omega_b}\right)^2\right\}^{1/2} \quad (12)$$

and for both long period and small-scale, or small scale but not necessarily long period G.W., we obtain:

$$\cos \bar{\alpha} \approx \left(\frac{\omega}{\omega_b}\right) \quad (13)$$

Figure 2 shows the actual elliptical trajectories at 93 km obtained by evaluating Eq. (3) for different horizontal phase velocities and periods; all drawn to scale for a major species density perturbation of 5% at the same height. The periods range from 6

min. when $\alpha \approx 35^\circ$ to 90 min. when $\alpha \approx 87^\circ$ and the semi-major axis is nearly horizontal. Clearly, for a given wave amplitude the size of the ellipse varies enormously with the period; the longer the period the greater the horizontal displacement of the air parcel. In all cases, the ellipse can be replaced by a straight line trajectory to a good approximation. For the same case α is shown in Figure 3 as a function of period for different G.W. phase velocities. We see that α depends very strongly on the period for short periods up to 30 min. For periods greater than 30 min. $\alpha > 80^\circ$. This implies that for most long period waves the trajectories are close to being horizontal. Clearly, there is very little dependence of α on the phase velocity. Figure 4 shows the ratio of the semi-minor to the semi-major axis, or the aspect ratio of the ellipse, r_2/r_1 . There is more dependence on the phase velocity, but once again there is relatively little dependence on the period above 30 min. The aspect ratio remains less than 4% above 30 min. for widely different phase velocities which again supports the validity of the straight line trajectory approximation.

In Figure 5 we show a schematic diagram (roughly to scale) of the line-of-sight of a ground-based interferometer with a typical field of view (of the order of one degree linear angle). A "footprint" of 1 km is made at a height level of 90 km for zenith observation. With the line-of-sight inclined at 20° to the horizon, the same interferometer makes a footprint of 8 km which is sufficiently short compared with the horizontal wavelengths of the overwhelming

majority of G.W. for us to neglect the variation of the wave fields across the field of view. For this inclination to the horizon, a G.W. with a period of about 30 min would have the semi-major axis of its air parcel trajectory aligned along the line of sight. Owing to the exceedingly high eccentricity of the elliptical trajectories we may consider the air parcel motion as being approximately parallel to the semi-major axis in general and along the line-of-sight for this case in particular.

3. Velocity Measurement and Effect of Background Winds

We begin by defining a brightness weighted velocity, \bar{V}_s , as follows:

let \bar{V}_s = G.W. air parcel velocity

\bar{V}_0 = horizontal wind velocity

$I_0(z)$ = background emission intensity

a brightness weighted velocity along the line of sight may be defined as

$$\begin{aligned}\bar{V}_s &= \frac{\int I_o(z)(\bar{V}_g + \bar{V}_o) \cdot d\bar{r}}{\int I_o(z)dr} \\ &= \frac{\int I_o(z)[\bar{V}_g \cdot \bar{r}_o + (\bar{V}_o \cdot \bar{r}_o)]}{\int I_o(z)dr}\end{aligned}\tag{14}$$

where $\bar{r} = \bar{r}_o r$ = vector distance along the line of sight with \bar{r}_o as a unit vector.

If $I_o(z)$ has a narrow sharp profile with a peak at z_0 and a half width much less than the vertical wave length, the real brightness weighted velocity becomes

$$\text{Re } \bar{V}_s \approx \text{Re } \bar{V}_g(z_0) \cdot \bar{r}_o + \bar{V}_o(z_0) \cdot \bar{r}_o\tag{15}$$

More detailed geometry is shown in Figure 6. Here the spherical polar coordinates θ & ϕ denote the line-of-sight direction and θ_g and ϕ_g denote the orientation of the assumed straight line trajectory of the G.W. air parcel.

$$\text{Re } \bar{V}_g \cdot \bar{r}_o = |\text{Re } V_g| [\cos \theta \cos \theta_g + \sin \theta \sin \theta_g \cos(\phi - \phi_g)]\tag{16}$$

Similarly, if θ_o & ϕ_o are the angles for the direction of the wind, and setting $\theta_o = 90^\circ$ for the horizontal wind, we have

$$\begin{aligned}
(\text{Re } \vec{V}_g + \vec{V}_o) \cdot \vec{r}_o = & |\text{Re } \vec{V}_g(t)| [\cos \theta \cos \theta_g + \sin \theta \sin \theta_g \cos(\phi - \phi_g)] \\
& + V_o [\sin \theta \cos(\phi - \phi_o)]
\end{aligned} \tag{17}$$

In Figure 7 we show the horizontally projected view of the line of sight, the direction of propagation relative to the wind and to the ground observer and the horizontal wind direction. The azimuthal angles are all taken with respect to the eastward direction.

The radial velocity, V_S , consists of a constant part due to the background wind and a fluctuating part due to the projection of the gravity wave motion along the line-of-sight (Figure 8). The quantities that are usually measured are: the brightness-weighted velocity, V_S ; the frequency, ω ; and the polar and azimuthal angles of the line of sight, θ and ϕ . The wind parameters, V_o and ϕ_o , are often unknown. There are two approaches for determining V_g , the fluctuating air parcel velocity.

In the first approach, we can use wind profile climatological models [9,10] for most mid-latitude locations at different hours of the night. Knowing V_o and ϕ_o , the only unknowns in (17) are V_g and ϕ_g . Since ϕ_g may be assumed a constant and V_g is oscillating, we may easily determine both by using (17) and the observed V_S , (see Figure 7).

In the second approach, we make use of the fact that V_o and ϕ_o may well be slowly varying functions of time as compared with V_g .

We may then use (17) and the observed fluctuating V_S and subtract away any

slowly varying background which may be attributed to the wind. The remainder would again contain only V_g and ϕ_g as unknowns and both may be readily determined from the subtracted V_S and (17), (without the wind terms).

In Fig. 7 we show the horizontally projected view of the line of sight, the direction of propagation relative to the wind and to the ground observer and the horizontal wind motion. The azimuthal angles are all taken with respect to the Eastern direction.

4. Discussion

The purpose of the present paper is to show that, since the minor species velocity is approximately the same as the velocity of the major species, a direct measurement of the Doppler-shifted airglow emission from the minor species with a suitably chosen optical interferometer can immediately yield information on the gravity wave velocity field. The results are not subject to the uncertainties associated with airglow brightness measurements due to the phase variations and phase difference between the minor and the major species that a density measurement would bring. Neither would Doppler velocity measurements be subject to the nonlinearities that can occur in the minor species density fluctuations.

The magnitude of the velocity field which ranges from 5 to 15 m/sec for the G.W. considered is well within the capabilities of the optical airglow instruments described below. One of the main observational difficulties lies in the selection of an observation site which would allow low observation angles to take advantage of the elongated trajectories for the longer period waves. Another difficulty comes from the background wind. However, if the winds do not vary too greatly over a period of the G.W., the problem of isolating the G.W. fluctuations from the background wind should not be too serious.

The direct detection and observation of the particle velocity described above impose rigid requirements on the instrument to be used and the operational approach employed. For the range of particle motions likely to occur, the particle trajectories are essentially narrow ellipses whose major axes are oriented at small angles to the horizontal as illustrated in Figure 2.

The basic requirement for the instrument is that it be capable of measuring velocities along the line-of-sight as small as a few meters per second. Several instruments have been described with this capability. All have inherently the narrow fields-of-view required for this type of measurement.

The Fabry-Perot interferometer (FPI) has been used for many years for the measurement of winds. Hernandez [11] has reviewed the use of the FPI and recent measurements have been described by

[12]. In normal use for wind measurements, the FPI observes successively at several azimuths at an elevation chosen to take advantage of the van Rhijn effect and also at the zenith. A few minutes integration at each viewing angle is required to deduce the wind.

The MICADO instrument, developed by Thuillier [13] is a thermally-stable, field-widened Michelson interferometer which uses measurements of the modulation and phase shifts of a few fringes at large path difference to deduce both the temperature and wind. Though the interferometer is field-widened, the field-of-view of the telescope which captures the light for the interferometer is 1° which is sufficiently small for the detection proposed here. The estimated accuracy of the velocity of the wind determined from MICADO is 5 m/s.

A further development of the concept of the field-widened Michelson interferometer is the WAMDII instrument described by Wiens [14]. In this instrument, an image of the sky is formed on a CCD array through a field-widened Michelson interferometer. This arrangement allows the measurement of variation of wind and temperature over an extended field of view. The WAMDII instrument on board the UARS satellite ([15] utilizes this concept and ground-based versions of the instrument are also in use (W. Gault et al, private communication) though with only photomultiplier detectors. With careful calibration, winds can be measured with this instrument to a precision of 5 m/s or better.

The direct detection of gravity wave motion would require a modification of the usual operating mode of the interferometer, since the optimal direction for detecting such motion is with the field-of-view aligned with the major axis of the ellipse. An all-sky imager such as the one used by Taylor [16] can be used to detect the direction of the wavefronts and therefore used to choose the correct azimuth for observation.

The optimal elevation for observation depends on the wave period as illustrated in Figure 3. Imager data does not provide real-time information which could be used to determine the period and hence set the elevation. The WAMDII-type instruments offer a distinct advantage in that they can simultaneously observe over a range of elevations. MICADO and FPI instruments could only be set at elevations corresponding to wave periods appropriate to their integration times. The range of elevations indicated in Figure 3 for periods consistent with the required integration times means that the observing site would have to allow observation at elevations of the order of 10° or less.

Acknowledgement

We would like to thank Dr. J. Winick for helpful discussions. The investigation was associated with the ARC/AARC Airglow modelling program, the MAPSTAR program and the SOAR program. One of us (R. P. Lowe) acknowledges partial support from the Middle Atmosphere Project of the Canadian Network for Space Research (CNSR), a Federal Network-of-Excellence. The work was supported by the U.S. Office of Scientific Research (AFOSR) and the Phillips Laboratories under contract F 19628-91-K - 0024.

Appendix A

The ratio of the semi-minor to the semi-major axis may be obtained by first dividing Eq. (5) by l_0^2 so that everything is given in terms of the squares of the vertical to horizontal displacement ratios such as, $\left(\frac{h_0}{l_0}\right)^2$, or $\left(\frac{h_0}{l_0}\right)^4$. From the definition of $\bar{\eta}^2$ (Eq. (3)), we can then show:

$$\begin{aligned}\bar{\eta}^2 &= \frac{1}{4} \left(\frac{g}{c_s^2} - \frac{\omega_b^2}{g} \right)^2 = \left(1 - \frac{\gamma}{2} \right)^2 \frac{g^2}{c_s^4} = \left[\frac{\gamma^2 g^2}{4c_s^2} - \frac{(\gamma-1)g^2}{c_s^2} \right] \left(\frac{1}{c_s^2} \right) \\ &= \frac{\omega_a^2 - \omega_b^2}{c_s^2}\end{aligned}\tag{A1}$$

which leads to

$$\frac{\bar{\eta}^2}{k_x^2} = \left(\frac{c}{c_s} \right)^2 \frac{\omega_a^2 - \omega_b^2}{\omega^2}.\tag{A2}$$

With a slightly varied form of the Hines' dispersion relation (1960),

$$\frac{k_z^2}{k_x^2} = \frac{\omega_b^2 - \omega^2}{\omega^2} - \left(\frac{c}{c_s} \right)^2 \frac{\omega_a^2 - \omega^2}{\omega^2}\tag{A3}$$

and the definitions given in Eq. (3), we can then show that

$$\frac{|h_0|^2}{|l_0|^2} = \frac{|w|^2}{|u|^2} = \frac{k_x^2 \left[1 - \left(\frac{c}{c_s} \right)^2 \right]^2}{k_z^2 + \bar{\eta}^2}\tag{A4}$$

From (A1), (A2), and (A3) we obtain

$$\frac{k_z^2 + \bar{\eta}^2}{k_x^2} = \left(\frac{\omega_b^2}{\omega^2} - 1 \right) \left[1 - \left(\frac{c}{c_s} \right)^2 \right]\tag{A5}$$

Using (A4) and (A5) we finally obtain

$$\frac{|h_0|^2}{|l_0|^2} = \left(\frac{\omega}{\omega_b}\right)^2 \frac{\left[1 - \left(\frac{c}{c_s}\right)^2\right]}{\left[1 - \left(\frac{\omega}{\omega_b}\right)^2\right]} \quad (\text{A6})$$

Substituting (A2), (A4), (A5) and (A6) into Eq. (5) we obtain Eq. (9).

Eq. (11) for the angle of inclination of the semi-major axis to the zenith, $\bar{\alpha}$, can be obtained in more or less the same way. We begin with Eq. (7) and once again divide everything by l_0^2 so that everything is expressed in terms $\left(\frac{h_0}{l_0}\right)^2$ given by (A6). We then use A(2) and A(6) to obtain Eq. (11).

Both Eqs. (9) and (11) are expressed in terms of only two directly observable parameters such as the wave frequency and horizontal phase velocity. All the other formulae used are just simple approximations to these two.

REFERENCES

- 1.. G. D. Thome, Long-period waves generated in the polar ionosphere during the onset of magnetic storms, J. Geophys. Res., 73, 6319 (1968)
2. H. S. Porter and T. F. Tuan, On the behavior of the F-layer under the influence of gravity waves, J. Atmos. Terr. Phys., 36 135 (1974)
3. Y. T. Chiu and B.K. Ching, The response of atmospheric and lower atmospheric layer structure to gravity waves, J. Geophys. Res. Lett., 5, 539 (1978).
4. R. Hatfield, T. F. Tuan and S. M. Silverman, On the effects of Atmospheric Gravity Waves on Profiles of H, O₃, and OH Emissions, J. Geophys. Res. 86, 2429 (1981).
5. C. S. Gardner and J. D. Shelton, Density response of neutral atmospheric layers to gravity wave perturbations, J. Geophys. Res. 90, 1745 (1985)
6. J. R. Isler, T. F. Tuan, R. H. Picard and U. Makhoul, On the Nonlinear Response of Airglow to Linear Gravity Waves, J. Geophys. Res. 96, 14,141 (1991).

7. J. R. Isler, X. Li, T. F. Tuan, F. He and R. H. Picard, preprint submitted to J. G. R (1995)
8. C. O. Hines, Can. J. Phys., Internal gravity waves at ionospheric heights, 38, 1441 (1960).
9. E. H. Ryan, M. S. Thesis, University of Cincinnati (1991).
10. E. H. Ryan and T. F. Tuan, MAPSTAR CONFERENCE, Sept. (1991).
11. G. Hernandez, "*Fabry Perot Interferometers*", Cambridge University Press (New York) (1986).
12. D. Rees, A. Aruliah, T. J. Fuller-Rowell, V. B. Wickwar and R. J. Sica, Winds in the upper mesosphere at mid-latitudes: First result using an imaging Fabry-Perot interferometer, Geophys. Res. Letters 17, 1259 (1990).
13. G. Thuillier and M. Herse, Measurements of wind in the upper atmosphere: First results of the MICADO instrument, Progress in Atmospheric Physics R, Rodrigo et al. (eds.) pp, 61-73, Kluwer Academic Publishers (1988).
14. R. H. Wiens, G. G. Shepherd, W. A. Gault and P. R. Kosteniuk, Optical measurements of Winds in the lower Thermosphere, J. Geophys. Res. 93, 5973 (1988).

15. G. G. Shepherd, G. Thuillier, W. A. Gault, B. H. Solheim, C. Hersom, J. M. Alumni, J. F. Brun, S. Brune, P. Charlot, D. L. Desaulniers, W. F. J. Evans, R. L. Gattinger, F. Girod, D. Harvie, R. H. Hum, D. J. W. Kendall, E. J. Llewellyn, R. P. Lowe, J. Ohrt, F. Pasternak, O. Peillet, I. Powell, Y. Rochon, W. E. Ward, R. H. Wiens and J. Wimperis, J. Geophys. Res., preprint, (1996)
16. M. J. Taylor and M. J. Hill, Near infrared imaging of hydroxyl wave structure over an ocean site at low altitudes, Geophys. Res. Lett. 18, 1333 (1991).

Figure Captions

1. Geometry of elliptical trajectory for air parcel motion in the presence of a gravity wave. r_1 and r_2 are the semi-major and semi-minor axes respectively.
2. Actual elliptical trajectories at 93 km for gravity waves with a density perturbation of 5% and for a number of zenith angles, α , of the major axis. Notice the vast difference between the short period ($\tau \approx 6\text{min}$) trajectory with the zenith angle, $\alpha \approx 35^\circ$, and the long period ($\tau \approx 90\text{min}$) trajectory with $\alpha \approx 87^\circ$.

3. Plot of the trajectory polar (zenith) angle, α , as a function of period for different horizontal phase velocities.
4. Plot of the ratio of the semi-minor axis, r_2 to the semi-major axis, r_1 , as a function of period.
5. Schematic diagram showing the observation point, O, the two line of sights and the associated foot prints at 90 km altitude.
6. Diagram showing the relationship between the direction of the line-of-sight, the direction of the gravity wave and the wind direction. The polar and azimuthal angles for these directions are defined respectively as (θ, ϕ) , (θ_g, ϕ_g) and (θ_O, ϕ_O) . With horizontal background wind $\theta_O = 90^\circ$.
7. A plane view from above showing the projected line of sight, the projected wave propagation and the wind propagation.
8. The radial brightness-weighted velocity against time.

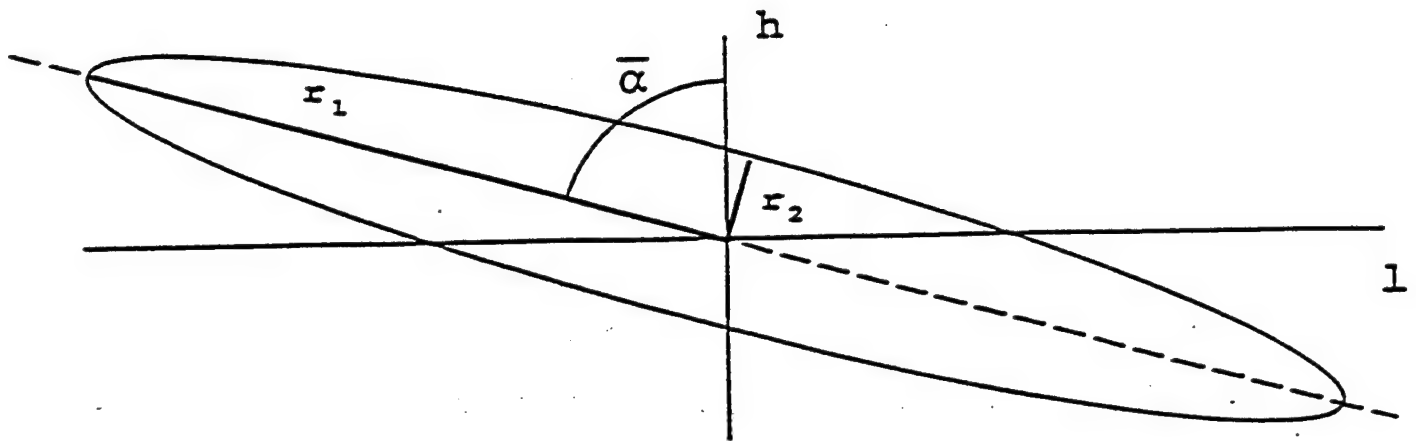


FIGURE 1

G.W. trajectories

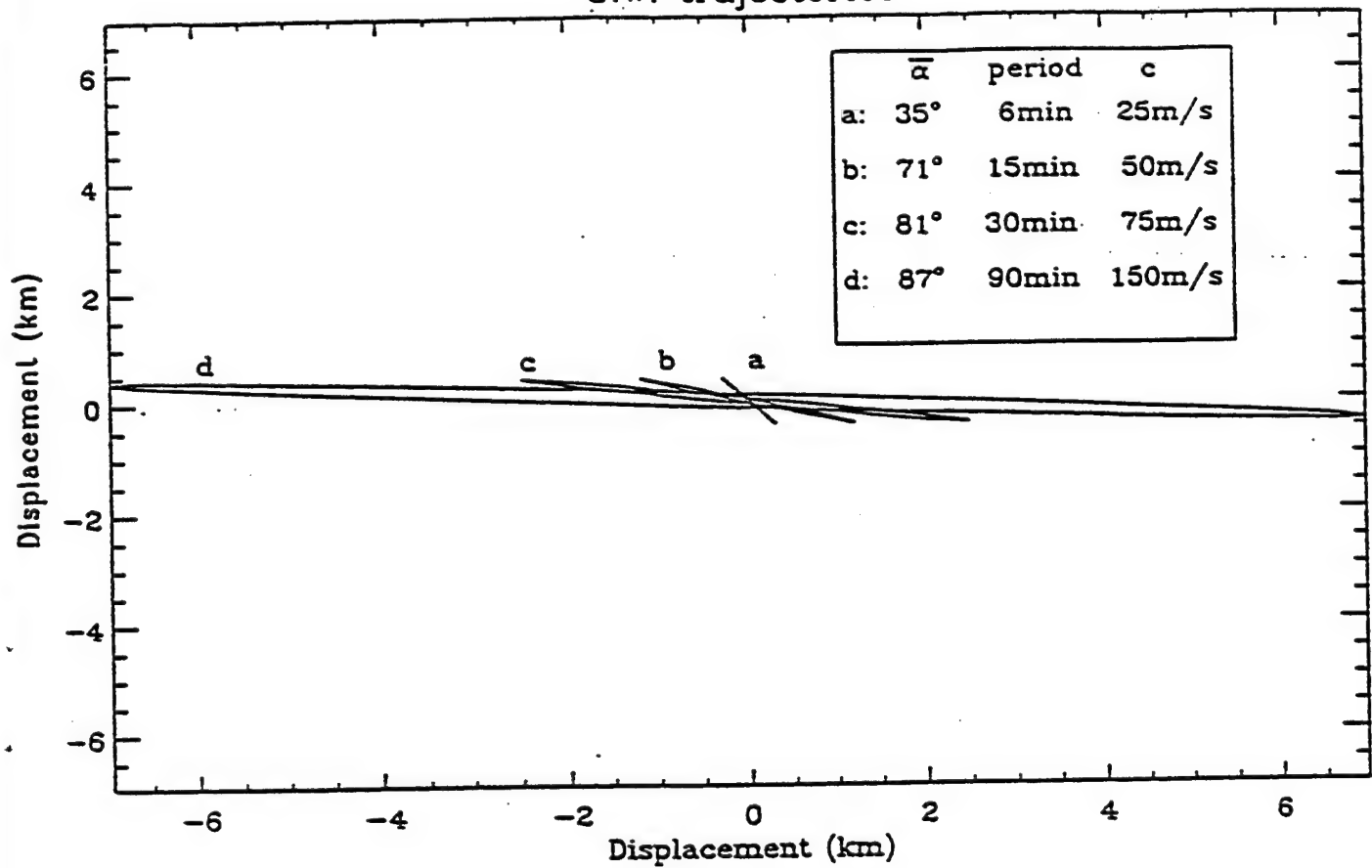


FIGURE 2

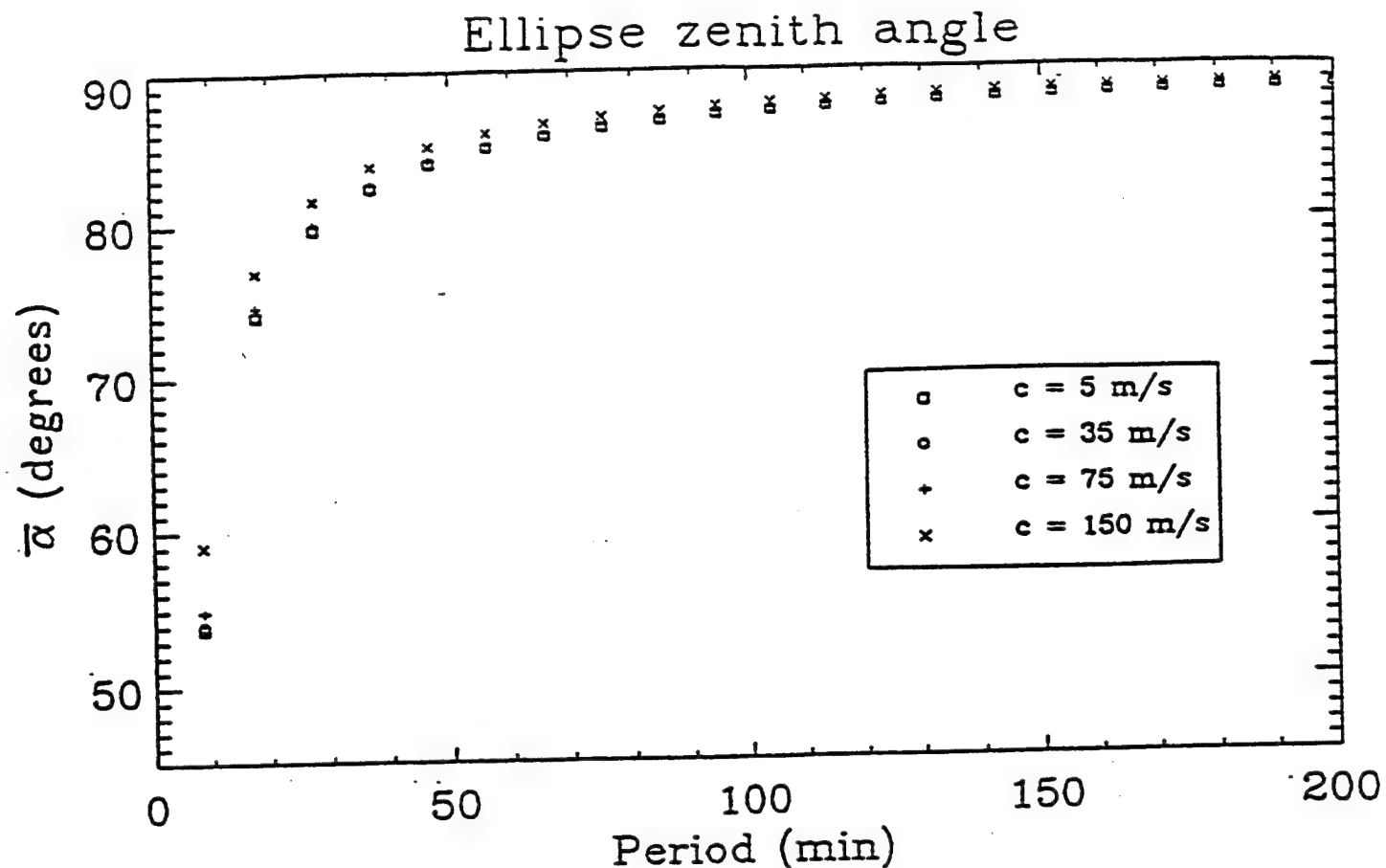


FIGURE 3

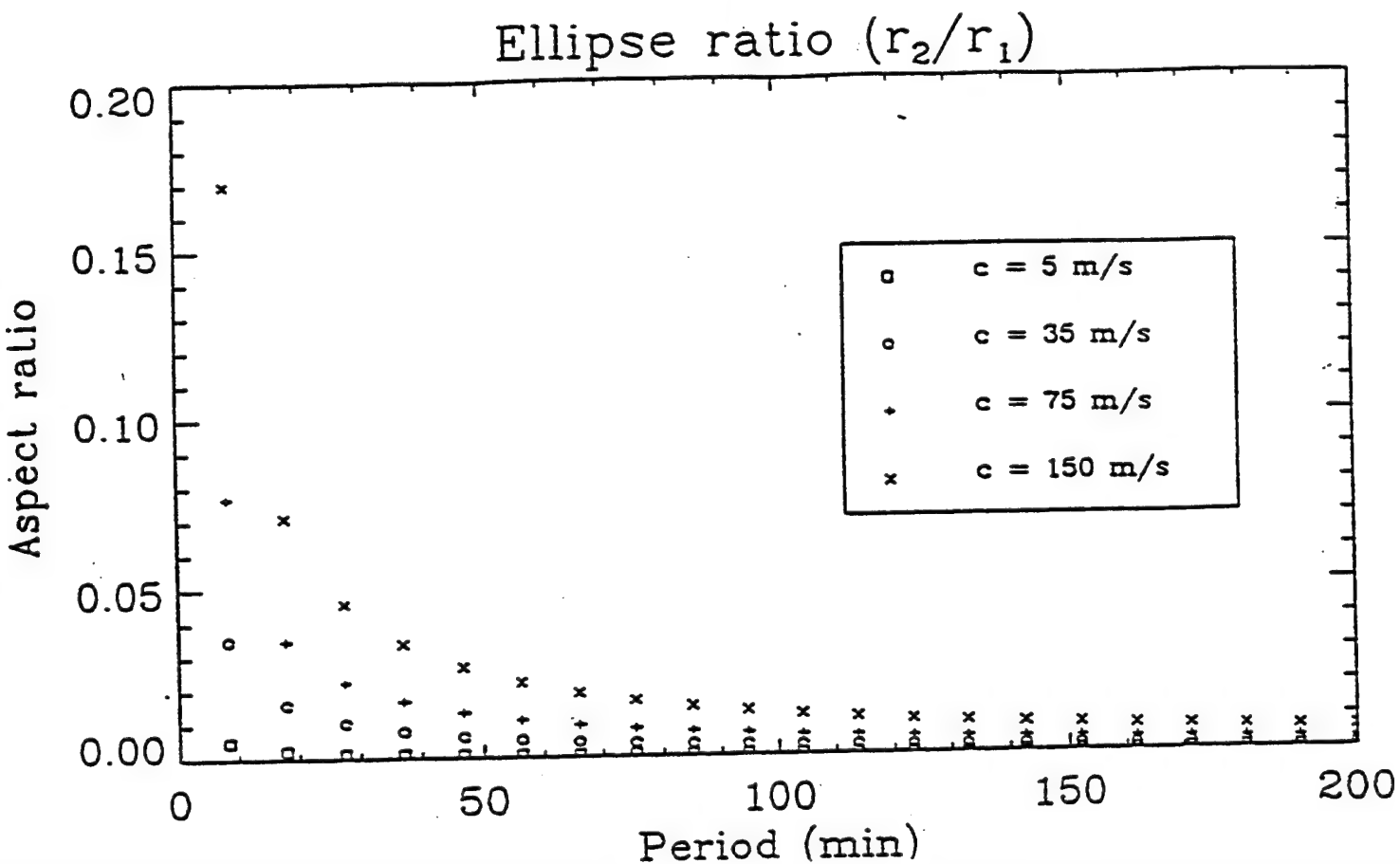


FIGURE 4

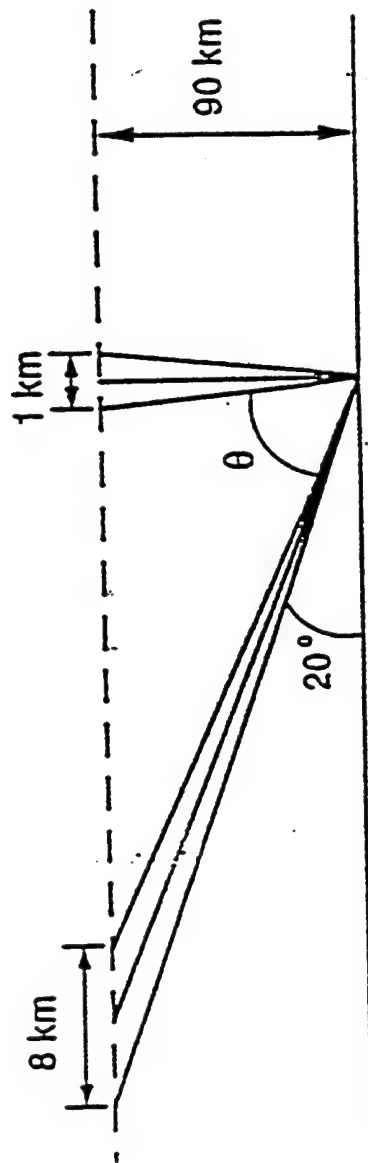


FIGURE 51

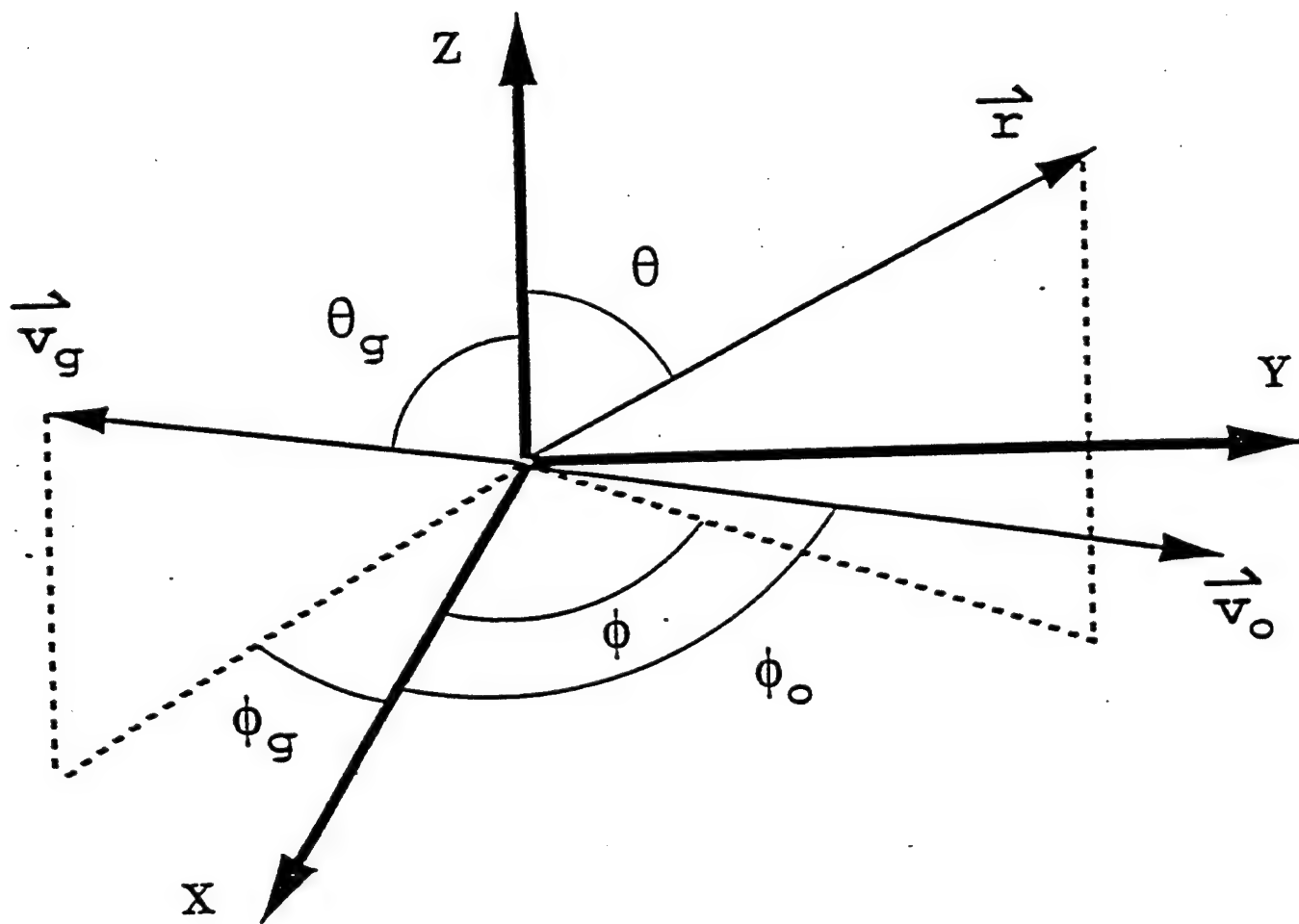


FIGURE 6

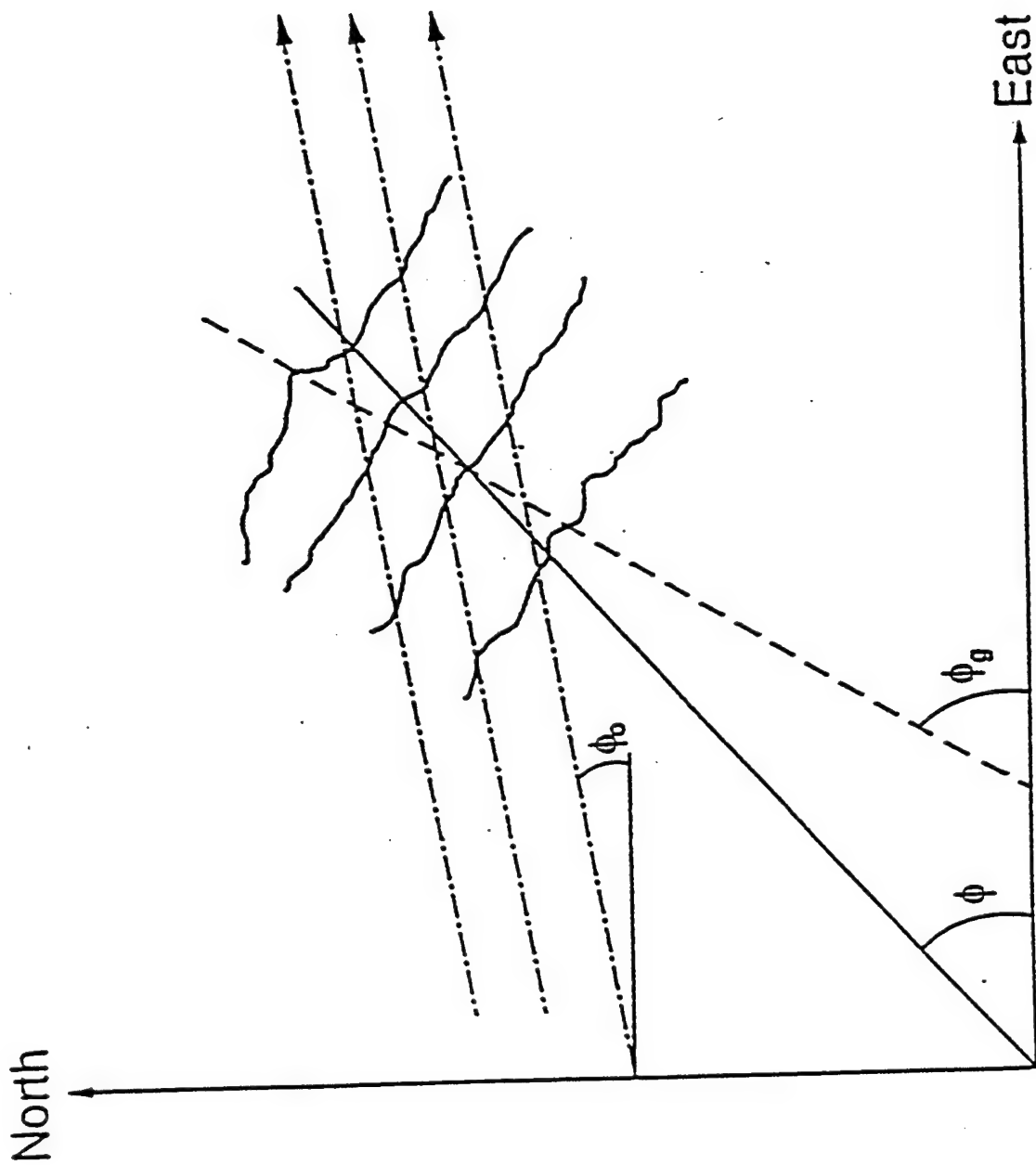


FIGURE 7

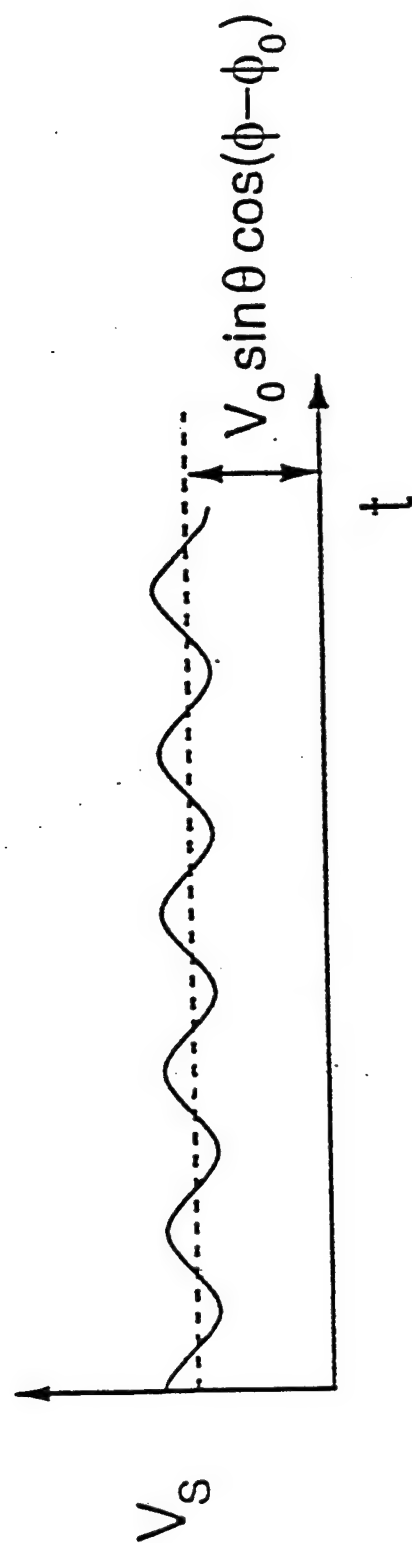


FIGURE 8

3. Evidence of Preferential Directions for Gravity Wave Propagation Due to Wind Filtering in the Middle Atmosphere

Introduction

In recent years, the importance of small-scale, short-period gravity waves on the dynamics of the upper atmospheric circulation has been recognized [Fritts and Vincent, 1987]. Observations of the bright infrared hydroxyl (OH) Meinel band emissions, which originate from a well-defined layer centered at an altitude of 87km [Baker and Stair, 1988], have proved most useful for investigating these waves.

Initially, the properties of the short-period waves were difficult to determine using spectrometric and single-point photographic measurements. Indeed it was not until Peterson and Kieffaber [1973] obtained photographic evidence of wavelike structure at near-infrared (NIR) wavelengths that their true extent was first appreciated. Since then there have been several photographic and low light TV investigations of wave structure in the NIR OH and other nightglow emissions at high, medium, and low latitudes (see, for example, Moreels and Herse [1977], Crawford et al. [1978], Peterson [1979], Hapgood and Taylor [1982], Herse [1984], Clairemidi et al. [1985], Armstrong [1986], Adams et al. [1988], Taylor et al. [1987, 1991a,b], Taylor and Henricksen [1989], and Taylor and Hill [1991]).

Low light images of the nightglow emissions provide an excellent method for remote sensing the two-dimensional spatial and temporal evolution of short-period wave motions over a large geographic area and with a high temporal resolution [Taylor et al., 1987]. The data gives important information on the occurrence frequency, horizontal wave lengths, and apparent horizontal phase velocities of the wave perturbation. These facts together with the geographical location, shape, orientation, and time of the displays have been most helpful in investigating potential wave sources [Taylor and Hapgood, 1988, Taylor and Edwards, 1991], many of which are thought to originate in the lower atmosphere.

Several attempts have been made in the past to associate various upper atmospheric wave phenomena with meteorological disturbances (see, for example, Hines [1968], Krassovsky and Shagaev [1977], Röttger [1977], Freund and Jacka [1979], Hung et al. [1979], Chiu and Sharp [1981], Gsvrilov and Shved [1982], Taylor and Hapgood [1988], and Taylor and Edwards [1991]). However, for various reasons, only a few of these investigations have succeeded in positively identifying individual wave sources.

To investigate the gravity wave morphology over an extended time interval, a series of measurements were recorded over 3 consecutive months during May, June, and July 1988. The observations were made as part of the Middle Atmospheric Periodic Structure and Associated Radiance (MAPSTAR) program and revealed similar spatial and temporal properties for the wave displays observed during each month, but a distinct tendency toward preferential directions of motion which varied from month to month was noted. The apparent asymmetry in the propagation headings of the gravity waves is due to the presence of critical layers which can occur at any height level where the horizontal wind velocity, along the direction of the horizontal wave vector, equals the horizontal phase velocity and the intrinsic frequency is Doppler-shifted to zero. At the critical layer height a horizontal surface region can be constructed to give a polar plot (a "blocking diagram") showing the range of azimuthal angles and speeds of gravity waves forbidden from further upward propagation [Ryan, 1991; Ryan and Tuan, 1991]. Gravity waves with horizontal phase speeds and directions within this region would encounter heavy absorption from a large number of diverse and relatively unstructured mechanisms [Booker and Bretherton, 1967; Hazel, 1967; Jones, 1968; Fritts and Geller, 1976; Fritts, 1978, 1979; He et al., 1990, 1991] as they approach the critical layer. Gravity waves with horizontal phase velocities outside this region would not encounter a critical layer and should be observable.

In the absence of detailed simultaneous wind measurements, we have first constructed a model of the zonal and meridional wind profiles for each month using the latest climatological information [Forbes, 1982a,b; Forbes and Gillette, 1982; Barnett and Corney, 1985; Fleming et al., 1988; Fleming and Chandra, 1989; Forbes and Vial, 1989; Chandra et al., 1990]. This model gives the mean wind profile for any geographic location and month of year from which we then construct the blocking diagrams which are computed for a given site, height, and time of the year (hour of the day and month). The results of the protracted OH image measurements are then compared with the model calculations to investigate the effects of wind filtering on the propagation of short period gravity waves into the upper atmosphere.

OH Observations

All-sky observations of the NIR nightglow emissions were made from the C1 site of the Mountain Research Station, near Nederland, Colorado (40.0°N, 105.6°W, 3050 m), using a modified Image Isocon TV system capable of obtaining good quality images of wave structure with an integration time of typically 2-5 s [Taylor et al., 1987]. The camera was fitted with a Nikon 8 mm, f/2.8 "fish eye" lens and a Schott RG715 filter. The combined response of this filter with the upper wavelength cutoff of

the camera tube (type S25) limited the band pass (at half maximum) of the observations to 715-810 nm. This region of the nightglow spectrum is dominated by several OH Meinel band emissions which have an integrated emission intensity of typically 2.0 kR [Llewellyn *et al.*, 1978]. Wave structure was detectable at all azimuths up to a range of ~ 600 km (limited by local horizon) which corresponds to a nominal search area of $\sim 10^6$ km² (assuming an emission altitude of 87 km). Observations were made during three consecutive new moon periods; May 11-22, June 7-22, and July 9-18, 1988. Coherent wave patterns were observed on 22 occasions during this time. Figure 1 shows a good example of a well-defined OH pattern with near east-west aligned wave fronts extending over the whole camera field. The image was obtained on July 10 at 0510 UT during a "bright night" display [Hoffmeister, 1952] when similar waveforms were also detected in the OI (557.7 nm) nightglow emission (which originates at ~ 96 -km altitude) [Offermann and Drescher, 1973] and at visible wave-lengths by the dark adapted eye. The clarity of the individual structures was best to the north and south of the individual site, but fainter, similarly oriented waveforms were also present in the zenith. The bright band intersecting the wave display at an acute angle is the Milky Way. Some discrete meteorological clouds (dark areas) can be seen at low elevations to the north and west. An increase in sky brightness due to scattered light from cities on the Colorado plains to the east is also evident. Data were obtained for approximately 4 hours this night, but after 0640 UT the recordings were limited by meteorological clouds. During this time the pattern remained extensive and uniform and moved toward the north. The high contrast and large apparent spatial extent of the display imaged on this occasion was quite unusual. Most of the wave patterns recorded during the campaign were less conspicuous and usually appeared as a set of well-formed elongated structures occupying a finite but variable area of the camera field (see Figure 2).

The data have been analyzed to determine the geographic location and orientation of the wave patterns and where possible their horizontal phase speeds. The all-sky images were calibrated in terms of elevation and azimuth using the right ascension and declination of several known stars within the camera field [Hapgood and Taylor, 1982; Lanchester, 1985]. Ground maps showing the position and motion of the waveforms as a function of time were then calculated for each display (assuming an emission altitude of 87 km), from which their average horizontal wavelengths and velocities were determined. Figure 2 shows six example maps (two for each month) illustrating the diversity in location, apparent spatial extent, orientation, and motion of the displays. The maps are centered on the mountain research station and show Colorado and adjoining states. Typically several waveforms are detected within the camera field at any one time, but sometimes many more coherent forms

were present. The general direction of motion of each display is indicated by the arrows. Only those waveforms that subtended elevations significantly greater than 5° are plotted.

The results of the image analysis are listed in Table 1. The azimuth of the wave motions (i.e., the normal to the wave fronts) was determined from the ground maps to an accuracy of about $\pm 5^\circ$. This represents the dominant direction of motion of each pattern measured over a time interval of typically 0.5 to 4 hours during the nights (depending upon observing conditions). However, at any given time, individual waveforms often exhibited considerable spread about this direction (see Figure 2). Due to changes in the seeing conditions (particularly in June) it was usually easier to determine the orientation and direction of motion of the wave pattern than it was to accurately measure its speed. Nevertheless, velocity measurements were obtained on 14 of the 22 displays detected during the campaign. Several measurements were made from the ground maps to determine the average speed for each display. The spread in individual measurements was used to provide an estimate of the error in each case (see Table 1). On two occasions (June 20-21 and July 12) a second wave motion was also detected during a course of the night and both sets of measurements are reported here. Each month shows a clear preference for wave propagation generally toward the north (in total 68% of the wave azimuths were within $\pm 40.0^\circ\text{N}$). In May and June, several displays also exhibited significant eastward motion. In July the northward motion became even more restricted in the azimuth range 83% within $\pm 30.0^\circ\text{N}$) with only one exception of a wave pattern moving toward the southeast. In particular none of the displays observed during this campaign exhibited strong westward components of motion.

The Wind Profiles Used

In the absence of suitable wind measurements we have constructed a model [Ryan, 1991; Ryan and Tuan, 1991] for deriving wind profiles at any site (latitude and longitude) and time (hour of the day and month of the year) using the latest available information on the background winds and the solar diurnal and semidiurnal tides and the lunar semidiurnal tide.

Background Winds and Tidal Oscillations

To calculate the magnitude and direction of the total wind at any given height, the background wind and three predominant atmospheric tides (solar diurnal (SD), solar semidiurnal (SSD), and lunar semidiurnal (LSD)) were added together in the zonal and meridional directions. Climatological data were used for the background winds and numerical model data for the tidal modes.

$$\text{Total wind} = \text{background} + \text{tidal wind} \quad (1)$$

The zonal background wind was obtained from the monthly mean zonal wind tables of *Fleming et al.* [1988] which are discussed by *Fleming and Chandra* [1989] and *Chandra et al.* [1990]. The meridional background winds were calculated from the monthly amplitudes and phases of "wave 1" and "wave 2" of the mean geopotential height given by *Barnett and Corney* [1985]. This wind component is often termed the meridional geostrophic wind [*Fleming et al.*, 1988]. The sum tidal modes were calculated from tabular values for their amplitudes and phases using the equation

$$\text{tidal wind} = \sum_i A_i \cos \left[\left(\frac{2\pi}{T_i} \right) (t - \phi_i) \right] \quad (2)$$

where i is summed over each of the SSD, LSD, and SD components and A_i is the amplitude, ϕ_i is the phase, T_i is the period of the tide (i.e., 24 hours for SD and 12 hours for SSD and LSD), and t is the local time. The SSD amplitudes and phases were obtained for each month using the Forbes/Vial Model Tides 1988. This information is available from the *NCAR CEDAR Data Base* [1990] and is discussed by *Forbes and Vial* [1989]. The data consists of monthly averages and is given from latitude 88° south to 88° north at 2° intervals from the ground level to 110 km. Amplitudes and phases for the SD and LSD components are not available on a monthly basis and values for solstice and equinox conditions were used [*Forbes*, 1982 a,b; *Forbes and Gillette*, 1982]. These tables provide amplitudes and phases from 0° to 78° latitude at 6° intervals from the ground level to 400 km.

Analysis of the Climatological and Numerical Data Model

The zonal and meridional wind profiles for a given height and geographical site were determined by the linear interpolation between the available tabulated values for (1) immediate above and below the height of interest and (2) locations in the immediate surroundings of the site of interest. The tables of wind profiles use different height intervals depending the amplitudes and phases were interpolated separately and the profiles computed from the resultant data points. In the second method the profiles were computed directly using the tabulated data and then interpolated to produce the wind components. As expected, both approaches gave very similar results. Profiles may be computed for any hour of the day and for each month of the year [*Ryan*, 1991; *Ryan and Tuan*, 1991].

As the SD and LSD tidal components are only available for equinox and solstice conditions, wind profiles for months such as March and April currently utilize the equinox data, while May and June employ the summer solstice data. It should be noted that the first available data point for the meridional background wind occurs in the stratosphere at 17 km. For the meridional background occurs in the stratosphere at 17 km. For the meridional component the highest available data point occurs at 85 km. Since the meridional wind is much less important than the zonal wind and at this height level the tidal components dominate, a linear extrapolation was employed to extend the meridional wind to 100 km.

Wind Profiles for Colorado Campaign 1988

Wind profiles were computed for the optical site at the Mountain Research Station for May, June, and July at local midnight. Figure 3 shows the total zonal and meridional components for each of these months (dashed curves). For comparison, wind profiles for December are also plotted (solid curve) to illustrate the difference between summer and winter solstice conditions. The zonal profile shows a steady westward wind during the summer months at a stratospheric and mesospheric levels with a peak amplitude at ~65 km increasing from ~30 m s⁻¹ in May to greater than 60 m s⁻¹ over an extended region in the middle atmosphere.

The meridional wind is strongly influenced by the tidal components and grows significantly weaker than the zonal wind throughout the middle atmosphere (note the change in horizontal scale for the wind amplitude) and the summer and winter are generally 180° out of phase with each other due to changes in the tidal oscillations. The contribution of the tidal motions (Figure 4) are not important in the lower atmosphere (below 40 km) and they only begin to play a significant role (particularly affecting the meridional winds) at mesospheric heights.

The Model for Critical Level Blocking Diagrams

The Doppler-Shifted Frequency

The theory of gravity wave absorption at critical layers is well developed (see, for example, *Booker and Bretherton* [1967], *Hines and Reddy* [1967], *Hazel* [1967], *Jones* [1968], *Fritts and Geller* [1976], *Fritts* [1978,1979], and *He et al.* [1990,1991]). Gravity waves propagating energy upward from the lower atmosphere are absorbed into the mean flow (and by other mechanisms) as they approach a "critical layer" where the intrinsic frequency of the wave is Doppler-shifted to zero. This situation

may occur at any height level when the local horizontal wind speed along the direction of propagation equals the observed horizontal phase speed of the gravity wave (which remains constant with altitude). The Doppler-shifted frequency, Ω , due to the horizontal wind V_0 is given by

$$\Omega = \omega - k_x V_{0x} \quad (3)$$

where ω is the source frequency, k_x is the magnitude of the horizontal wave vector, and V_{0x} is the component of V_0 along v_x . Eq. (3) can be rewritten as

$$\Omega = \omega \left[1 - \frac{V_{0x}}{v_x} \right] \quad (4)$$

where v_x is the observed horizontal phase speed of the wave. Thus at the critical layer when $V_{0x} = v_x$, $\Omega = 0$. Equation (4) can be expressed in terms of the zonal and meridional components as [Wang and Tuan, 1988]

$$\Omega = \omega \left[1 - \frac{V_z \cos \phi + V_m \sin \phi}{v_x} \right] \quad (5)$$

where V_z and V_m are the zonal and the meridional wind components.

Eq. (5) was used to determine the forbidden regions defined by $\Omega \leq 0$ at any height below the peak of the OH layer for each propagation direction ϕ and phase speed v_x . Although downward reflections from any critical layer can be significant [He *et al.*, 1990, 1991], they do not affect the OH layer if the sources are located in the lower atmosphere. Polar plots (blocking diagrams) with v_x as the radius and ϕ as the polar angle were then constructed to show which directions and magnitudes are restricted for gravity wave propagation up to OH altitudes.

Blocking diagrams [Ryan, 1991; Ryan and Tuan, 1991] were plotted for each month using the wind profiles derived for the Colorado optical site. As expected, each plot (see Section 5) shows a forbidden region for westward wave propagation due to the strong zonal winds in the stratosphere and lower mesosphere. The blocking effect increases considerably in "area" from May to July, eventually restricting all

westward propagating gravity waves with observed phase speeds below $\sim 65 \text{ m s}^{-1}$. Some blocking also occurs to the east during these 3 months. This is mainly due to zonal winds below 20 km and is much less than the westward blocking. Wave propagation toward the north and south is generally much less restricted. Due to the tidal modes the blocking diagrams can vary at different hours of the day (see Figure 9).

Results

Figures 5, 6, and 7 show the blocking diagrams for May, June and July at local midnight for the observation site. The figures were computed for a height of 85 km. This is just below the nominal peak of OH emission ($\sim 87 \text{ km}$, half width 5-8 km) and each plot, therefore, represents the cumulative effects of wave blocking for all heights up to and including the base of the OH layer. For clarity, the restricted regions for wave propagation are indicated by the shaded areas. Superimposed on each of these diagrams are the average horizontal propagation directions and magnitudes (where known) of the 22 wave displays recorded during this period. The solid arrows indicate magnitude and direction of the wave motions, while the dashed arrows show direction only.

In May, six wave displays were recorded and four velocity measurements made (see Table 1). Figure 5 shows that all six wave patterns moved in directions that were least impeded for gravity wave propagation. Moreover, the four measurements of the phase velocity were all in excess of the blocking limits indicating unrestricted wave propagation to OH altitudes. During June (Figure 6), ten wave patterns were detected, but due to limitations in the observing conditions, only five velocity measurements were possible. Nevertheless, the azimuthal distribution of the patterns were again favorable for the wave propagation from the lower atmosphere. One of the displays observed on June 22 (azimuth 80°) exhibited a velocity that was apparently insufficient for wave propagation up to 85 km. However, the wave azimuth was clearly directed away from the major blocking region (i.e., almost due east) and the observed phase speed could well have been in excess of the actual blocking limit that existed on this night.

During July (Figure 7), the sky conditions improved considerably and velocity measurements were possible on five of six displays. Remarkably, all but one of the wave patterns recorded during this month exhibited well-defined motion towards the north. Moreover, the observed phase speeds of the patterns (including the display moving towards the south east) significantly exceeded the nominal blocking limits on each occasion.

Discussion

The spatial and temporal properties of the wave motions reported here are typical of the mid-latitude nightglow displays described in literature (see, for example, *Peterson and Kieffaber* [1973], *Moreels and Herse* [1977], *Armstrong* [1986], *Taylor et al.* [1987]). On occasions these displays have been associated with the passage of short-period (<1 hour) gravity waves through the nightglow layers. Although individual sources for the waves have been difficult to locate, there are good reasons why many of the wave sources may be located in the lower atmosphere [*Hines*, 1960]. In this study all of the wave sources were assumed to be located in the tropospheric regions.

A comparison of the image measurements with the climatological model predictions show almost complete agreement between the predicted (i.e., least restricted) and the observed directions of wave propagation. Furthermore, with only one exception the apparent phase speeds of the waves were always greater than the predicted blocking limits. Thus, the waves responsible for the OH patterns observed during this campaign were probably subjected to considerable directional filtering. The agreement suggests that middle atmospheric winds can play an important role in governing the flux and azimuthal distribution of short-period wave energy reaching the upper atmosphere. As the filtering theory assumes a tropospheric origin for the waves, this study is also consistent with the generally accepted idea of a predominance of lower atmosphere sources at mid-latitudes.

The anisotropy observed in the distribution of wave azimuths is a key element of this study. Assuming the effects of wind filtering were negligible, this result could conceivably have been caused by a nonuniform distribution of sources. This requires that the wave sources were located (1) primarily to the south and west of the optical site during May and June and (2) almost exclusively to the south of the site in July. Moreover, there should have been no similar type sources to the east of the optical site for the duration of the campaign. While the distribution of wave sources during this period was almost certainly not uniform, it is highly improbable that it would have given rise to the observed set of wave motions. As the winds in the middle atmosphere (see Figure 3) can be large compared with the apparent phase speeds of the waves (see Table 1), it is much more likely that the anisotropy in the data resulted from directional filtering of an ensemble of wave motions.

To simplify the investigation the blocking diagrams shown in Section 5 were computed assuming that all of the wave sources were located in the vicinity of the optical site. In practice, we do not know the actual position

of the sources with respect to the observer. In the absence of background winds, gravity waves of a period of ≤ 1 hour would be expected to propagate from the source region to OH heights within a ground range of ~ 800 km [Freund and Jacka, 1979; Taylor and Hapgood, 1988]. However, as the path of the gravity wave through the atmosphere is strongly dependent upon its intrinsic frequency [Hines, 1960], which changes with the prevailing wind conditions (equation (3)), the horizontal range over which the waves may propagate can be significantly larger. Thus, many of the wave motions imaged by the all-sky camera may have originated from sources located several hundred kilometers from the observing site.

To investigate the effects of varying the source location on the blocking diagrams, wind profiles at points $\pm 4^\circ$ in latitude and longitude to the north, south, west, and east of the optical site were calculated (corresponding to a change in source position of 890 km in latitude and 680 km in longitude). Figure 8 shows the total zonal and meridional wind components for June. The zonal wind depends solely upon the latitude, and plots are given only for points north and south of the center (optical) site. Some differences between the south and the center/north profiles arise above 60 km altitude but they are no greater than the changes that take place from June and July (see Figure 3), both of which exhibit similar blocking diagrams (Figures 6 and 7). The meridional winds are more sensitive to variations in source location (e.g., the profile to the south of center), but as the zonal winds dominate, the overall effects on the blocking diagrams are not significant. Thus, uncertainties in the location of the wave sources of up to several hundred kilometers appear to have little impact on the net wave filtering. However, sources located at significantly larger ranges may well encounter different wind profiles than those existing at the observing site.

As the wave displays were imaged at different times during the night, changes in the tidal contributions to the wind profiles have also been investigated. This is important as the temporal origin of each wave is not known. For short-period waves the group velocities should be less than the observed phase velocities (i.e., < 50 m/s, see Table 1), and propagation times of a few to several hours would be expected [Taylor and Hapgood, 1988]. To examine the effect of time changes on the blocking areas, the total zonal and meridional wind components were plotted at 1-hour intervals over the period of 0400 to 0900 UT when most of the data were recorded (2200 to 0300 LT). As expected, the zonal winds showed minimal changes, but the meridional winds varied substantially. Figure 9 illustrates the changes in wave blocking that can occur. The diagrams are plotted for June at 2200 and 0200 LT. The net effect of the tidal variations appears to be a clockwise expansion of the major (western) blocking sector. A similar trend was also found for May and July. During the winter

months a counterclockwise rotation of the blocking area from 1000 to 0200 LT occurs. In general, the short-term effects of the tidal mode changes on the blocking diagrams were greater than those induced by variations in the source location. Changes in the blocking area during the course of the night (see Figure 9) may therefore affect the propagation of some waves (particularly those moving northward), but there are no obvious signs of this in our (limited) data set.

The filtering of a gravity wave by its absorption into the mean flow at a critical layer applies only when the background winds through which the wave is propagating are stable (i.e., when the Richardson's number, Ri , of the background is significantly greater than $1/4$). Wind profiles exhibiting very steep vertical gradients ($Ri < 1/4$) are naturally unstable and reradiation or overreflection of the gravity wave can occur [Jones, 1968; Fritts, 1978; He *et al.*, 1991]. Under these circumstances the effect of the wind filtering on the gravity waves needs to be reassessed. An examination of a large number of climatological data on background winds and atmospheric tides has yielded little evidence for such steep vertical gradients. Nevertheless, it is quite possible that a chance combination of background winds with other long-period gravity waves may induce localized regions of instability into the real wind profile. However, the overall agreement between the critical layer theory and the nightglow observations presented here suggest that the occurrence of unstable background winds may be relatively rare.

Figure 10 illustrates the effect of changing the altitude of the blocking investigation. Two heights, 80 and 100 km, are plotted showing the changes in the blocked areas for the optical site at local midnight during May. As discussed earlier, below 90 km, most of the blocking occurs for westward propagating waves. However, above 90 km, strong blocking occurs for both eastward and westward propagating waves. Similar results were obtained during June and July. For comparisons the blocking diagrams for winter solstice conditions (December) were also plotted. These plots (not shown) indicate major blocking for eastward wave motion for altitudes up to 100 km. Unlike the summer plots, the winter blocking diagrams remain virtually unchanged over the height range 80 to 100 km. On several occasions, during July, similar wave patterns were imaged in the OH and OI (557.7 nm) green line emissions (peak altitude ~96 km). Depending upon the azimuth of the wave motions, it is possible that gravity waves seen in the OH emission may not reach the OI layer. Indeed, attempts to image green line structure during May and June when several of the OH wave patterns imaged in July exhibited strong northward motion (see Figure 7) which is the direction of least blocking at both the OH and the OI altitudes. Thus, although limited, the OI data provide further support of wave filtering by winds.

The sources of the waves observed during this period are under investigation but are currently unknown. An unexpected consequence of this analysis points toward a tropospheric origin for the bulk of the wave motions. During the campaign, many thunderstorms were reported over Colorado and the neighboring states. Thunderstorm activity has been identified as a source of short-period gravity waves on at least one prior occasion [*Taylor and Hapgood*, 1988]. By comparing the properties of the image data with the distribution of thunderstorms and other tropospheric disturbances it may be possible to identify individual wave sources using the wind-filtering model.

The results of this study are quite remarkable when it is recalled that the blocking diagrams were developed using climatological data which provide only an estimate of the wave filtering to be expected to be expected at any given site for this time of the year. Ideally, for this type of investigation, simultaneous wind profile measurements should be made in the vicinity of the nightglow observations. The fact that the wave data collected over the 3-month period exhibited magnitudes and directions consistent with the model results suggests that climatological data are probably sufficient for this type of study. However, more measurements are needed before any firm conclusions can be drawn on this point. In particular, data taken during the winter months from a similar mid-latitude site when the zonal winds blow toward the east (i.e., in the opposite direction to the summer flow) should provide a further important test for the theory.

Summary

The critical layer theory for gravity wave filtering has been applied to an extended set of nightglow measurements to study the effects of middle atmospheric winds on the propagation of short-period gravity waves. All-sky images of the NIR OH emissions are well suited for this research as they provide precise information on the directions of motion and the apparent speeds of the waves reaching the upper atmosphere. The measurements reported here show almost total agreement between the observed and the permitted wave azimuths and speeds. This result indicates that the flow of wave energy into the upper atmosphere can be significantly modified by the background winds. Whether wind filtering dominates the flux of short-period wave energy at other sites (at high, medium, and low latitudes) and times of the year has yet to be determined. If further nightglow measurements substantiate these findings, the wind-filtering model may be used to help make a more quantitative investigation of the dominant wave sources and to study regional and seasonal effects of short-period gravity waves on the

dynamics of the upper atmosphere.

While one may well argue that only instantaneous wind profiles measured at the same time as the airglow data should be used, the combined data collected over 3 months, the general consistency between the forbidden region of the blocking diagrams and the observed gravity wave propagation directions as well as magnitudes, would all suggest that in the late spring and early summer months there may well be gravity wave (GW) directional filtering. Further verifications were found when the OH data taken by Lowe et al. on April 18, 1991, in London, Ontario, were checked with the blocking diagrams for London. The time of the year for this particular data set is of special interest. Obviously, more observations are needed before any firm conclusions can be drawn. Data taken during the winter when the zonal winds are blowing eastward (in the opposite direction) should give this theory a further important test.

We should mention that the filtering of a gravity wave through its absorption into the mean flow at the critical layer region applies only to stable background winds (i.e., the Richardson's number of the background winds is much greater than $1/4$). For wind profiles with much steeper vertical gradients so that the background becomes unstable, reradiation and overreflection [Jones, 1968; Fritts, 1978; He et al., 1991] can occur. Under such circumstances the gravity wave blocking has to be entirely reexamined. However, in examining a large number of climatological background winds and atmospheric tides, we are unable to find much evidence for such steep vertical background wind gradients. It is always possible, of course, for instantaneous wind profiles, modified by long-period "background" gravity waves, to exhibit such background instability. But the overall consistency between the observed GW propagation and the blocking diagrams would suggest that the occurrence of such unstable background winds would be relatively rare.

Acknowledgments. We are most grateful to the director and staff of the Mountain Research Station of the University of Colorado for allowing us the use of their facilities for the optical measurements. We thank M.J. Hill (Southampton University) and P. Mace (Utah State University) for their considerable help during the campaign. We would like to thank E.A. Dewan, R.H. Picard, R.P. Lowe, and J.R. Winick for many helpful discussions on the gravity wave "blocking" model as well as the wind model. We would also like to thank R. Barnes of NCAR for his help with the Forbes/Vial Model Tides and to E. Fleming of Applied Research Corporation for supplying the climatological data as well as NCAR for the use of their CEDAR data base. This research was supported by the U.S. Air Force Office of Scientific Research (AFOSR) and the Phillips Laboratory under contract

F19628-87K-0023 and F19628-91-K-0024. The work was also supported by the ARC/AARC Airglow Modeling and the MAPSTAR program.

The Editor thanks C.G. Fesen and J.A. Waldock for their assistance in evaluating this paper.

REFERENCES

- (1) Adams, G. W., A. W. Peterson, J. W. Brosnahan, and J. W. Neuschaefer, Radar and optical observations of mesospheric wave activity during the lunar eclipse of 6 July 1982, *J. Atmos. Terr. Phys.*, 50,11, 1988.
- (2) Armstrong, E. B., Irregularities in the 80- to 100-km region: A photographic approach, *Radio Sci.*, 21, 313, 1986.
- (3) Baker, D. J., and A. T. Stair, Jr., Rocket measurements of the altitude distributions of the hydroxyl airglow, *Phys. Scr.*, 37, 611, 1988.
- (4) Barnett, J. J., and M. Corney, Planetary waves, Middle Atmosphere Program, *Map Handb.*, 16, 86, Sci. Comm. Sol. Terr. Phys. Sec., Univ of Ill., Urbana, 1985.
- (5) Booker, J. R., and F. P. Bretherton, The critical layer for internal gravity waves in shear flow., *J. Fluid Mech.*, 27, 3, 513, 1967.
- (6) Chandra, S., E. Fleming, M. Schoeberl, and J. Barnett, Monthly mean global climatology of temperature, wind, geopotential height and pressure for 0-120 km, *Adv. Space Res.*, 6, (6)3, 1990.
- (7) Chiu, Y.T., and L.R. Sharp, Correlative study of thermospheric gravity waves and tropospheric vorticity area index, *Geophys. Res. Lett.*, 8, 281, 1981.
- (8) Clairemidi, J., M. Herse, and G. Moreels, Bi-dimensional observations of waves near the mesopause at auroral latitudes, *Planet, Space Sci.*, 33, 1013, 1985.
- (9) Crawford, J., P. Rothwell, and M. J. Taylor, ASSESS 2: A simulated mission of Spacelab, Review Article, *Nature*, 275, 17, 1978.
- (10) Fleming, E., S. Chandra, M. Shoeberl, and J. Barnett, Monthly mean global climatology of temperature, wind, geopotential height and pressure for 0-120 km, *NASA Tech. Memo.* 100697, 1988.
- (11) Forbes, J. M., Atmospheric tides, 1, Model description and results for the solar diurnal component, *J. Geophys. Res.*, 87(A7), 5222, 1982a.
- (12) Forbes, J. M., Atmospheric tides, 2, The solar and lunar semidiurnal components, *J. Geophys. Res.*, 87(A7), 5241, 1982b.
- (13) Forbes, J. M., and D. F. Gillette, A compendium of theoretical

atmospheric tidal structures, 1, Model description and explicit structures due to realistic thermal and gravitational excitation, *Rep. AFGL-TR-82-0173(1)*, Air Force Geophys. Lab, Hanscom Air Force Base, Mass., 1982, ADA 125720

(14) Forbes, J. M., and F. Vial, Monthly simulations of the solar semidiurnal tide in the mesosphere and lower thermosphere, *J. Atmos. Terr. Phys.*, 51(7/8), 649, 1989.

(15) Francis, S. H., Global propagation of atmospheric gravity waves: A review, *J. Atmos. Terr. Phys.*, 37, 1011, 1975.

Freund, J. T., and F. Jacka, Structure in the 557.7 nm (OI) airglow, *J. Atmos. Terr. Phys.*, 41, 25, 1979.

(16) Fritts, D. C., The nonlinear gravity wave-critical level interaction, *J. Atmos. Sci.*, 35, 397, 1978.

(17) Fritts, D. C., The excitation of radiating waves and Kelvin-Helmholtz instabilities by gravity wave-critical level interaction, *J. Atmos. Sci.*, 36, 12, 1979.

(18) Fritts, D. C., and M. A. Geller, Viscous stabilization of gravity wave critical level flows, *J. Atmos. Sci.*, 33, 2276, 1976.

(19) Fritts, D. C., and R. A. Vincent, Mesospheric momentum flux studies at Adelaide, Australia: Observations and a gravity wave-tidal interaction model. *J. Atmos. Sci.*, 44, 605, 1987.

(20) Gavrilov, N. M., and G. M. Schved, Study of internal gravity waves in the lower thermosphere from observations of the nocturnal sky airglow [OI] 5577 Å in Ashkhadab, *Ann. Geophys.*, 38, 789, 1982.

(21) Hapgood, M. A., and M. T. Taylor, Analysis of airglow image data, *Ann. Geophys.*, 38, 805, 1982.

Hazel, P., The effect of viscosity and heat conduction on internal gravity waves at a critical level, *J. Fluid Mech.*, 30(4), 775, 1967.

(22) He, F., T. F. Tuan, R. Picard, and J. Isler, Optical model analysis of gravity-wave reflections from critical layers, *Eos Trans. AGU*, 71, 1496, 1990.

(23) He, F., T. F. Tuan, R. Picard, and J. Isler, Modeling of optical model treatment of gravity-wave reflections from critical layers, *Eos Trans. AGU*, 72,(17), Spring Meeting Suppl., 208, 1991.

- (24) Herse, M., Waves in the OH emissive layer, *Science*, 225, 172, 1984.
- (25) Hines, C. O., Internal atmospheric gravity waves, *Can. J. Phys.*, 38, 1441, 1960.
- (26) Hines C. O., A possible source of waves in noctilucent clouds, *J. Atmos. Sci.*, 25, 937, 1968.
- (27) Hines C. O., and C. A. Reddy, On the propagation of atmospheric gravity waves through regions of wind shear, *J. Geophys. Res.*, 72, 1015, 1967.
- (28) Hoffmeister, C., Investigations on bright night sky and luminous bands, *J. Brit. Astron. Assoc.*, 62, 288, 1952.
- (29) Hung, R. J., T. Phan, and R. E. Smith, Coupling of ionosphere and troposphere during the occurrence of isolated tornadoes on November 20, 1973, *J. Geophys. Res.*, 84,1261, 1979.
- (30) Jones, W.L., Reflexion and stability of waves in stably stratified fluids with shear flow: A numerical study, *J. Fluid Mech.*, 34(3), 609, 1968.
- (31) Krassovsky, V. I., and M. V. Shaghaev, On the nature of internal gravity waves observed from hydroxyl emissions, *Planet Space Sci.*, 25, 200, 1977.
- (32) Lanchester, B. S., Relation between discrete auroral forms and magnetic field disturbances, PhD. Thesis, Univ of Southampton, England, 1985.
- (33) Llewellyn, E. J., B. H. Long, and B. H. Solheim, The quenching of OH* in the atmosphere, *Planet. Space Sci.*, 26, 525, 1978.
- (34) Moreels, G., and M. Herse, Photographical evidence of waves around the 85 km level, *Planet. Space Sci.*, 25,265, 1977.
- (35) National Center for Atmospheric Research (NCAR) CEDAR Data Base Catalog, *Forbes/Vial Model Tides 1988*, Boulder, Colo., 1990.
- (36) Offermann, D., and A. Drescher, Atomic oxygen densities in the lower thermosphere as derived from in situ 5577-Å night airglow and mass spectrometer measurements, *J. Geophys. Res.*, 78, 6690, 1973.
- (38) Peterson, A. W. , Airglow events visible to the naked eye, *Appl. Opt.*, 18, 3390, 1979.

- (39) Peterson, A. W., and L. M. Kieffaber, Infrared photography of OH airglow structures, *Nature*, 244, 92, 1973.
- (40) Röttger, J., Traveling disturbances in the equatorial ionosphere and their association with penetrative cumulus convection, *J. Atmos. Terr. Phys.*, 39, 987, 1977.
- (41) Ryan, E. H., Critical layer directional filtering of atmospheric gravity waves: A comparison of airglow observation and a wind profile model, M.S. thesis, The University of Cincinnati, Ohio 1991.
- (42) Ryan, E. H., and T. F. Tuan, Gravity waves blocking by critical layers, in paper presented at Middle Atmosphere Periodic Structure and Associated Radiance (MAPSTAR) Meeting, Air Force Geophysics Laboratory, Boston, Mass., April 22-23, 1991.
- (43) Taylor, M. J., and R. Edwards, Observations of short period mesospheric wave patterns: In situ or tropospheric wave generation?, *Geophys. Res. Lett.*, 18, 1337, 1991.
- (44) Taylor, M. J., and M. A. Hapgood, Identification of a thunderstorm as a source of short period gravity waves in the upper atmospheric nightglow emissions, *Planet. Space Sci.*, 36(10), 975, 1988.
- (45) Taylor, M. J., and K. Henriksen, Gravity wave studies at polar latitudes, in *Electromagnetic Coupling in the Polar Cleft and Caps*, edited by P. E. Sandholt, and A. Egeland, Kluwer Academic Pub., Dordrecht, 421, 1989.
- (46) Taylor, M. J., and M. J. Hill, Near-infrared imaging of hydroxyl wave structure over an ocean site at low latitudes, *Geophys. Res. Lett.*, 18, 1333, 1991.
- (47) Taylor, M. J., M. A. Hapgood, and P. Rothwell, Observations of gravity wave propagation in the OH (557.7 nm), Na (589.2 nm) and near infrared OH nightglow emissions, *Planet. Space Sci.*, 35, 413, 1987.
- (48) Taylor, M. J., P. J. Espy, D. J. Baker, R. J. Sica, P. C. Neal, and W. R. Pendelton, Jr., Simultaneous intensity, temperature, and imaging measurements of short period wave structure in the OH nightglow emissions, *Planet. Space Sci.*, 39, 1171, 1991a.
- (49) Taylor, M. J., D. N. Turnbull, and R. P. Lowe, Coincident imaging and spectrometric observations of zenith OH nightglow structure, *Geophys. Res.*

Lett., 18, 1349, 1991b.

(50) Wang, D. Y., and T. F. Tuan, Brunt-Doppler ducting of small-period gravity waves, *J. Geophys. Res.*, 93(A9), 9916, 1988.

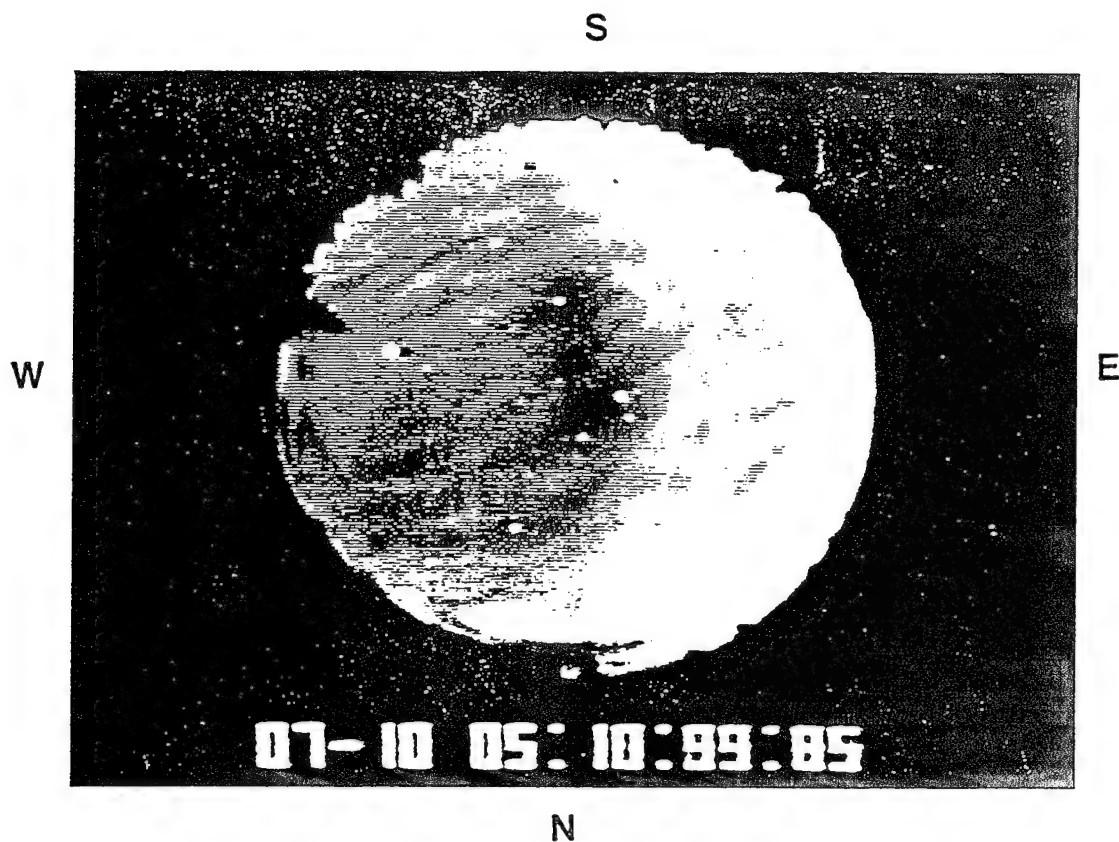


Figure 1. All-sky image showing coherent near-infrared (NIR) wave structure extending over the whole camera field. Geographic north appears at the bottom of the picture. The data were obtained on July 10 at 0510 UT using an integration time of 1.5 s. Similar waveforms were also imaged in the OI (557.7 nm) nightglow emission and to the north several bands were visible at low elevation to the dark adapted eye. (Note the dark region near the center of the image is due to a defect in the camera tube.)

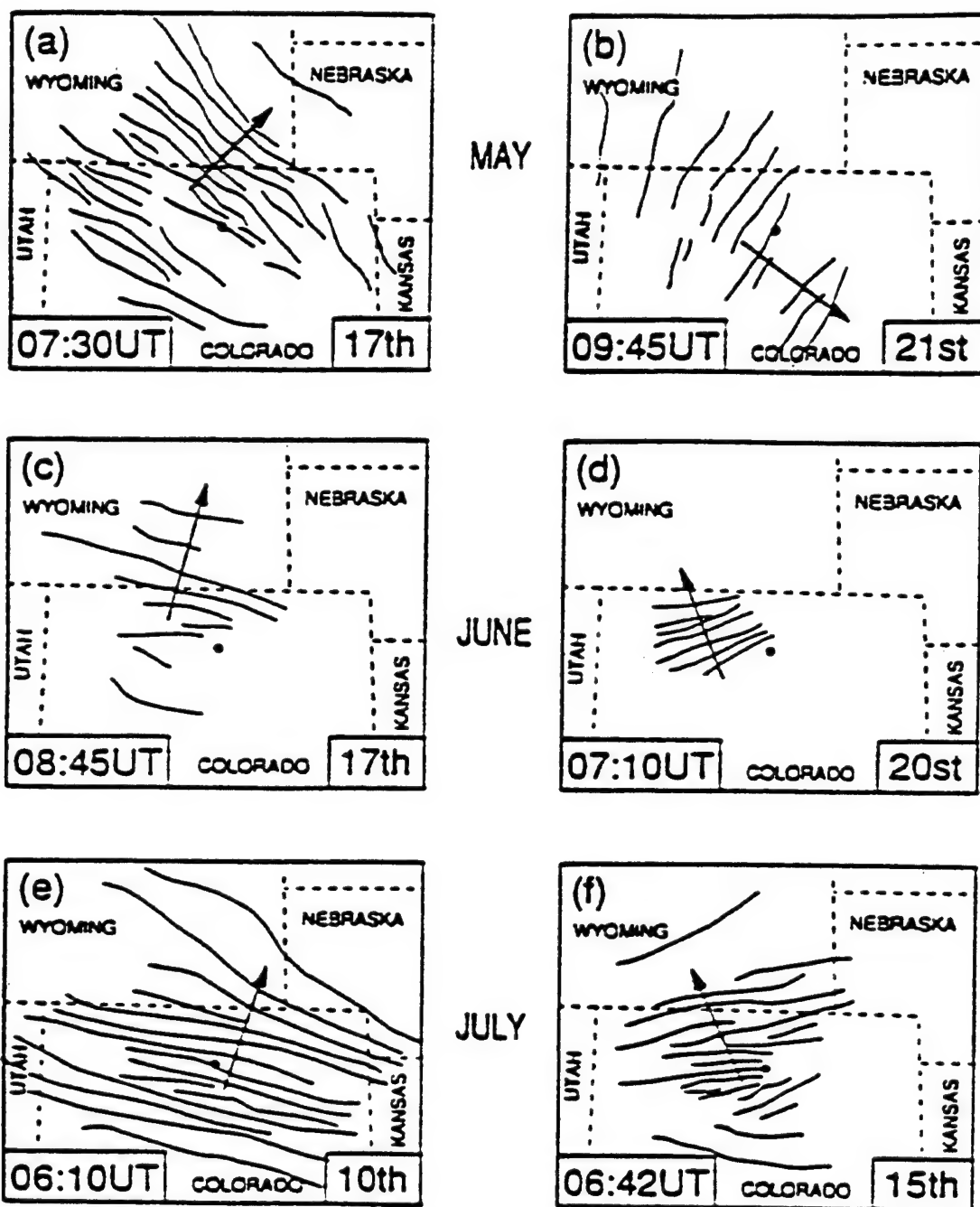


Figure 2. Ground maps showing the geographic location and orientation of six OH wave patterns (two for each month). The black spot near the center of each map marks the location of the optical site and the arrows show the direction of motion of the displays. A total of 22 displays were recorded during the campaign. The maps were plotted assuming an emission altitude of 87 km.

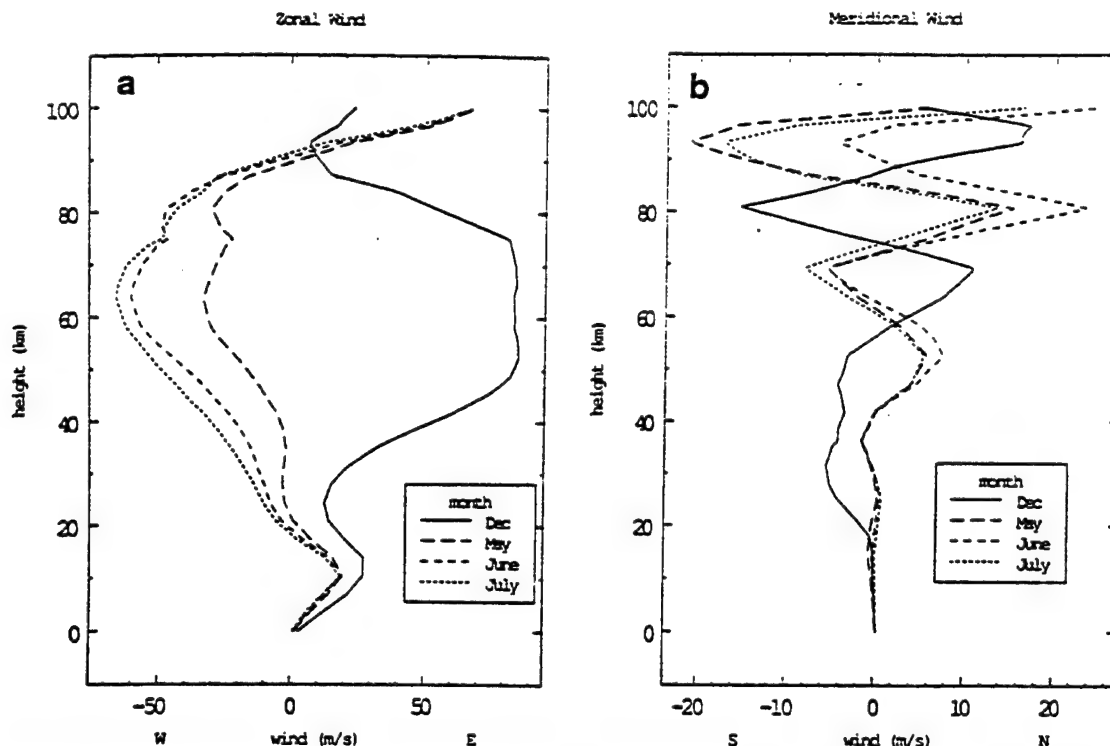


Figure 3. Model results showing (a) the total zonal wind component and (b) the total meridional wind component as a function of height for December, May, June, and July at local midnight. Note the difference in scales between the zonal and meridional winds. (Unless otherwise stated, all of the plots presented here were computed for the optical site at local midnight (0600 UT).)

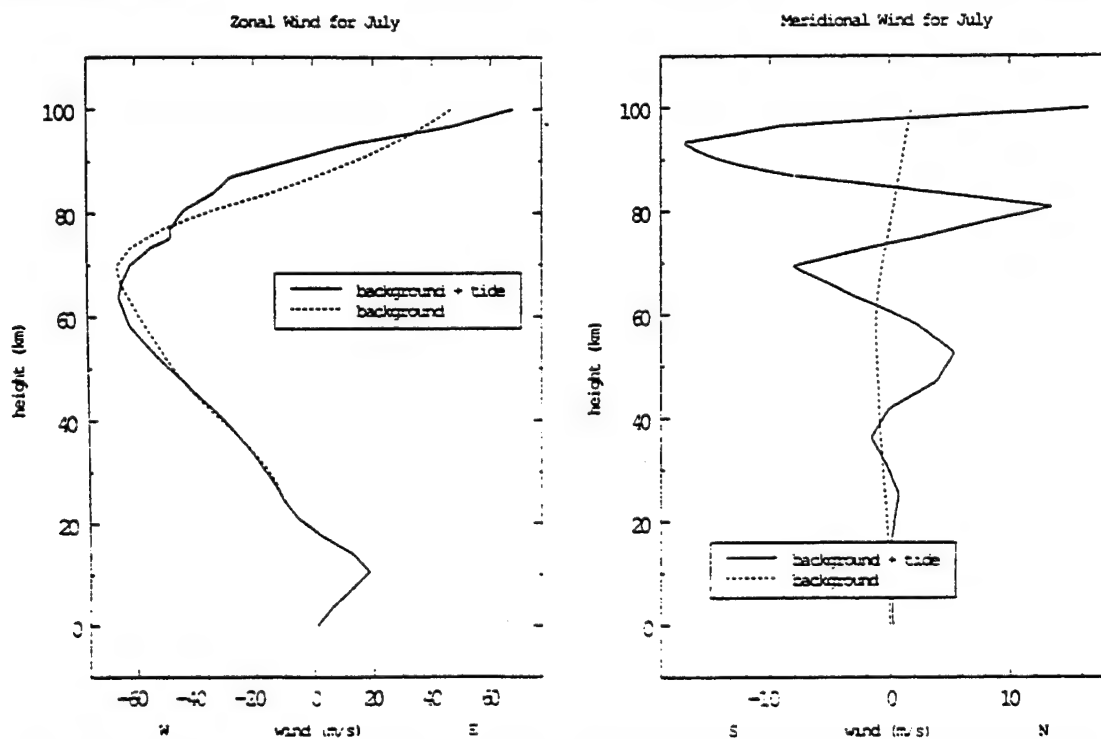


Figure 4. Zonal and meridional wind plots showing the effect of the sum tidal modes on the total wind component (i.e., background plus tides). The zonal winds are dominated by the background component, but the meridional winds vary significantly with the tidal motions.

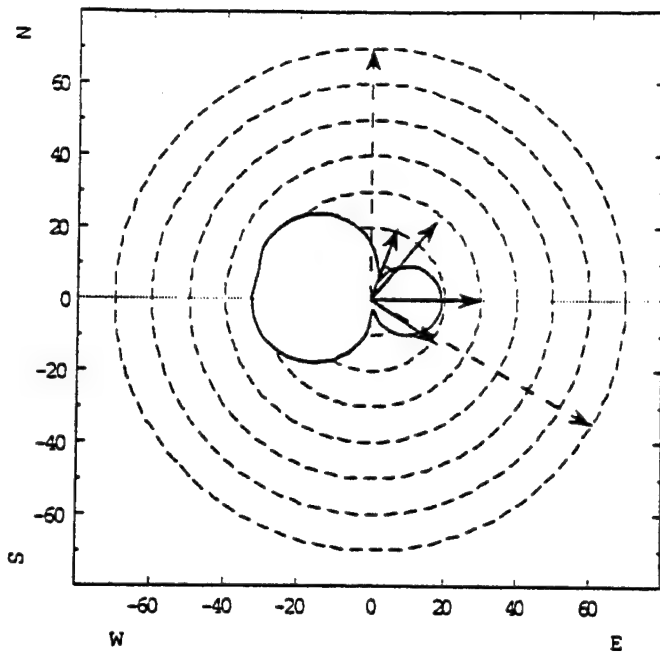


Figure 5. Blocking diagram for May at 85 km. The shaded area indicates the magnitude and direction of the restricted region for wave propagation to OH heights. The solid arrows show the magnitude and direction of the wave motions observed during this month, while the dashed arrows indicate direction only.

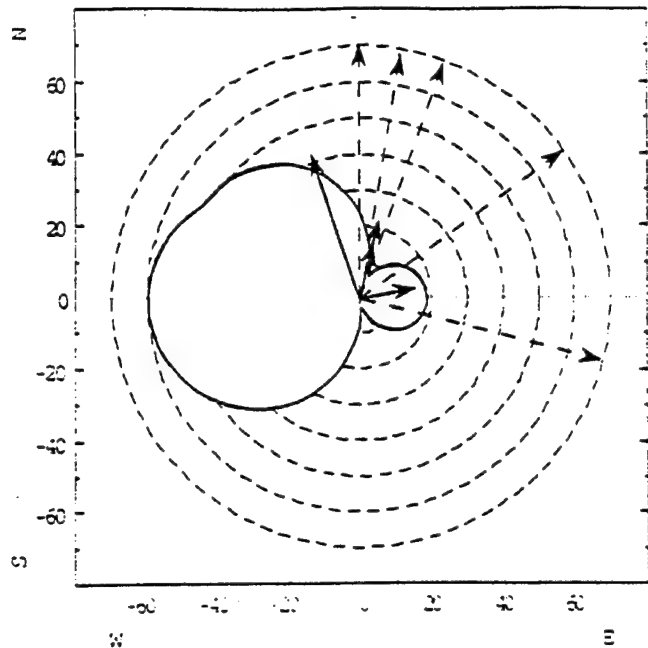


Figure 6. Blocking diagram for June at 85 km. For comparison the results are plotted on the same scale as Figure 5. Frequent changes in the observing conditions during this month limited the velocity measurements of several displays to direction only.

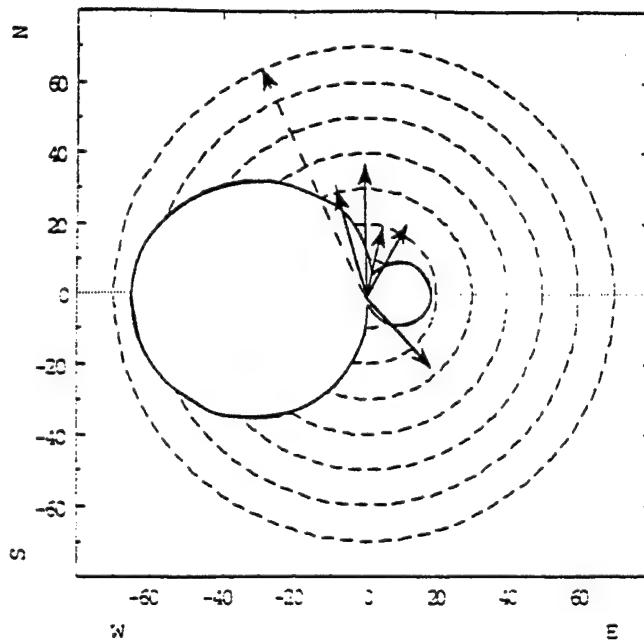


Figure 7. Blocking diagram for July at 85 km. All but one of the wave patterns observed during this period were restricted in azimuth range to $\pm 30^\circ$ N.

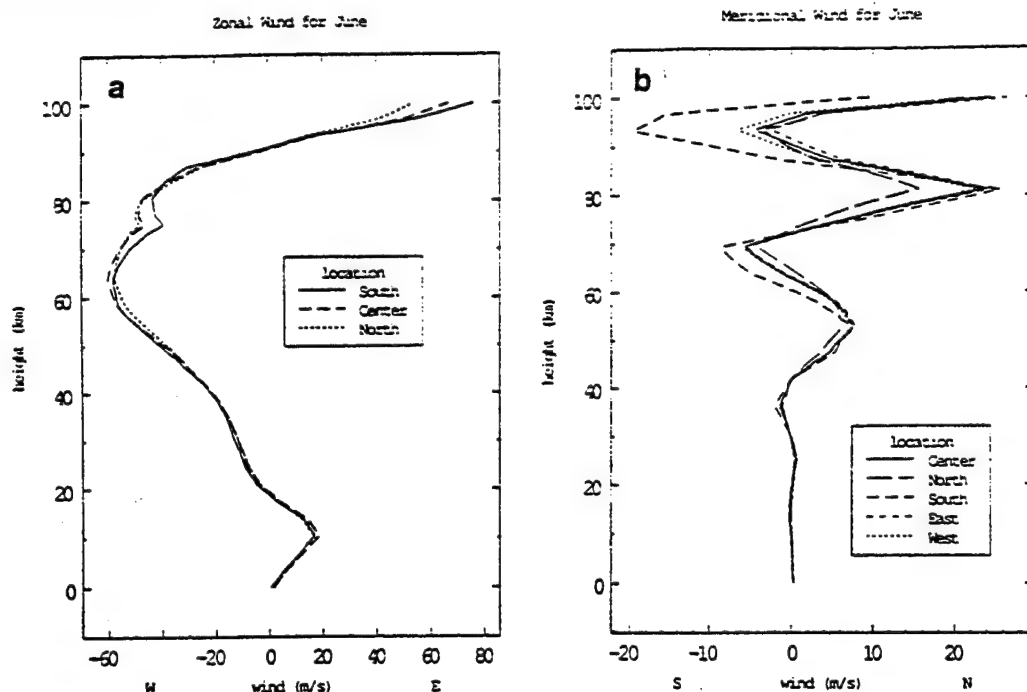


Figure 8. Model results showing the effect of changing the location of the wind profile calculations on (a) the total zonal and (b) the total meridional components. The data were computed for points $\pm 4^\circ$ in latitude and longitude to the north, south, east and west of the optical site.

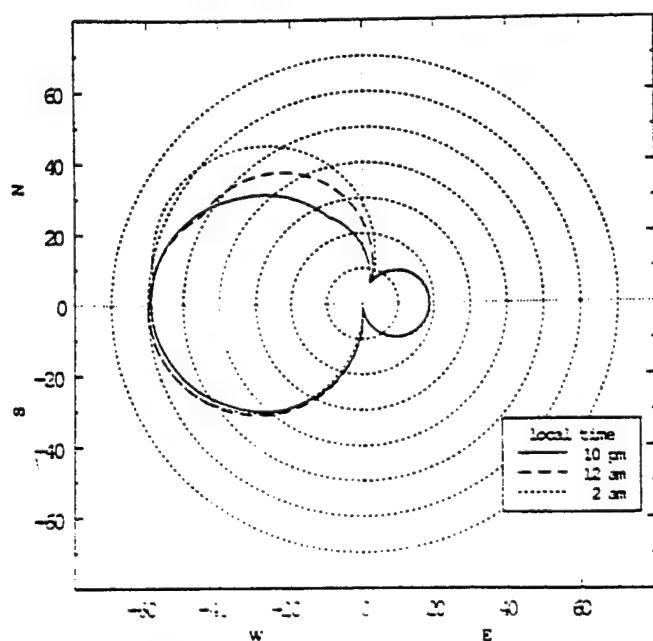


Figure 9. Blocking diagrams for June at 85 km showing the short term effects of tidal mode changes on the location of the restricted areas for wave propagation. Three local times are shown corresponding to 0400, 0600, and 0800 UT.

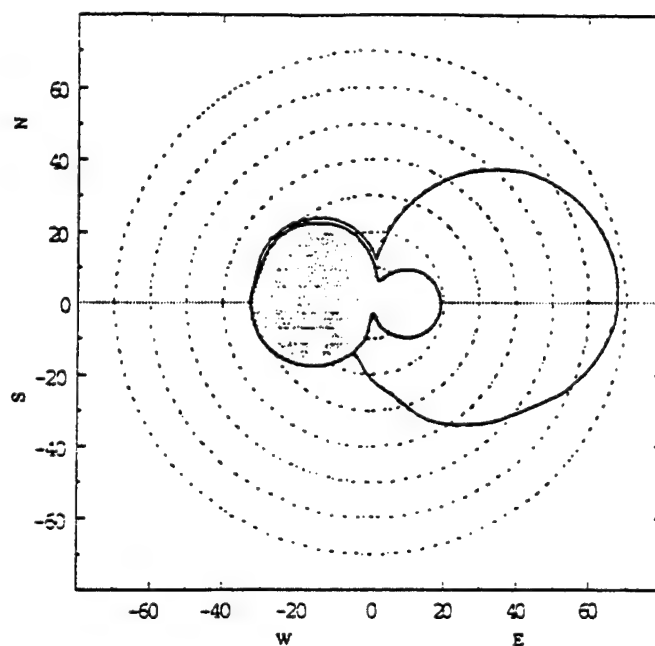


Figure 10. Blocking diagrams for May showing the effect of changing the height of the investigation on the location and shape of the restricted areas. Two height levels at 80 and 100 km are shown. The 80 km plot (dark shaded area) is very similar to that of Figure 5. However, the 100 km plot (light shaded area) shows a marked increase in the blocking area to the east. Any waves propagating upward toward the east at OH altitudes will be strongly filtered before they reach this height.

TABLE 1. Colorado Campaign 1988 OH Data Analysis

Date UT	Day (UT) Number Velocity	Wave Azimuth $\pm 5^\circ$	Observed Phase Speed m/s
May 13	134	90	30 ± 2
May 14	135	120	
May 15	136	0	
May 16	137	20	21 ± 2
May 17	138	40	28 ± 2
May 21	142	125	22 ± 4
June 09	161	20	
June 12	164	10	
June 15	167	0	
June 16	168	105	
June 17	169	15	22 ± 1
June 18	171	55	
June 20	172a	15	5 ± 2
	172b	340	42 ± 2
June 21	173a	80	18 ± 3
	173b	20	14 ± 3
July 10	192	15	20 ± 1
July 12	194	30	23 ± 3
July 15	197	335	
July 16	198	140	28 ± 2
July 17	199	345	32 ± 4
July 18	200	0	37 ± 3

List of the azimuth of the wave motions (i.e., the normal to the wave fronts) and their observed phase speeds for the 23 displays recorded during the campaign. On two occasions (June 20 and June 21) two patterns were observed during the course of the night.

4 The Effects of Dissipation on Gravity waves in the Critical Layer Region for Stable and Unstable background Winds; Realistic Background Atmosphere and Winds

Introduction

The subject of gravity-wave critical-layer interaction has received much attention [1-5]. In all these papers the attention has been focused on the mechanisms for the interaction and the excitation of new gravity wave modes. Very little attention has been paid to the effect of the interaction on the original wave, including the downward reflected wave below the critical layer. It is our purpose to determine, through phenomenology, the solution for the original wave, the magnitude of its reflection, its variation with the horizontal phase velocity and the direction of wind propagation, the effects of the absorptive loss on the wave and on over-reflection. The investigation will make use of realistic background atmosphere and wind profiles.

Much of the previous work on the critical layer has made use of the WKB approximation [6] for the incident wave, which basically neglects reflections. As the critical layer is approached, the incident wave is absorbed by the following diverse mechanisms: (a) frequency broadening due to nonlinear wave growth; (b) turbulence generated by convective instability; (c) dissipation from viscosity and heat conduction; (d) absorption into the mean flow; (e) excitation of new modes. In view of the fact that all such wave absorption takes place over a vertical distance short compared with the incident vertical wavelength, we would expect from basic physics that the reflections from the critical-layer region should be significant under certain circumstances (e.g. large but still stable instantaneously observed wind gradients).

The fact that absorptive losses can create significant reflections has been demonstrated in atmospheric science by Richmond [7] who has shown that for large-scale gravity waves the wave absorption

from viscosity and heat conduction at high altitudes can produce so much downward reflection on an upward propagating gravity wave that some degree of gravity-wave ducting can actually occur. In that paper a three-layer model was used to simulate the viscous and heat conduction absorptions.

We now wish to determine the reflections from similar absorptive losses plus the additional loss from instability and turbulence for the critical layer case. To begin, we reformulate the coupled hydrodynamic equations including horizontal winds into a single second-order Sturm-Liouville equation which allows only for losses through the mean flow (i.e. (d) of above) so that the total energy flux in the presence of horizontal winds is conserved. The latter may also be considered as another verification of the Eliassen and Palm Theorem. All additional losses can be parametrized by simply adding a single absorption parameter very similar to the optical model [6]. The optical potential treatment has been successfully used in nuclear physics and unsuccessfully in atomic physics, because, for the latter, the absorption is very structured. Owing to the large variety of mechanisms of dissipation in the critical layer region, the problem in this study bear many similarities to the scattering problems in nuclear physics, and thus the same technique may be used.

In scattering theory, one wants to know what happens to a particular scattering channel (e.g., the elastic channel with no loss of incident energy or the inelastic channel with an excitation of the target which can be a nucleus, an atom or, as in our case, a mean flow) without having to solve the entire problem which often involves intractable nonlinear field equations. The optical model is then used phenomenologically to replace as much as possible the effects of the physics of the unwanted channels on the particular channel of interest. Most important of all, the optical model reduces an intractable nonlinear system to a tractable linear problem which focuses only on one channel. Our interest is in setting limits on the reflections of the original incident wave with the original incident

wave parameters (i.e. the elastic scattering) produced by gravity-wave and critical-layer interaction which is highly nonlinear. To model the interaction we introduce the optical potential to phenomenologically take care of the myriad of relatively unstructured losses just mentioned. The physical justification for this comes from the narrowness of the vertical range over which the losses occur as compared with the incident vertical wavelength. This will allow us to adopt a simple two-parameter potential to calculate the reflection of gravity waves. The optical potential then not only replaces the various diverse dissipation mechanisms for the reflection of the incident wave, but, for the case of unstable background winds, can also serve to generate newly created modes in the incident channel.

We use the method of Geller et al (1975) for computing the width of the instability region, which is small compared with the average vertical wavelength of the incident gravity wave. Due to the relatively long wavelength, the exact functional form of the potential no longer matters and we choose a two parameter potential, namely the strength (labeled W_0) and the range of the optical potential. As the range can be estimated, the only free parameter left then is W_0 . We shall vary this parameter to give us a range of reflection coefficients and we will show that the actual reflection from the critical level itself plays almost no role for most reasonable values of W_0 .

In our calculation we use COSPAR atmospheric models with NCAR-CEDAR (1990) wind profiles modified by the tidal-wave model of Forbes et al (1982). Because of the singularity of critical layer, any numerical calculation will fail in that region. But since the instability region is very small compared with the variation in the background atmosphere, as a good approximation, we can assume that the background is isothermal within the instability region. This approximation leads to analytic solutions to the linearized hydrodynamic equations. We join the analytical solution to the numerical solution at the lower end of the instability region. Once

the gravity-wave solutions are known everywhere, we can obtain the reflection coefficients and the response of airglow to a gravity wave in the presence of critical layers. That the critical layers may have a strong effect on gravity-wave propagation has already been shown through the airglow observations of Taylor et al (1993) based on the "blocking diagrams" of Ryan (1991). It is part of our wish is to construct a gravity-wave model in the presence of the critical layer.

Based on our study we can conclude that (1) with any reasonable absorption from nonlinearity and turbulence and for stable background wind, the reflection and absorption, in most instances, take place before the wave reaches the critical level and, therefore, the total reflection from the critical-layer region is in fact independent of the reflection parameter at the critical level; (2) the gravity-wave critical layer interaction in the presence of an unstable wind can result in wave emission and growth rather than wave absorption. Thus, instead of a "sink" for absorbing gravity waves, critical layer becomes a "source" for creating gravity waves. In such case the reflection coefficient is greater than unity and over-reflection can occur (Jones, (1968)); (3) resonance absorption can occur in which the reflections from the critical layer and from the background interfere destructively; (4) for some observed wind profiles with large wind shear the reflection coefficient can be very significant.

Mathematical Formulation

The linearized hydrodynamical equations in the presence of horizontal winds [14] are given by:

$$\frac{d\psi}{dz} - \eta\psi = \frac{i}{\Omega}(\omega_b^2 - \Omega^2)\Phi \quad (1)$$

$$\frac{d\Phi}{dz} + \left(\eta + \frac{\kappa_h}{\Omega} \frac{\partial V_o}{\partial z}\right) \phi = i \left(\frac{\kappa_h}{\Omega^2} - \frac{1}{c^2}\right) \quad (2)$$

where ω = observed gravity-wave frequency

v_h = horizontal phase velocity

$\omega_b = -g \left(\frac{1}{\rho_o} \frac{d\rho_o}{dz} + \frac{g}{c^2} \right) =$ Brunt frequency

$\Psi = \frac{\omega \Delta \rho}{\rho_o^{1/2}} =$ pressure variation, $\Delta \rho$, normalized to include

the background density variation

$\Phi = \rho_o^{1/2} \omega \Delta \omega =$ vertical velocity variation, $\Delta \rho$, also

normalized in a similar way

$\Omega = \omega - \bar{\kappa}_h \cdot \bar{V}_o = \omega - \kappa_h V_o = \omega \left(1 - \frac{V_o}{v_h} \right) =$ intrinsic

Doppler shifted frequency

$\bar{\kappa}$ = wave vector (κ_h = its horizontal component)

$V_o =$ horizontal background velocity along propagation direction

$$\eta = - \left(\frac{1}{2} \frac{1}{\rho_o} \frac{d\rho_o}{dz} + \frac{g}{c^2} \right)$$

An oscillatory factor, $\exp(i\omega t - ik_h x)$ is dropped out of Ψ and Φ in all equations. The coupled equations given by (1) and (2) can be combined to yield

$$\frac{d}{dz} \left(\frac{1}{\omega_b^2 - \Omega^2} \frac{\partial}{\partial z} \right) \Psi - \left[\frac{d}{dz} \left(\frac{\eta}{\omega_b^2 - \Omega^2} \right) + \frac{\eta^2}{\omega_b^2 - \Omega^2} + \frac{1}{c^2} - \frac{\kappa_x^2}{\Omega^2} \right] \Psi = 0 \quad (3)$$

We will use numerical method in finding the gravity-wave solutions to eq. (3). But in the vicinity of the critical level ($\Omega = 0$) eq. (3) becomes singular, and the numerical method can not be applied. To solve this problem, we assume that the background atmosphere in the neighborhood of the critical level is isothermal and that the wind shear there is constant and use analytical solutions which can then be joined to the numerical solutions outside the critical-layer region. Since the instability region ranges from several hundred meters to a couple of kilometers for most gravity waves of interest, both the background temperature and the wind shear may be assumed to be constant over such a short vertical region. The wind profile in the immediate vicinity of the critical layer is then given by $V_{0h}(z) = V_0 + \beta(z - z_0)$ where β is the constant wind gradient.

With this assumption, eq. (3) in the vicinity of critical layer becomes

$$\frac{d}{dz} \frac{1}{1-x^2} \frac{d\Psi}{dx} + \left[\frac{\lambda}{x^2} - \frac{\sigma^2}{1-x^2} + \frac{2\sigma x}{(1-x^2)^2} - \nu \right] \Psi = 0 \quad (4)$$

where $x = \frac{\Omega}{\omega_b} = \frac{\omega}{\omega_b} \left(1 - \frac{V_{0h}(z)}{v_h} \right)$ is the new coordinate introduced;

$x=0$ corresponds to $\Omega=0$ where the critical level occurs, and x is positive going downwards.

$$\nu = \frac{\omega_b^4}{k_h^2 \beta^2 c^2} = \text{eigenvalue (dimensionless)}$$

$$\sigma = \frac{\omega_b \eta}{k_h \beta}$$

$$\lambda = \frac{\omega_b^2}{\beta^2} = \text{background Richardson number (dimensionless)}$$

$$\beta = \frac{\partial V_{0h}}{\partial z} = \text{wind gradient or wind shear and is constant}$$

Eq. (4) is a Sturm-Liouville equation which includes the loss to the mean flow. The equation allows for analytic solutions in the neighborhood of the critical level ($x = 0$) and also guarantees that any absorption parameter (optical potential) we add to the equation would represent additional losses (other than losses to the mean flow) to the incident wave. By multiplying (4) from the left by Ψ^* and the Hermitian adjoint of (4) by Ψ , subtracting the latter from the former and integrating from $x=a$ to $x=b$, where a and b are two arbitrary positions, we obtain:

$$\left[\Psi^* \frac{1}{1-x^2} \frac{d\Psi}{dx} - \Psi \frac{1}{1-x^2} \frac{d\Psi^*}{dx} \right]_a^b = 0 \quad (5)$$

Equation (5) holds because the eigenvalue of a Sturm-Liouville equation is real. Since a and b are arbitrary positions, we conclude:

$$\Psi^* \frac{1}{1-x^2} \frac{d\Psi}{dx} - \Psi \frac{1}{1-x^2} \frac{d\Psi^*}{dx} = \text{constant} \quad (6)$$

Rewriting the first equation in (1) in terms of x for the immediate neighbourhood of the critical layer and multiplying the result from the left by $\Psi^*/(1-x^2)$ and its Hermitian adjoint by $\Psi/(1-x^2)$ and subtracting the latter from the former, we obtain:

$$\Psi^* \frac{1}{1-x^2} \frac{d\Psi}{dx} - \Psi \frac{1}{1-x^2} \frac{d\Psi^*}{dx} = \frac{-i\omega_b^2 v_h^2 (\Delta p^* \Delta \omega + \Delta p \Delta \omega^*)}{\beta (v_h - V_o)} \quad (7)$$

In eq. (7) we have used the fact that

$$\begin{aligned} \Psi^* \Phi &= \omega^2 \Delta p^* \Delta w \\ \Psi \phi^* &= \omega^2 \Delta p \Delta w^* \end{aligned} \quad (8)$$

From eq. (7) we obtain:

$$\Psi^* \frac{1}{1-x^2} \frac{d\Psi}{dx} - \Psi \frac{1}{1-x^2} \frac{d\Psi^*}{dx} = -\frac{4i\omega_b^3 v_h}{\beta} \left[\frac{\langle \Delta p^* \Delta w \rangle_t}{1 - \frac{V_{0h}}{v_h}} \right] \quad (9)$$

where the bracket term on the right is constant from (7). It can be shown from horizontal momentum conservation that the total time-averaged energy flux in the presence of horizontal winds, F_T , is given by

$$F_T = \langle \Delta p^* \Delta w \rangle_t + \rho_0 \langle \Delta u^* \Delta w \rangle_t V_{0h} = \frac{\langle \Delta p^* \Delta w \rangle_t}{1 - \frac{V_{0h}}{v_h}} \quad (10)$$

Equations (9) and (10) can be recognized as a direct consequence of the Eliasson and Palm theorems for an inviscid atmosphere where the only possible loss (or gain) of energy for the gravity wave is with the mean flow.

So far our mathematical formulation has described only the loss mechanism (d), the absorption into the mean flow. We will not consider mechanism (c), since dissipation from viscosity and heat conduction are very small except very close to the critical level where their effects will be modeled by a complex parameter, R_c , the "reflection" coefficient at the critical level. The other loss mechanisms including the important losses due to instability and turbulence will be described phenomenologically by incorporating an optical potential in (4).

In the present treatment the vertical wave length of the incident gravity wave is typically of the order of low tens of kilometers, while the vertical range of the region in which the gravity wave is nonlinear and the atmosphere is convectively unstable is of the order of only a couple of kilometers [5]. Thus, the effective range over which strong absorption occurs is considerably less than the wavelength of the incident gravity wave. From basic scattering theory this means that the scattering and, hence, the reflection from the strongly interacting region is relatively independent of the "shape" of the optical model "potential" and the entire scattering process can be described by a simple two-parameter optical "potential".

We will allow our choice to be guided by the worst-case scenario, that is the most singular behavior at the critical layer, which arises from the nonlinear convective derivative term in the momentum equation. to lowest order, this term is given by

$$\rho(\bar{v} \cdot \bar{\nabla})\bar{v} \sim K \frac{\Psi}{x^2} \quad (11)$$

where K is a dimensional constant. The expression on the right-hand side of (11) is obtained by substituting the linear solution for v and ρ on the left of (11) and using the known behavior of Ψ [1] near the critical level. Thus, we may choose the following optical potential:

$$\begin{aligned} V_{\text{optical}} &= \frac{iW_0}{x^2} & (x < x_m) \\ V_{\text{optical}} &= 0 & (x > x_m) \end{aligned} \quad (12)$$

for the potential depth. x_m , corresponding to z_m , is the position where the instability begins and 0 to x_m provides a measure for the range over which the absorption is active. W_0 and x_m constitute the two parameters of our model. However, as will be shown in the next section, x_m can be independently determined, leaving us with a single-parameter theory.

Since eq. (4) guarantees the conservation of FT we can take care of any dissipative loss by phenomenologically adding an "optical potential", or absorptive potential to (4) using (11) as the potential model [6]. Equation (4) then becomes

$$\frac{d}{dx} \frac{1}{1-x^2} \frac{d\Psi}{dx} + \left[\frac{\lambda + iW_0}{x^2} - \frac{\sigma^2}{1-x^2} + \frac{2\sigma x}{(1-x^2)} - \nu \right] \Psi = 0 \quad (13)$$

Since $x_m \ll 1$, in the region of $0 < x < x_m$ the analytic solution to the lowest order is good enough for our purpose. The solution to (7) depends on whether the background wind profile is stable ($\lambda > 1/4$) or unstable ($\lambda < 1/4$). At any arbitrary but fixed location, $x = \underline{x}$, we can find plane wave solutions in the immediate vicinity of \underline{x} , i.e., $x = \underline{x} + \delta$ where $\delta/\underline{x} \ll 1$.

We list the solutions to the lowest order in x in Table I for $0 < x < x_m$.

Table I

	$\lambda > 1/4$	$\lambda < 1/4$
Ψ_+	$x^{1/2-\bar{\beta}/2} e^{i(\bar{\alpha} \log_e x)/2}$ $x^{1/2-\bar{\beta}/2} e^{i(\bar{\alpha} \log_e \underline{x})/2} e^{ik\delta}$	$x^{1/2-\bar{\beta}/2} e^{i(\bar{\alpha} \log_e x)/2}$ $x^{1/2-\bar{\beta}/2} e^{i(\bar{\alpha} \log_e \underline{x})/2} e^{ik\delta}$
Ψ_-	$x^{1/2+\bar{\beta}/2} e^{-i(\bar{\alpha} \log_e x)/2}$ $x^{1/2+\bar{\beta}/2} e^{-i(\bar{\alpha} \log_e \underline{x})/2} e^{-ik\delta}$	$x^{1/2+\bar{\beta}/2} e^{-i(\bar{\alpha} \log_e x)/2}$ $x^{1/2+\bar{\beta}/2} e^{-i(\bar{\alpha} \log_e \underline{x})/2} e^{-ik\delta}$

where

$$\bar{\alpha} = \left[(4\lambda - 1)^2 + 16W_0^2 \right]^{1/4} \cos\left(\frac{\phi}{2}\right)$$

$$\bar{\beta} = \left[(4\lambda - 1)^2 + 16W_0^2 \right]^{1/4} \sin\left(\frac{\phi}{2}\right)$$

$$\phi = \tan^{-1} \frac{4W_0}{4\lambda - 1}$$

$$k = \left(\frac{\bar{\alpha}}{2\underline{x}} \right) = \text{instantaneous wave vector at } x = \underline{x}$$

Ψ_+ = upgoing (energy) wave

Ψ_- = downgoing (energy) wave

In Table I, the top line of each row gives solutions for $\lambda > 1/4$ and $\lambda < 1/4$. The bottom line of each row gives the leading term in the expansion of these solutions about any arbitrary but fixed x . We see right away that the instantaneous vertical wavelength ($\approx 2\pi/k$) goes to zero as $x \rightarrow 0$ at the critical point, as is well known.

The behavior of upgoing and downgoing waves depend entirely on the argument, ϕ , of the cosine/sine function appearing in $\bar{\alpha}$ and $\bar{\beta}$ for stable and unstable background winds. Figure 1 shows the argument, ϕ . Since W_0 is always negative (for absorption), we see that for stable background winds ($\lambda > 1/4$), ϕ , the argument for the arctangent function, is in the second quadrant and therefore $\bar{\alpha} < 0$ and $\bar{\beta} > 0$. In the limit as W_0 goes to zero, $\phi/2$ goes to π , $\bar{\alpha} = -(4\lambda - 1)^{1/2} = -\mu$ and $\bar{\beta} = 0$. For unstable background winds ($\lambda < 1/4$) and ϕ , the argument for the arctangent, is in the third quadrant, and thus, $\bar{\alpha} < 0$ and $\bar{\beta} > 0$. In the limit as W_0 goes to zero, ϕ goes to π , $\bar{\alpha}$ goes to zero and $\bar{\beta}$ goes to $(1 - 4\lambda)^{1/2}$. Thus, for both stable and background winds $k < 0$ and since x is positive going downwards, $\exp[ik\delta]$ is downward in phase progression and hence upwards in energy propagation. By the same argument, $\exp[-ik\delta]$ is upwards in phase progression and downwards in energy propagation.

The most interesting phenomenon occurs for the case of unstable background winds when $4\lambda - 1$ (Figure 1) becomes negative. We can set $4\lambda - 1 = -e = -(4\lambda' - 1)$ where $\lambda < 1/4$, $e > 0$, and $\lambda' > 1/4$. Thus,

$$\tan \phi = \frac{4W_0}{4\lambda - 1} = \frac{-4W_0}{e} = \frac{-4W_0}{4\lambda' - 1} \quad (14)$$

This means that an unstable background wind with a negative optical potential, $W_0 < 0$, is equivalent to a stable background wind with a positive optical potential, $W_0 < 0$. In this way, instead of an absorbing potential which acts as a sink and takes energy out of the gravity wave, we now have a source which puts energy into the gravity wave. The reflection coefficient is greater than unity and over-reflection occurs (Jones, (1968)). When this happens, the ultimate source of energy is, of course, the background wind.

We now investigate the explicit behavior of the constant in the Eliassen and Palm Theorems given by Eq. (10). By substituting the lowest order solutions of Eq. (4) into the left-hand side of Eq. (9), we obtain for $x \ll 1$:

$$\frac{\langle \Delta p \Delta w \rangle_i}{1 - \frac{V_0}{v_h}} = \frac{|A|^2 \mu (1 - |R_c|^2)}{4\lambda^{1/2} \omega_b^2 v_h} \quad (15)$$

for stable background winds and

$$\frac{\langle \Delta p \Delta w \rangle}{1 - \frac{V_0}{v_h}} = - \frac{|A|^2 \bar{\mu} |R_c| \sin \chi}{2\lambda^{1/2} \omega_b^2 v_h} \quad (16)$$

for unstable background winds. Here, A is the wave amplitude for Ψ in Eqs. (15) and (16), $\tilde{\mu}=(1-4\lambda)^{1/2}$ in Eq. (16) and R_c is the complex reflection parameter at the critical level given by

$$R_c = |R_c| e^{i\chi}$$

From Eq. (14), we see that over-reflection can occur only if χ has such value that $\sin \chi < 0$. We also note that for stable background wind

$$R_c = 1 \rightarrow \frac{\langle \Delta p \Delta w \rangle_t}{1 - \frac{V_0}{v_h}} = 0$$

This merely means that with perfect reflection at the critical level, a standing wave along the vertical direction is produced and the net energy flux is zero.

Important points of interest in Eqs. (15) and (16) are that the time averaged energy flux depends on : (1) the steepness of the vertical wind gradient; (2) the period of the gravity wave (the greater the period, the greater the absorption into the mean flow); (3) the inverse of horizontal phase velocity (the smaller scale gravity waves are absorbed more) and (4) the altitude (larger Brunt periods at higher altitude mean that the absorption into the mean flow increases with altitude).

With a nonvanishing W_0 , we proceed in a similar fashion for the derivation of (9), but start from Eq. (13) rather than Eq. (4). The result is

$$\Psi^* \frac{1}{1-x^2} \frac{d\Psi}{dx} - \Psi \frac{1}{1-x^2} \frac{d\Psi}{dx} + 2iW_0 F(x) = \text{constant } t = iN \quad (17)$$

where

$$F(x) = \int \frac{|\psi|^2}{x'} dx'$$

and

$$N - 2W_0 F(x) = \frac{-4\omega_b^3 v_h^2 \langle \Delta p \Delta w \rangle}{\beta \left(1 - \frac{V_0}{v_h}\right)} \quad (18)$$

term (i.e. $2W_0 F(x)$) to the constant N . Eq. (18) also provides a generalization to the Eliassen and Palm theorems for the case when there are dissipative absorption mechanisms, i.e. absorption other than into the mean flow.

The same technique used to derive Eqs. (15) and (16) can be used to show that (for $x \ll 1$) with stable/unstable background

$$\frac{\langle \Delta p \Delta w \rangle_t}{1 - \frac{V_0}{v_h}} = - \frac{|A|^2 \left[\bar{\alpha} x^{-\bar{\beta}} + 2\bar{\beta} |R| \sin(\chi - \bar{\alpha} \log_e x) - \bar{\alpha} |R|^2 x^{\bar{\beta}} \right]}{4\lambda^{1/2} \omega_b^2 v_h} \quad (19)$$

In Eq. (19), the R.H.S. gives the behavior of the leading term of the energy flux. The parameter for reflection at the critical level, R_c , is replaced in the right-hand expressions by R , because, with the wave vector, k , given by the above expression, the reflection coefficient does not vary with x . It is easy to show that (19) reduces

to (15) for stable background winds when W_0 is made to approach zero, and to (16) for unstable background winds .

The behavior of Eq. (19) which includes absorption into channels other than just the mean flow is quite different from that of Eqs. (15) and (16) which only allow the absorption into the mean flow. In general, at any fixed height the greater the absorption into the other channels, the smaller the vertical energy flux which also means that less of the flux is available for conversion into systematic energy such as an increase in the local mean flow.

Reflection of incident wave

By matching the boundary conditions at x_m we can find the reflection coefficients of the gravity waves in the context of a multi-layer model. The numerical solutions within any layer centered about z can be approximated by upgoing and downgoing instantaneous plane waves at any position z

$$\Psi(z) = A(z)e^{ik_z(z-z)} + B(z)e^{-ik_z(z-z)} \quad (20)$$

where the k_z is the instantaneous vertical wave vector (or the vertical wave vector in the thin isothermal layer within the multi-layer model). The reflection coefficient R at arbitrary position z is given by

$$R(z) = \frac{|B(z)|}{|A(z)|} \quad (21)$$

By taking derivative of (20) with respect to z , we get

$$\Psi'(z) = ik_z A(z)e^{ik_z(z-z)} - ik_z B(z)e^{-ik_z(z-z)} \quad (22)$$

Combining (20) and (22) we obtain

$$R(z) = \frac{|ik_z \Psi - \Psi'|}{|ik_z \Psi + \Psi'|}$$

Figures 2(a), (b) and (c) show respectively the projected background wind profiles along the zonal, 45° to the zonal and 315°

to zonal directions. The normalized pressure wave amplitude, Ψ , the location of the critical level ($x=0$, or $z = z_c$), the range of the optical potential ($0 < x < x_m$, or $z_m < z < z_c$) where the absorption due to nonlinearity and gravity wave instability occurs, and the range ($x_m < x < x_0$, or $z_0 < z < z_m$) where the gravity wave reflection comes primarily from the wind gradient, are all indicated in Figure 2. In this report we shall only consider a gravity wave with a period of one-half an hour and propagating in the three directions. Figures 3(a), (b) and (c) show the reflection coefficients of gravity waves versus horizontal phase velocity for different R_c (the "reflection" coefficient at the critical level). From Figure 3 we can see that with the introduction of even modest absorption ($W_0 = -0.15\lambda$) the curves are almost identical, which means that the physical processes for reflection at the critical level ($z = z_c$) begin to lose their effectiveness. With $W_0 < -0.2\lambda$ (Figures 4(a), (b) and (c)) the total reflection coefficient becomes entirely independent of the physics at the critical level $x = 0$ ($z = z_c$), i.e., the same total reflection holds for any value of R_c with any amplitude and phase. The total reflection coefficient ranges from 5% to 25%. The minima (absorption resonance states) occur when the reflected gravity waves from critical level region and background interfere destructively. For isothermal background with constant background wind gradient, the phase of gravity waves near critical level is logarithmically dependent on x , the normalized distance from the critical level. The distance x_0 for a gravity wave with horizontal phase velocity v_h is proportional to v_h . Thus, the phase $\phi \propto \log(v_h)$. For every 2π change in phase we will get a minimum (or maximum). Thus, we have

$$\mu \log \frac{v_{h2}}{v_{h1}} = 2\pi \quad (23)$$

or

$$\frac{v_{h2}}{v_{h1}} = \text{constant}$$

So, for isothermal case, the minima occur more often for small scale gravity waves than for large scale gravity waves. Since this report is interested in the real atmosphere, we can not get the simple analytic relation between horizontal phase velocity and minima. We can provide qualitative explanations. The instantaneous wave vector k_z can be approximately written as

$$k_z \propto \sqrt{\frac{\omega_b^2 - \Omega^2}{\Omega^2} k_x^2 - \frac{\omega_a^2 - \Omega^2}{c^2}} \quad (24)$$

In the vicinity of the critical level, Ω is small, so the dominant term is $\frac{\omega_b}{\Omega} k_x$. Obviously larger ω_b produces larger k_z and short instantaneous wavelength and therefore more phase change. We would expect more resonance states for larger ω_b . Figure 5 shows the ω_b profile. We can see from it that ω_b has a peak at about 85km. In examining Figures 2 (a), (b) and (c) we see that above 40 m/sec, owing to the difference in the shapes of the projected wind profile, the critical level moves away from the peak ω_b values much faster with increasing horizontal phase velocity for the zonal ($a = 0$) wave propagation than for either of the other two propagating directions. This means that ω_b and hence k_z tends to be smaller for $a = 0$, giving us less absorption resonances per unit horizontal phase velocity.

With uniform ωb we would expect the distance between neighbouring minima to increase uniformly as horizontal phase velocity increases. As the presence of the peak will shorten the distance of neighboring minima, the two competing factors produce a more or less evenly separated minima for the reflection coefficient

Figures 6(a), (b) and (c) show what would happen when we vary the wind gradient as measured by the background Richardson's number, λ . It should be pointed out that for climatological wind-profile gradients, λ is of the order of about 40 and therefore very stable. For $\lambda \approx 1/4$ the wind profile is very steep and the maxima and minima occur very infrequently. In fact, within the phase speed range we work there is only one absorptive resonance. When the background is unstable, i.e., $\lambda \approx 1/4$, the total reflection coefficient can be greater than one and over-reflection occurs, as mentioned earlier. While the over-reflection is a well-known phenomenon [3], the present optical model treatment not only predicts the over-reflection (Figure 6), but also brings both over-reflection in an unstable background wind and under-reflection in a stable background wind into the same mathematical framework.

Observed wind profiles have sometimes been known to show far smaller background Richardson's number and a greater propensity for instability. In Figure 7 we have used the Na lidar observed meridional and zonal wind profiles for October 21, 1993 at Haleakala (Tao and Gardner, (1994)) to construct the projected wind profile along the direction of a simultaneously observed gravity

wave (Swenson et al, (1994)) propagating along an azimuthal angle of 330° to 340° with a phase speed of 30 to 35 m/sec and a period of 38 min. at about 10:30 UT. Using different W_0 , we plotted the reflection coefficient against phase speeds and found that it varies between 60 and 75%. Thus, while the highly stable climatological wind profiles can only produce reflections of the order of 10 to 25%, an observed profile can produce far greater reflections.

Figure 8 shows the behavior of the reflection coefficient as a function of W_0 for a fixed period of one-half hour and phase speed of 70 m/sec and using the same observed wind profiles (Tao and Gardner, (1994)). There are two competing effects involved: when the dissipation is relatively small, an increase in dissipation tends to absorb more of the G.W. and hence decrease the wave reflection; this is offset by the "suddenness" of the absorption which occurs at large $|W_0|$ and which increases reflection. Thus, one would expect that the reflection coefficient would at first decrease with increasing $|W_0|$ when the "suddenness factor" is small compared to the absorption factor, and then increase with $|W_0|$ when the reverse is true. The minimum occurs at about $W_0 = -0.2\lambda$. This also more or less coincides with the value of $|W_0|$ above which the reflection coefficient becomes independent of the reflection at the critical level.

Summary and Discussion

In this report we begin by investigating the limits on the total reflection from the critical layer by studying the scattering of incident gravity waves which suffer energy losses from numerous diverse and unstructured dissipative sources. By setting up a Sturm-Liouville equation, we are able to incorporate within our formalism the conservation of the total time-averaged energy flux in the presence of background winds, thereby verifying the Eliassen and Palm First Theorem. Such a formalism would allow us to parametrize all dissipative losses (turbulence, viscosity, heat conduction etc) by adding an absorptive parameter (the optical potential) which, owing to the very short vertical range (of the order of one or two kilometers or less) would allow us to ignore the detailed structure of the loss mechanism in the same way that the short range of the nuclear potential would allow us to use a two-parameter single optical potential for the enormous number of excitation and ionization processes (including multi-particle production) in nuclear scattering. The magnitude of the absorption is, however, sufficiently large, so that the reflection at the critical level does not play any role. Since, unlike nuclear physics, the range over which the instability occurs can be calculated (Geller et al (1975)), we are left with a single parameter model.

In this formalism the optical potential takes care of losses other than the loss into the mean flow. Our particular method also allows us to generalize the result for vertical pressure energy flux to include the absorptive losses ((15) and (16)). The total downward reflection of a gravity wave from the critical layer region depends on the horizontal phase velocity v_h of the gravity wave, the vertical wind gradient, as well as the background atmosphere. For stable background winds ($\lambda > 1/4$) and realistic losses ($|W_0| = 0.45\lambda \approx 0.65\lambda$) and for climatological wind gradients, the downward reflection coefficient ranges from 5% to 25% which is not sufficient for gravity-wave ducting.

We have also found that for realistic losses in the range $|W_0| = 0.45\lambda \approx 0.65\lambda$ and for stable background winds, the downward reflection is independent of the physics in the neighborhood of the critical level. The very large viscosity and heat conduction losses expected near the critical level, in fact, do not play any role; the incident upgoing wave being so reduced in amplitude at such close proximity to the critical level that the reflected wave, so close to the critical level, is negligible, even if the total reflection from the entire critical-layer region (as opposed to the critical level) can be quite significant.

The total reflection coefficient drops down to very low values periodically as a result of resonance absorptions. The resonance absorptions depend, of course, on the background winds and horizontal phase velocity of the gravity wave as expected. The

background atmosphere also plays a significant role in determining where the resonance absorptions occur.

For unstable background winds, our optical model shows that over-reflection could occur, in agreement with Jones (1968). The unstable background situation ($\lambda < 1/4$) has been shown to be equivalent to stable background situation ($\lambda > 1/4$) with a source for producing waves instead of a sink for absorbing waves. In this way, our method can bring the physics of stable and unstable background winds to within the same framework.

Our original reason for making this investigation is through the recognition of the very short vertical distance over which the incident gravity wave is absorbed or dissipated compared to its much longer incident vertical wavelength. This suddenness in the absorption would suggest a breakdown of the WKB approximation resulting in a considerably greater reflection than is generally thought. We were particularly surprised to find that the absorbing negative optical "potential" for a stable background becomes in effect an emitting positive "potential" with an unstable background, thus, bringing both phenomena to within a single mathematical framework.

With climatological wind profiles we have found that there is relatively little reflection, never much higher than 25%. But using the actual observed profiles of Tao and Gardner (1994) we have found a reflection of the order of 60% or greater for a reasonably

large range of horizontal phase speeds, due mostly to the very large observed wind gradient. This would seem to indicate that on the whole there is considerable more reflection from the critical layer than is usually thought. Furthermore, the two competing effects, i.e. the decrease in reflection due to dissipation and the increase in reflection due to the suddenness of the switching on of the dissipation, result in Figure 8 in which the reflection coefficient first drops to a minimum (at 35 to 40 m/sec) and then increases. Variations in the single parameter, W_0 , in our single-parameter model do not seem to be able to bring down the magnitude of the reflection coefficient.

Lastly, we have in the process obtained G.W. solutions as the critical layer is approached. These can be used to calculate the response of airglow to gravity waves in the presence of critical layers as typical small scale gravity waves often do encounter such layers with the height range for OH, OI or other types of airglow emissions.

Bibliography

1. J. R. Booker, F. P. Bretherton, The Critical Layer for Internal Gravity Waves in a Shear Flow, J. Fluid Mech. 27. 513 (1967).
2. P. Hazel, The Effect of Viscosity and Heat Conduction on Internal Gravity Waves at a Critical Level, J. Fluid Mech. 30, 775 (1967).

3. W. L. Jones, Reflection and Stability of Waves in Stably Stratified Fluids with Shear Flow; a Numerical Study, J. Fluid Mech. **34**, 609 (1968).
- 4 J. E. Geisler, R. E. Dickinson, Numerical Study of an Interacting Rossby Wave and Barotropic Zonal Flow near a Critical Level, J. Atmos. Sci. **31**, 946 (1975).
5. M. A. Geller, H. Tanaka, D. C. Fritts, Production of Turbulence in the Vicinity of Critical Levels for Internal Gravity Waves, J. Atmos. Sci. **32**, 2125, (1975).
6. L. I. Schiff, Quantum mechanics, 3rd edition, McGraw-Hill, (1968).
7. A.D. Richmond, The Nature of Gravity-Wave Ducting in the Thermosphere, J. Geophys. Res. **83**, 4143 (1978).
8. NCAR CEDAR Data base Catalogue (1990), National center for Atmospheric Research, Boulder, Colorado.
9. J. M. Forbes, D. F. Gillette, AFGL-TR-82-0173(I), AFGL (now Phillips Lab.) Hanscom AFB(1982), ADA 125720..
10. M. J. Taylor, E. H. Ryan, T. F. Tuan, R. Edwards, Evidence of Preferential Directions for Gravity Wave Propagation due to

Wind Filtering in the Middle Atmosphere, J. Geophys Res. **98**, 6047 (1993).

11. E. H. Ryan, "Critical Layer Directional Filtering of Atmospheric Gravity Waves", MS. Thesis, University of Cincinnati, (1991)
12. D. Y. Wang, T. F. Tuan, Brunt-Doppler Ducting of Small-Period Gravity Waves, J. Geophys. Res. **93**, 9916 (1988)
13. X. Tao, C. S. Gardner, Momentum and Heat Flux Observations in the Mesosphere above Haleakala during ALOHA-93 G.R.L. ALOHA/ANLC- 93, special edition, (1994)
14. G. R. Swenson, M. J. Taylor and P. J. Espy, ALOHA-93 Measurements of Intrinsic AGW Characteristics using the Airborne Airglow Imager and Groundbased Na Wind/Temperature Lidar G.R.L, ALOHA/ANLC-93, (1994).

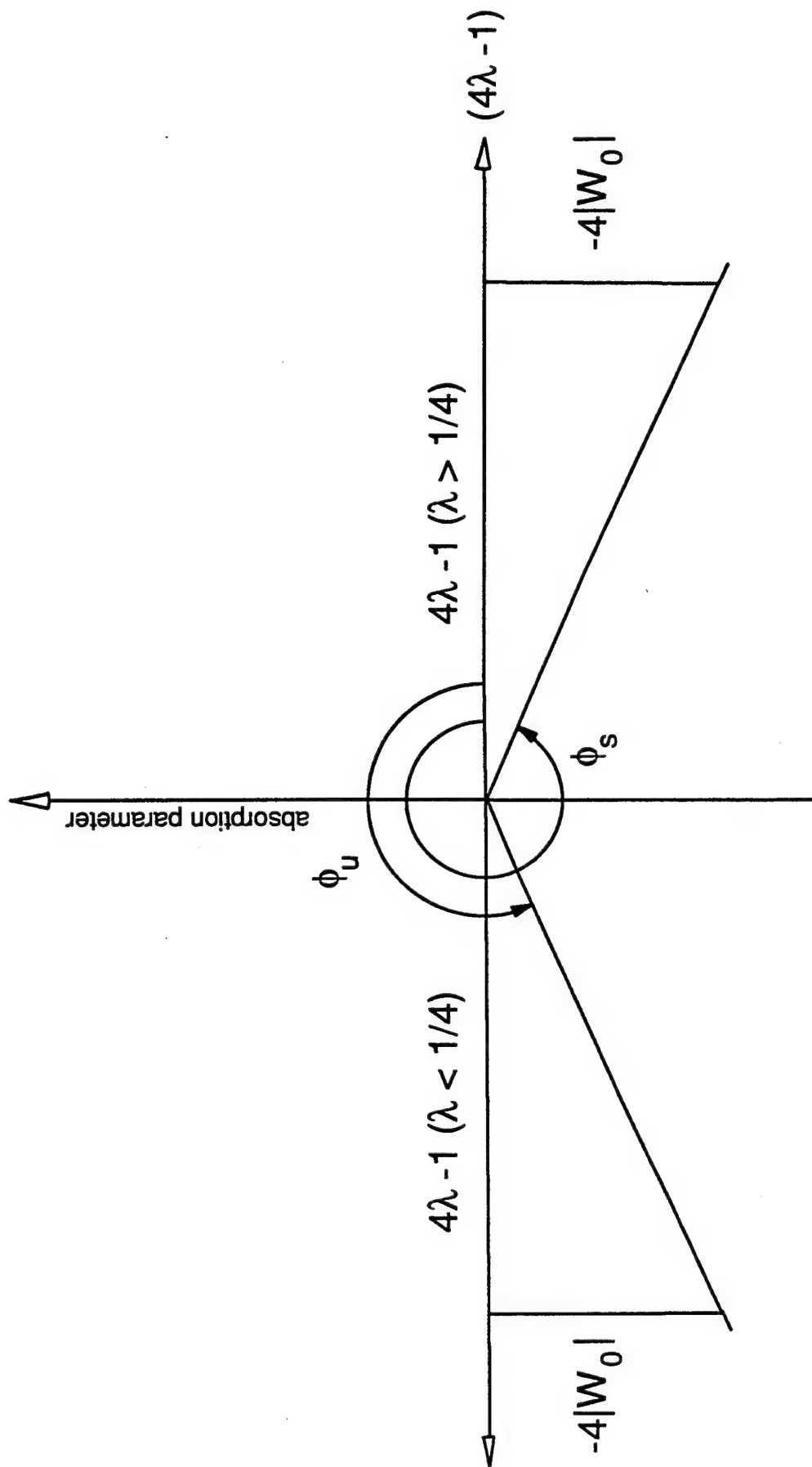


FIGURE 1

horizontal wind profile

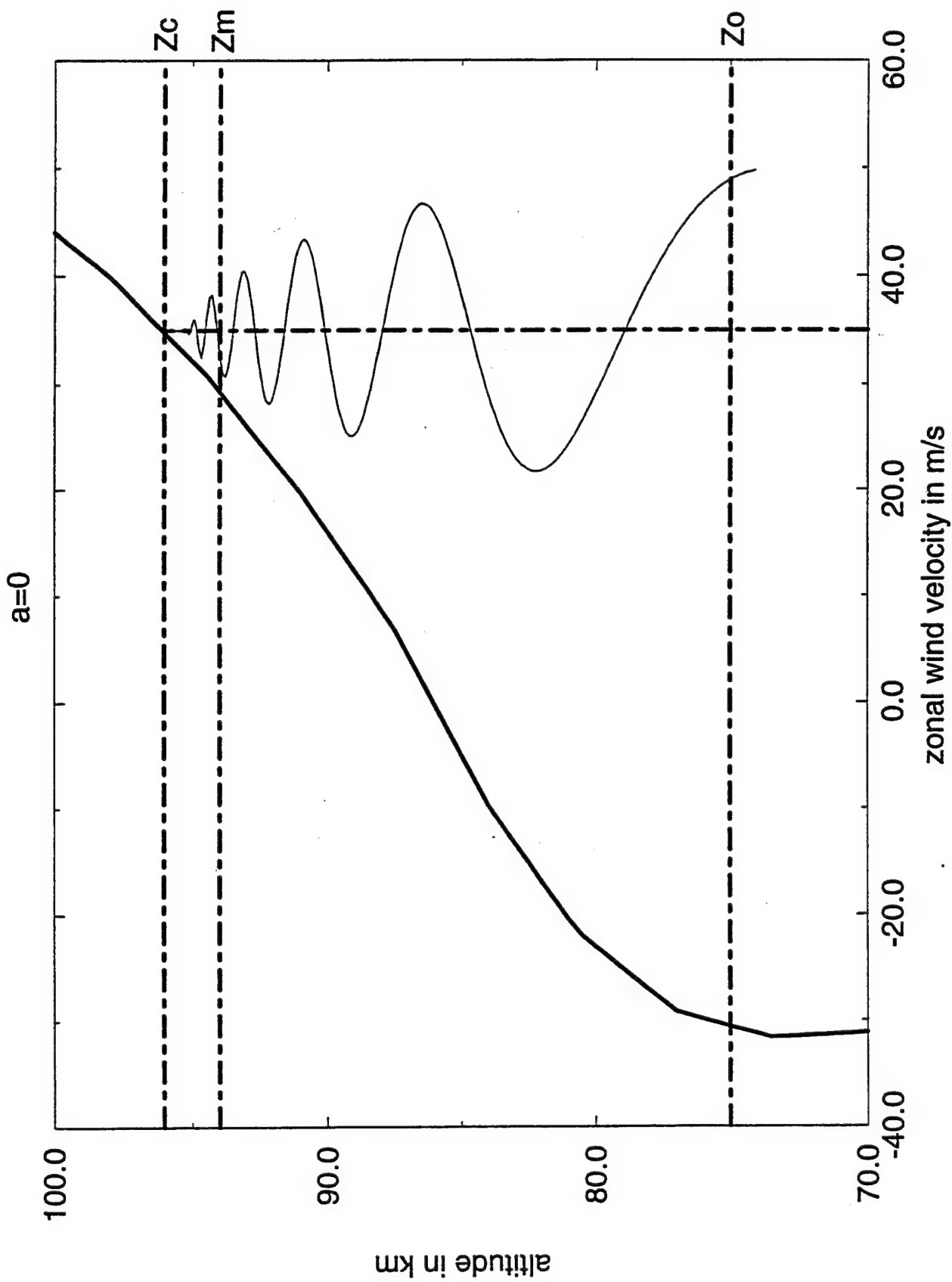


FIGURE 2a

horizontal wind profile

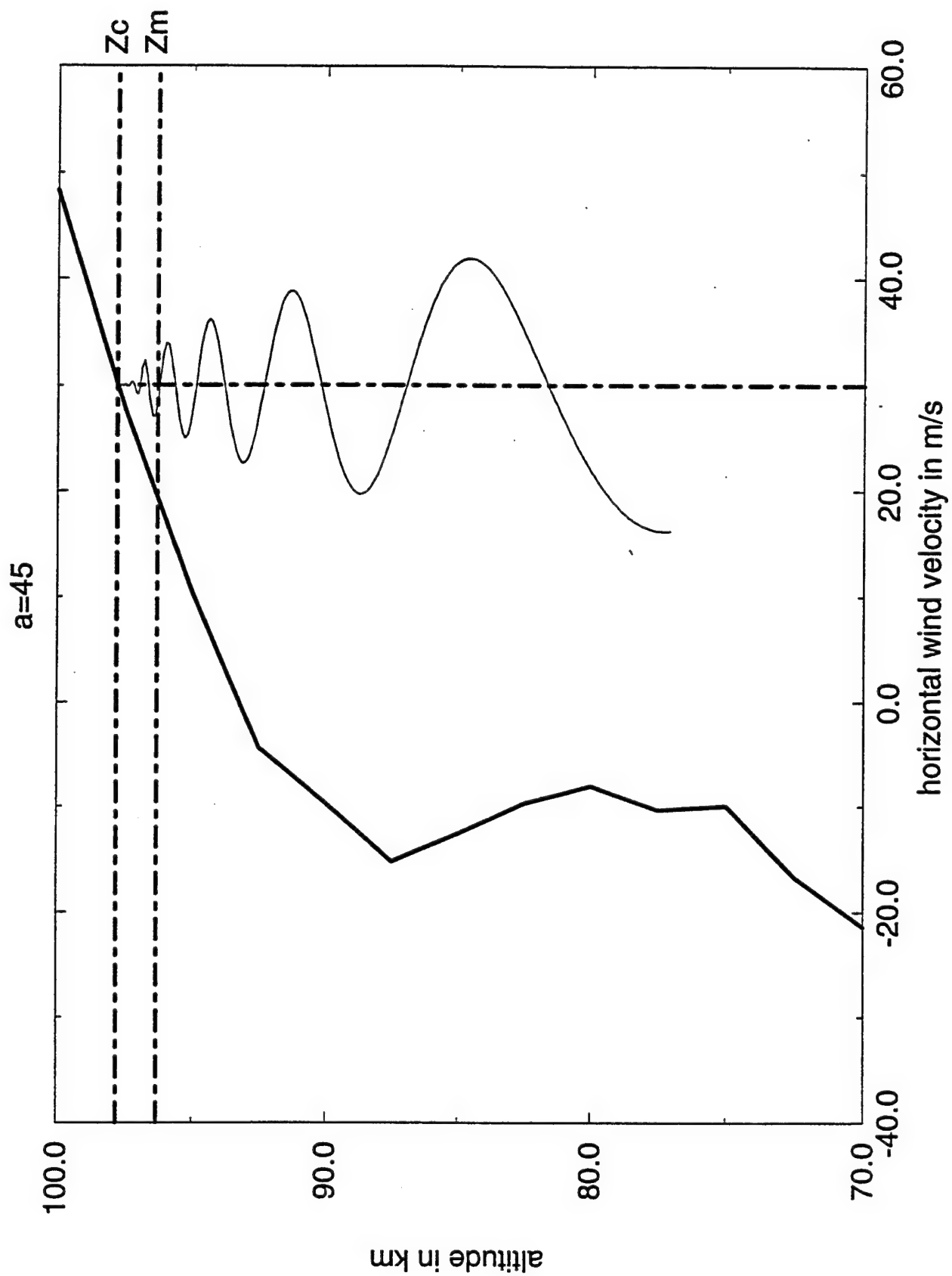


FIGURE 2b

horizontal wind profile

a=315

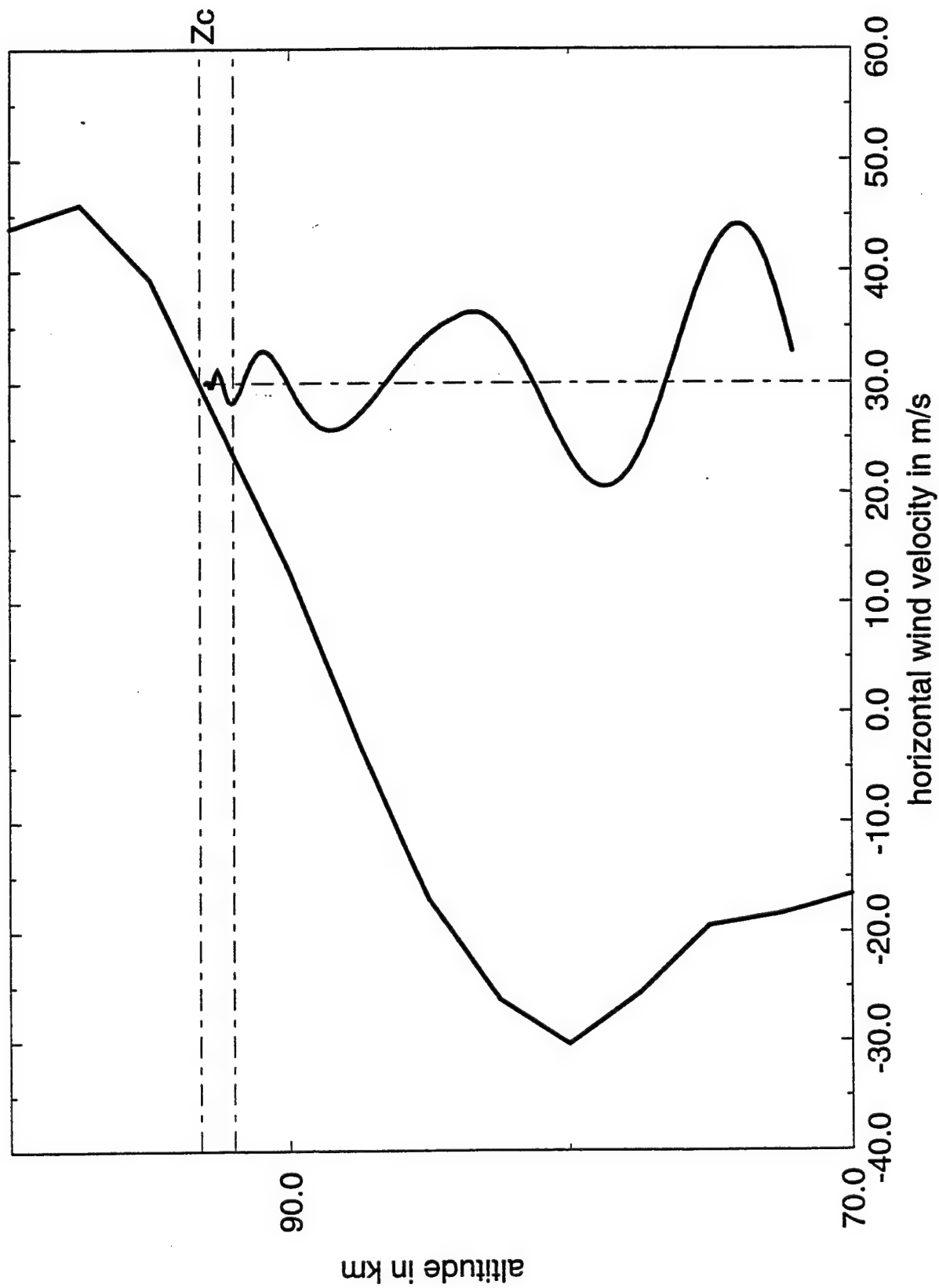


FIGURE 2c

Reflection Coefficient vs Horizontal Phase Velocity

$T = 30\text{min}$, $a = 0$, $Wo = -0.15$

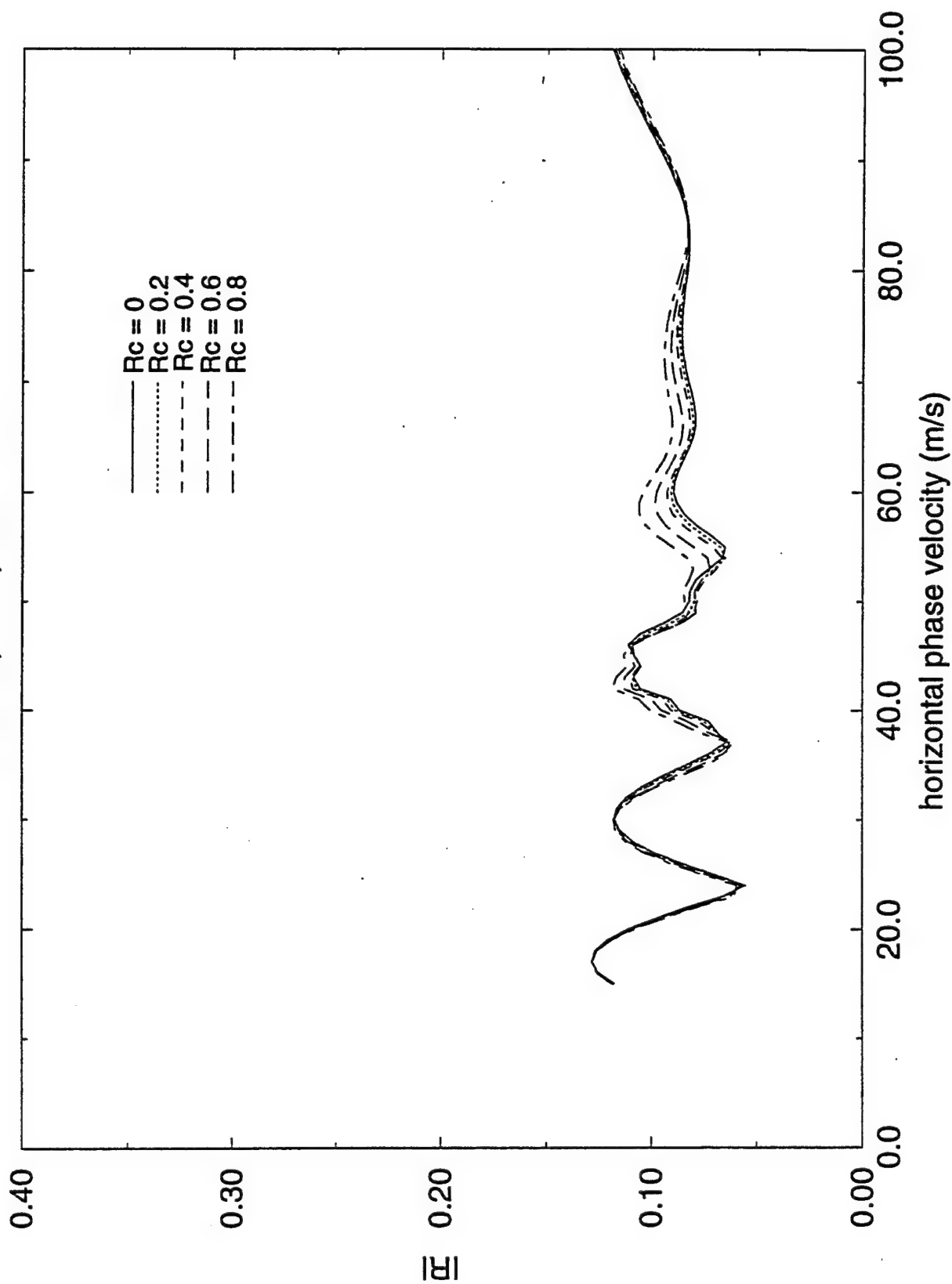


FIGURE 3a

Reflection Coefficient vs Horizontal Phase Velocity

$T = 30\text{min}$, $a = 45$, $Wo = -0.15$

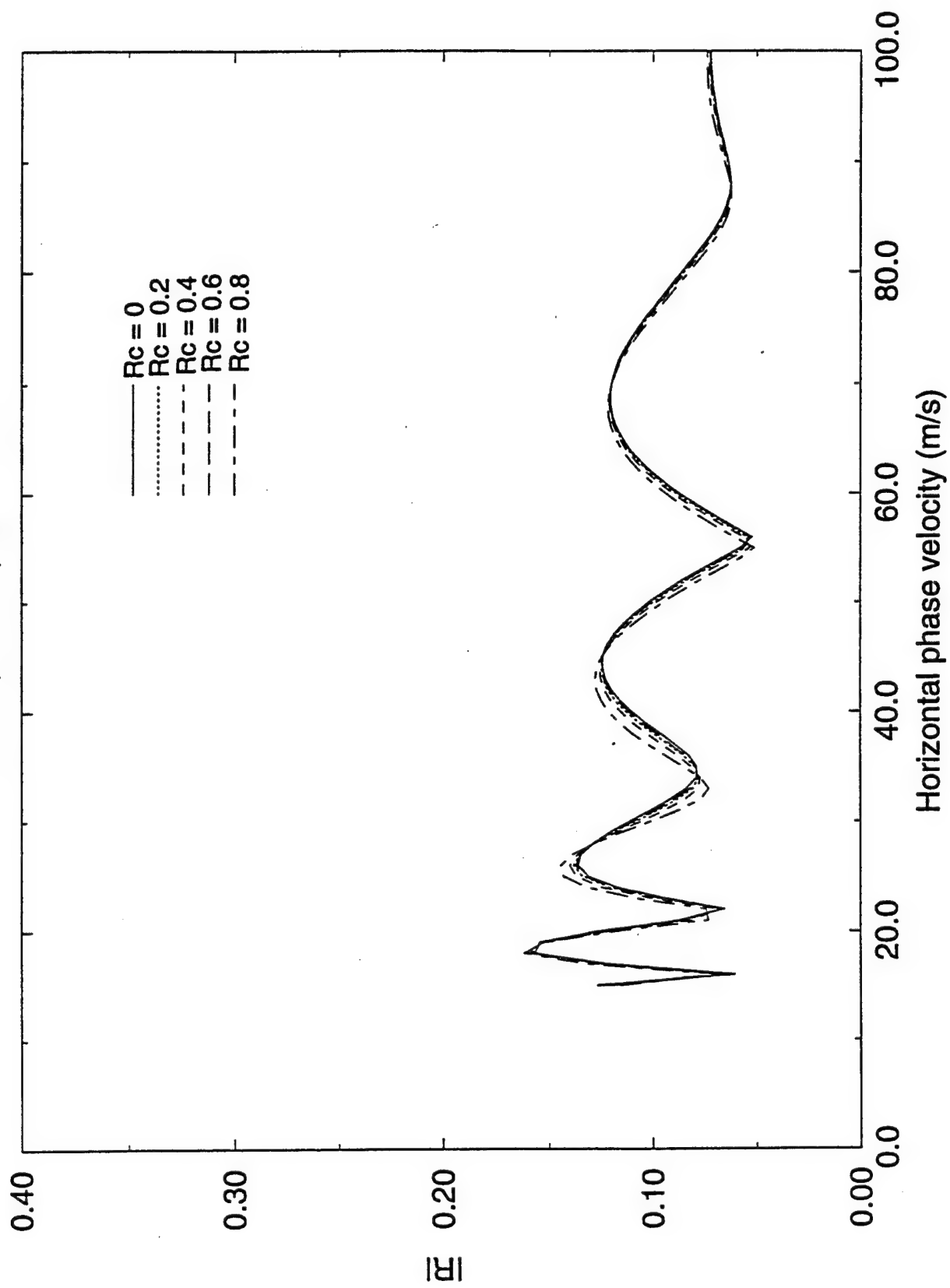


FIGURE 3b

Reflection Coefficient vs Horizontal Phase Velocity

$T = 315$, $a = 315$, $Wo = -0.15$

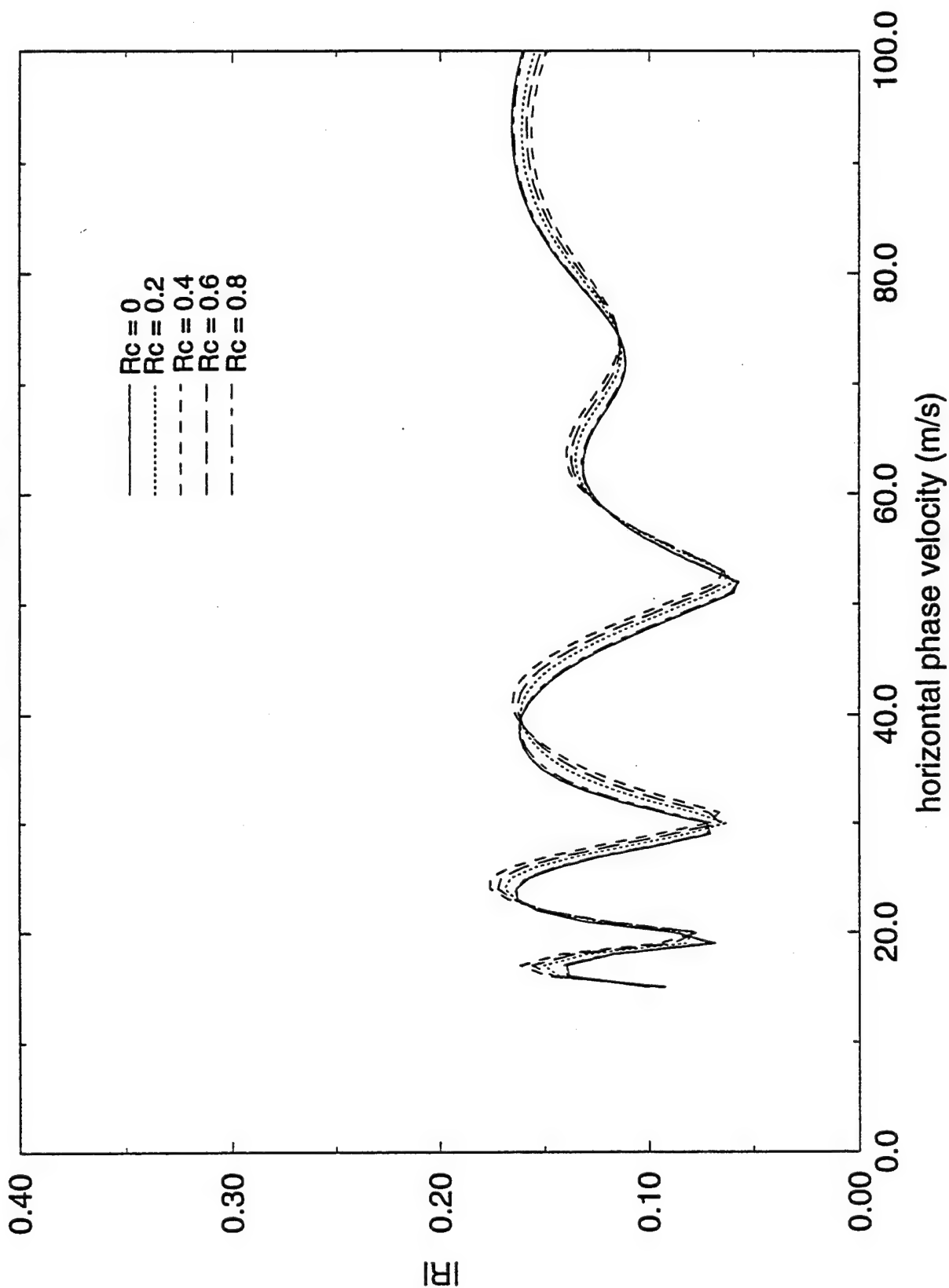


FIGURE 3c

Reflection Coefficient VS Horizontal Phase Velocity

$T=30\text{min}, a=0$

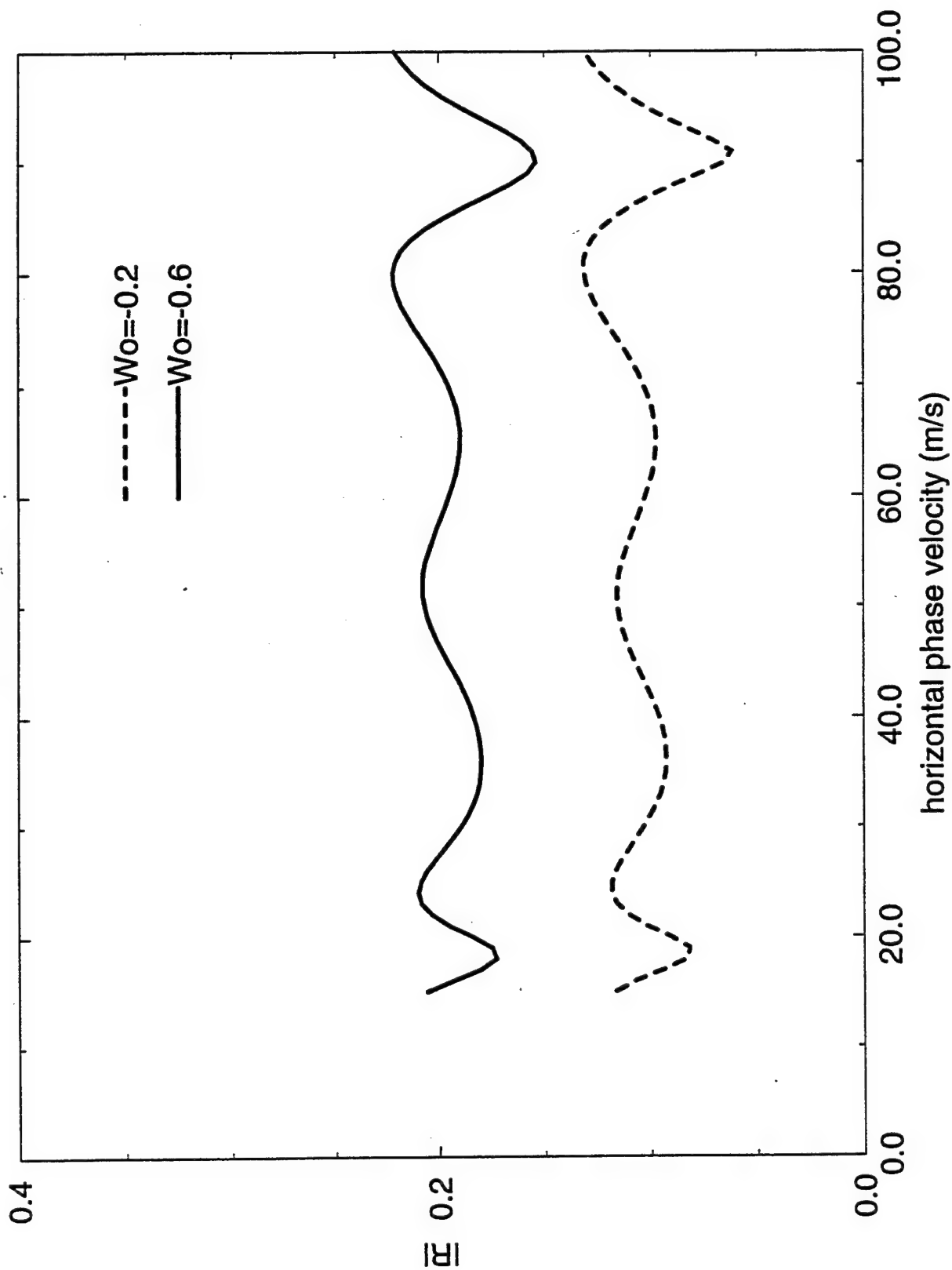


FIGURE 4a

Reflection Coefficient VS Horizontal Phase Velocity

$T=30\text{min}$, $a=45$

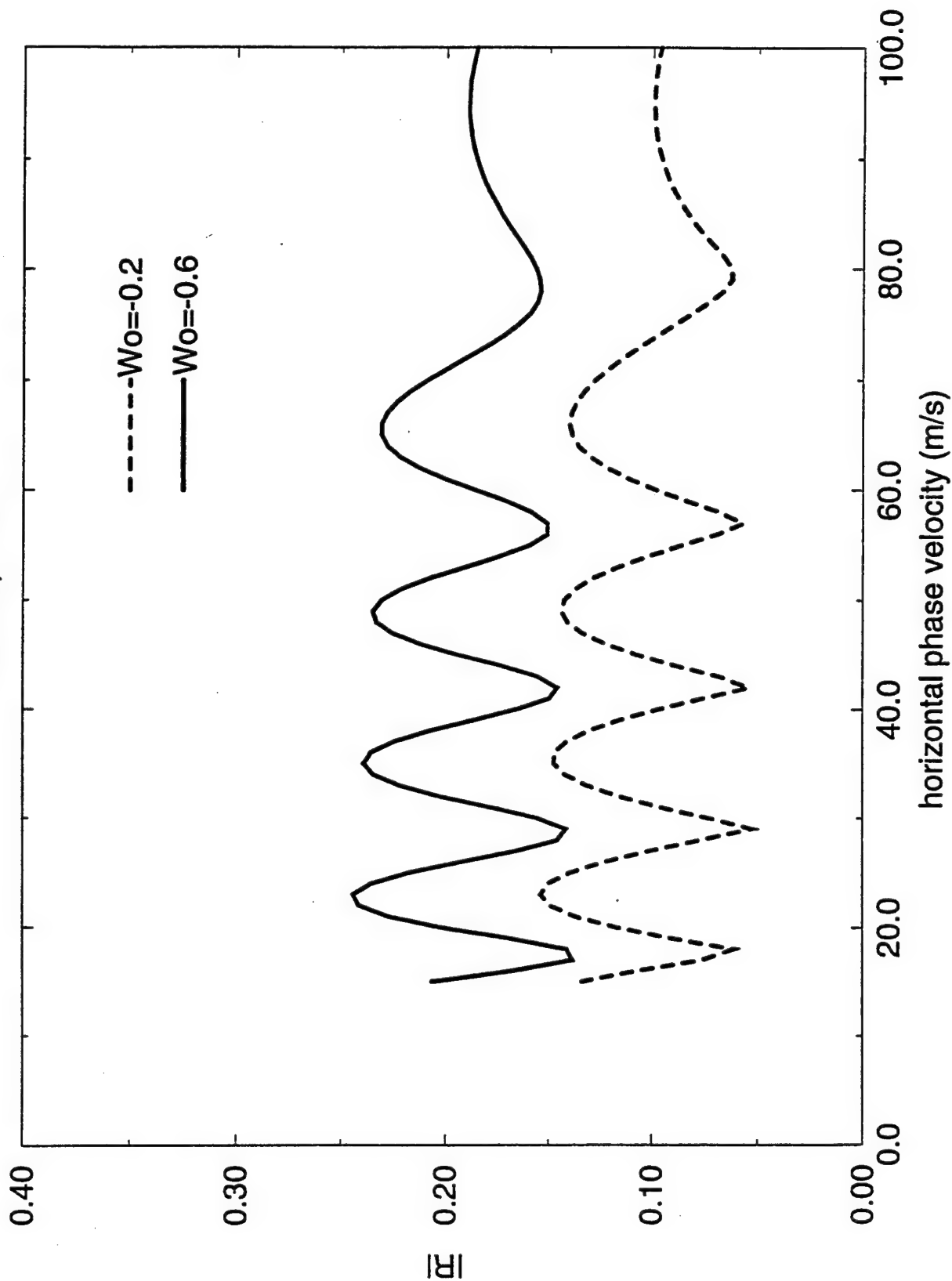


FIGURE 4b

reflection Coefficient VS Horizontal Phase Velocity

T=30min, a=315

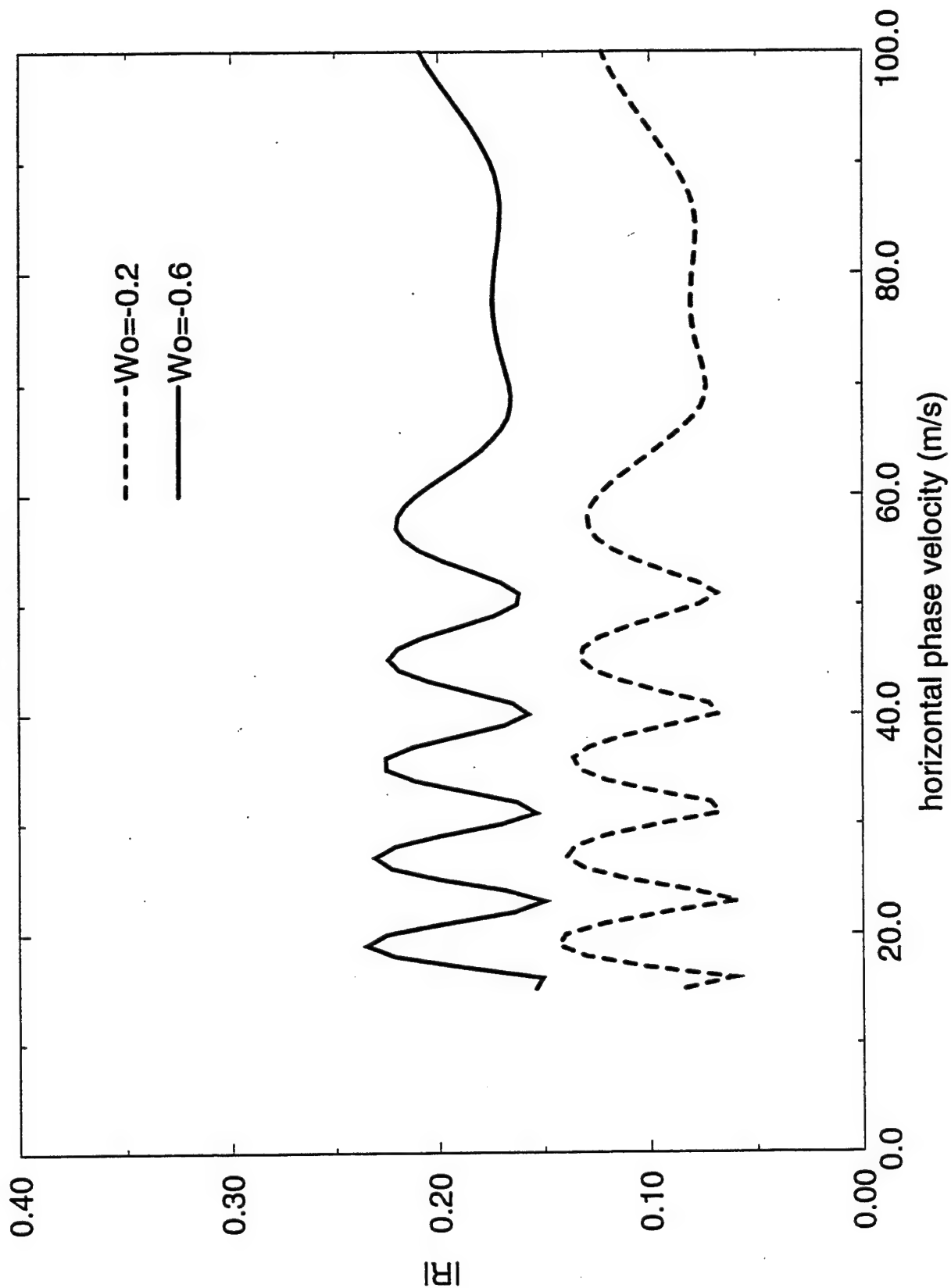


FIGURE 4c

Altitude vs Brunt Frequency

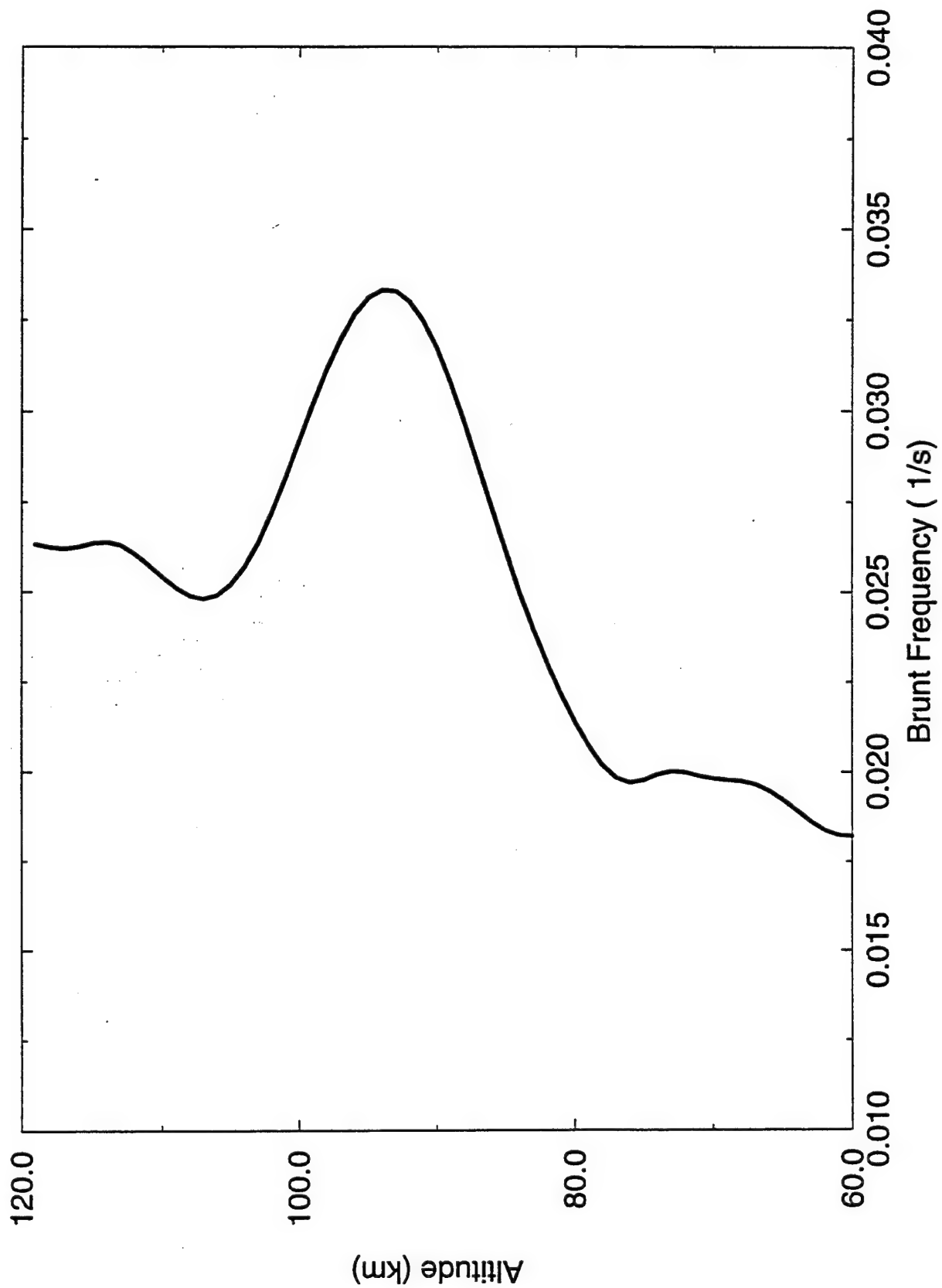


FIGURE 5

Reflection Coefficient vs Lambda

$T=30\text{min}$, $V_x=30\text{m/s}$, $a=0$

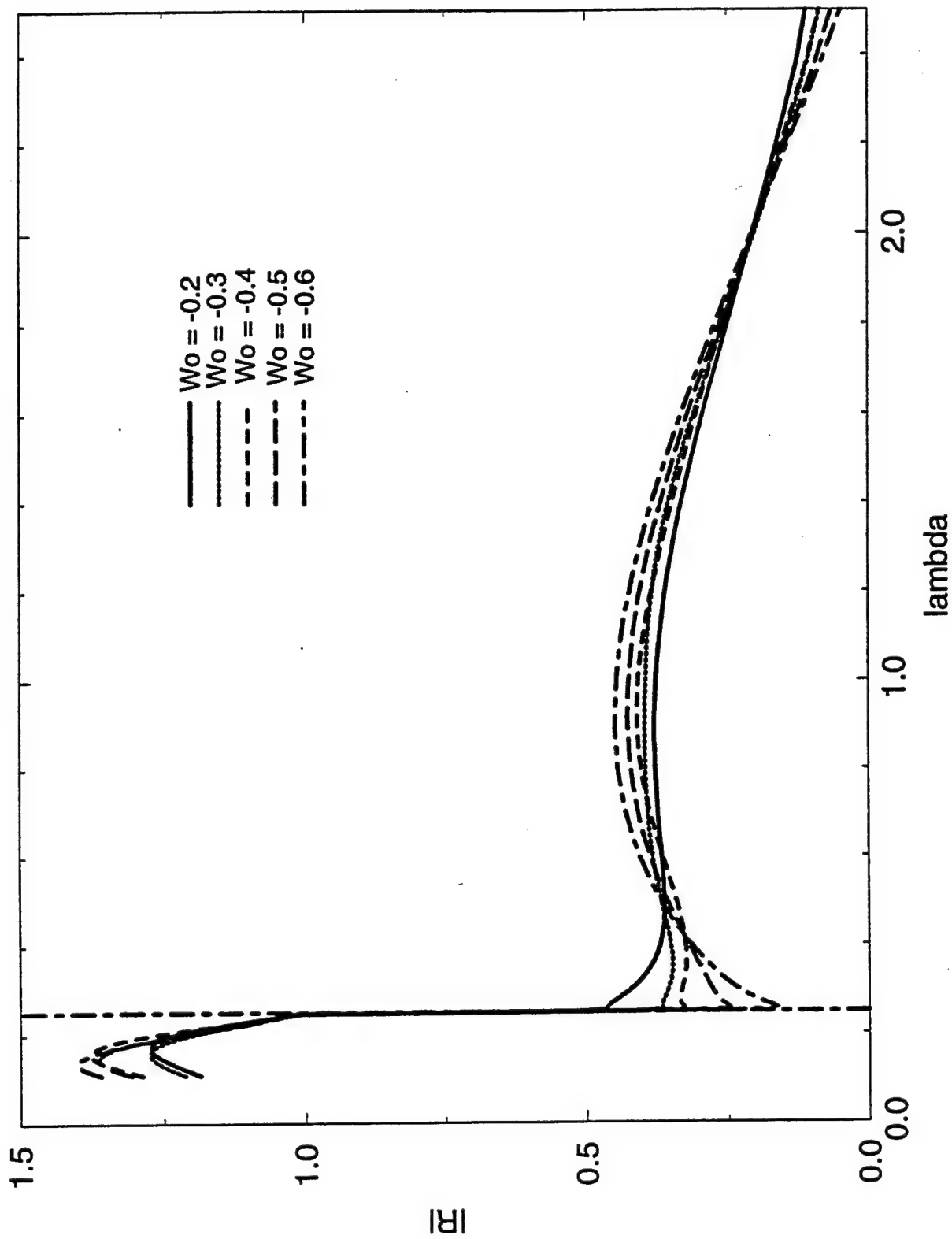


FIGURE 6a

Reflection Coefficient vs Lambda

$T=30\text{min}$, $V_x=30\text{m/s}$, $a=45$

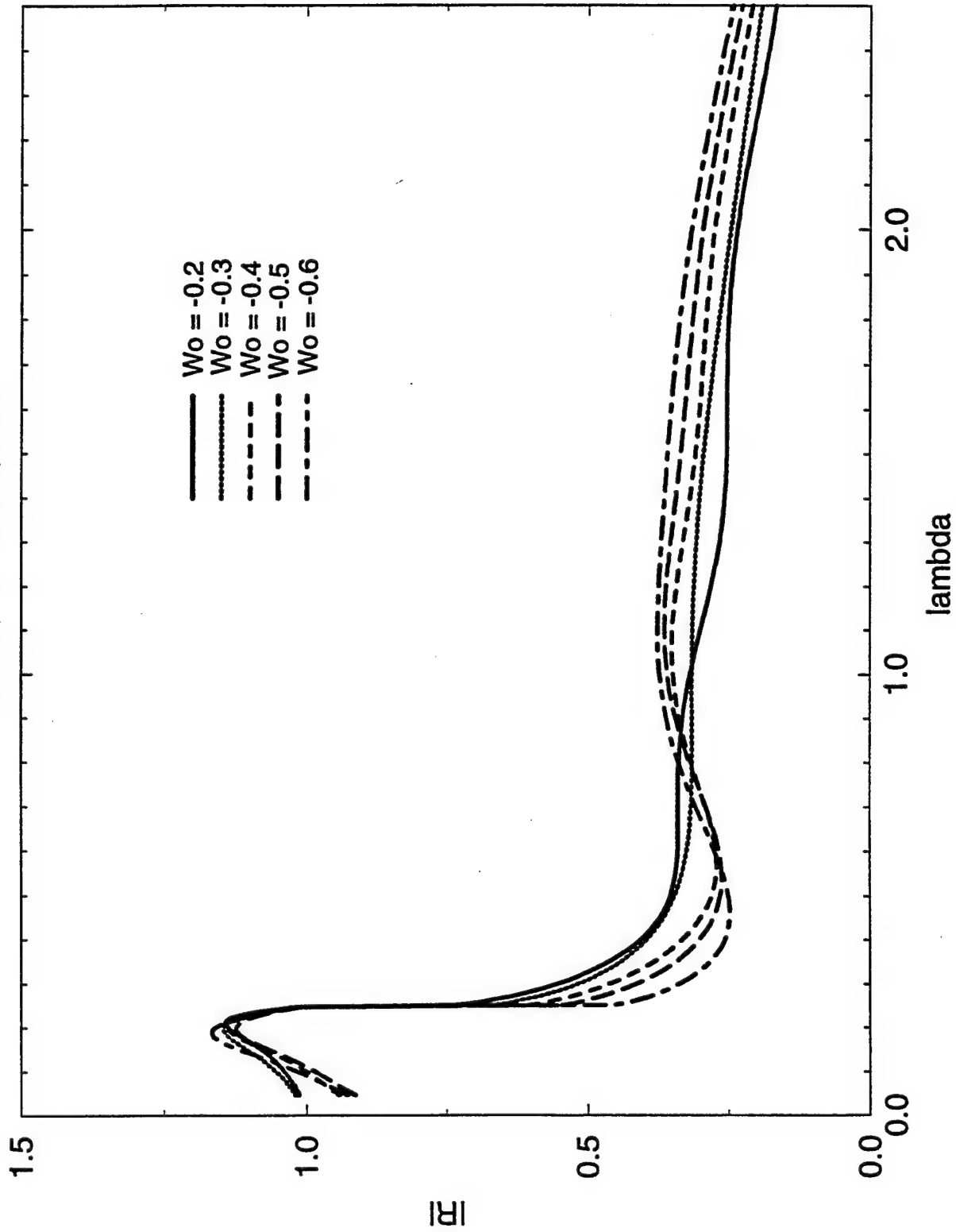


FIGURE 6b

Reflection Coefficient vs Lambda

$T=30\text{min}$, $V_x=30\text{m/s}$, $a=315$

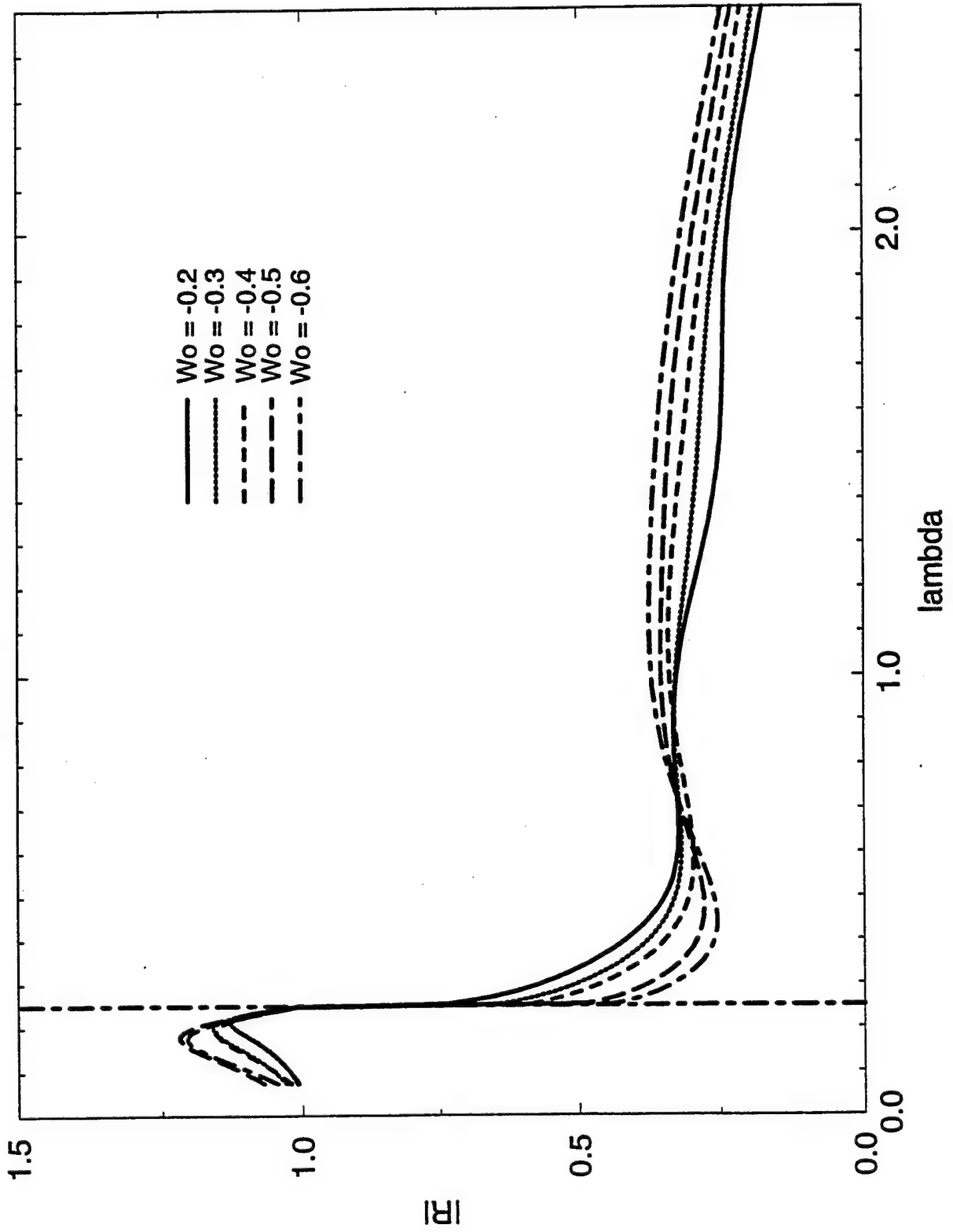


FIGURE 6c

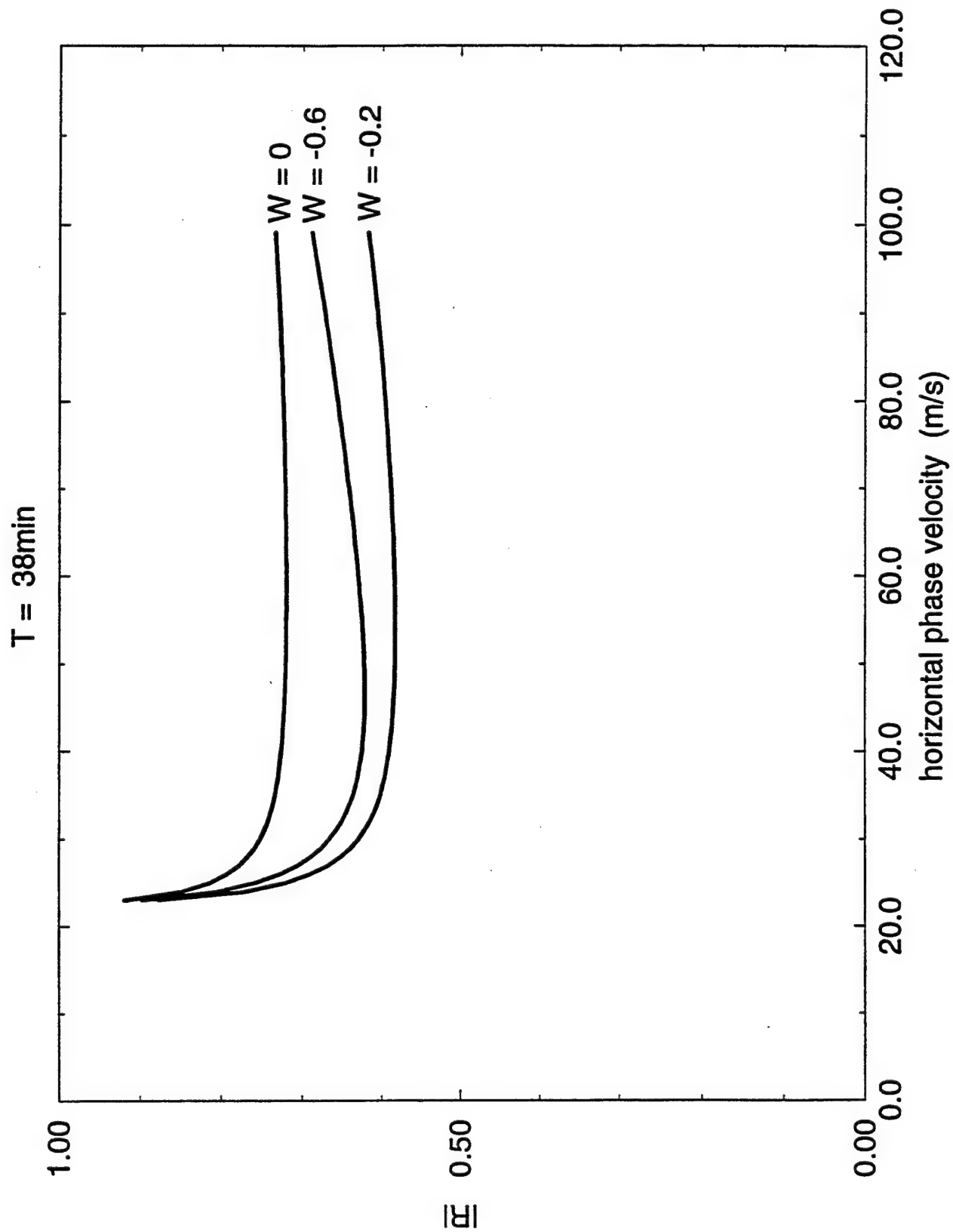


FIGURE 7

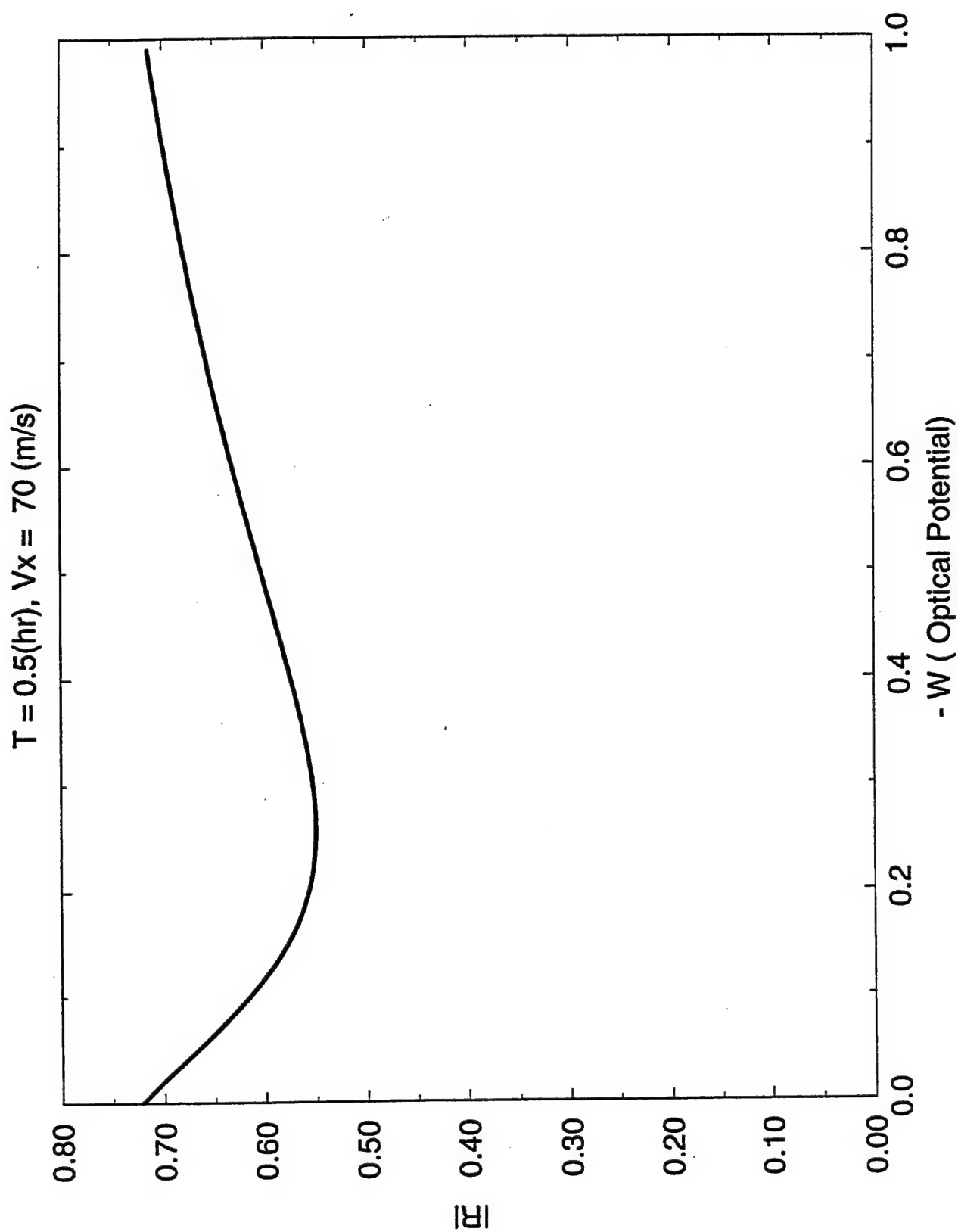


FIGURE 8

5 APPLICATION OF THE DISPERSION FORMULA TO LONG AND SHORT PERIOD G.W. MODES; THEIR TRANSFORMATIONS AMONG DIFFERENT TYPES OF GUIDANCE MECHANISMS WITH CHANGING PERIODS, AND COMPARISONS WITH ALOHA DATA

Introduction

Recent OH and 557.7 OI observations in the ALOHA campaign have revealed wave structures which cover a large part of the sky and appear to be guided within a narrow height range. Much of the observed wave structures have periods in the range of 10 min. or less. The possibility of short-period fully guided rather than partially guided wave modes in the mesospheric region can be easily understood by simply looking at a plot of Brunt period curve vs height (Wang & Tuan, (1988)). The mesospheric trough in the Brunt-period curve can readily provide full wave ducting since the wave can only be evanescent above the trough and has nowhere to "tunnel out" below. This is not true, however, for long-period ducted modes which, without the Brunt period limitation at the upper boundary, are for the most part partially (Tuan and Tadic, (1982)) guided since they can leak out through an essentially isothermal upper half space. In the present report we are primarily concerned with the basic physics of long-period and short-period ducting; their transformation from partial, to virtual, to full-wave guidance as the period is shortened. We will also consider the application of some of the short-period modes (in particular, a two-node fully guided mode) to some spectacular observed ALOHA data just mentioned above. We shall first, however, consider the fundamental problems of treating ducted modes.

From the beginning, it was recognized that fully guided modes would not present a serious problem, since such modes are sharply divided from each other and modal "interference" does not occur. However, interest at that time centered around long period waves (waves with periods many times greater than the Brunt period), and for such periods fully guided modes are rare. Early theoretical studies of partially guided long-period G.W. modes can be divided into two schools: one school (Friedman (1966), Midgley and Liemohn (1966), Reddy (1969)) applies to the G.W. solutions a radiation boundary condition for the upper atmosphere above an artificially set upper boundary (to allow the wave energy to freely escape) together with a rigid surface boundary condition at the ground level;

the solutions satisfying these upper and lower boundary conditions are then found with the help of the multi-layer model which allows us to treat an inhomogeneous background atmosphere. Since the solutions satisfying the radiation and the rigid surface ground boundary conditions cannot simultaneously satisfy flux conservation within a time independent framework, the wave vectors of the guided mode solutions are in general complex.

The second school (Francis (1973), (1975), Yu et al (1980)) considers the behavior of the reflection coefficient at the same upper boundary when a G.W. from above the upper boundary is reflected by all the atmospheric structure as well as the rigid ground surface below the boundary. Then, from standard phase-shift analysis, partial wave guidance can occur whenever the phase of the reflection coefficient changes by π over a very narrow range in the horizontal phase velocity. Unlike the first school, this method conserves flux since only the rigid surface ground boundary condition is used and the vertical wave vector is hence allowed to remain real. The first school obtains solutions with complex vertical wave vectors because of the very nature of their boundary conditions; the method would almost invariably lead to an infinite number of partially guided modes. The second school deals with real vertical wave vectors all the time and finds only two partially guided modes at lower altitudes; altitudes where the presence of additional partial wave guidance from the dissipation mechanism (Richmond (1978)) does not enter the picture. In this report we deal only with structural guidance and will therefore set the upper boundary low enough to avoid any other guidance mechanisms such as, for instance, the dissipative guidance (Richmond (1978)).

To connect these two seemingly irreconcilable methods, Tuan and Tadic (1982) have shown that a dispersion formula linking the reflection coefficient (used by the second school) for the G.W. above the upper boundary in the thermospheric region, where the atmosphere can be assumed to be uniform and isothermal, to all the free and guided modes (as computed by the first school) that occur below this boundary (this would include all wave guidance of interest to us), can be developed. They have proved that the guided modes computed by the first school appear as complex poles in the reflection coefficient. For an overall picture of the reflection of the G.W. by both the atmospheric structure and the rigid ground boundary, we refer you to Fig.1 in the paper by Tuan and Tadic (1982). The dispersion formula for this reflection coefficient is

derived entirely from imposing causality on the Sturm-Liouville form of the inviscid hydrodynamic equation and is valid for any background atmospheric model.

In this paper we will begin with long-period waves by comparing the phase shift for the reflection coefficient computed from straight partial-wave analysis used by the second school, to the phase shift computed from the reflection coefficient given by the dispersion formula which provides the explicit linkage to the modes computed by the first school. As will be seen, they are essentially the same, proving once and for all that only two long period partially guided modes can exist. We then show that, using only the dispersion formula, the phase shift computed from the 10-pole approximation is nearly the same as the 2-pole approximation and that these two poles are the Lamb and the S_2 modes. The other poles merely provide some background for the reflection coefficient.

We next consider what happens to the ducting mechanism when the wave period is gradually reduced. We shall only be concerned with the two prominent partially-ducted modes. As the period is reduced they move first away from the real axis and then to the negative imaginary axis where they become virtually guided modes. As the period is further reduced they move up the imaginary axis until they become two fully guided modes with purely imaginary vertical wave vectors. One interesting point is that the S_2 mode, which is less severely guided as a long-period partial mode than the Lamb mode, becomes ultimately the more severely fully guided mode at the short-period end. In addition, we find that many of the other "modes" as computed by the first school and which do not play a significant role in long-period partial wave guidance, can now become important fully guided modes. As a result, the total number of fully guided modes keep increasing as the period is shortened until about 6 min. when they again decrease as the Brunt period is approached. At 4.6 min. there are only 4 fully guided modes and ultimately at 3.6 min, when we are well below the Brunt period, there is only the Lamb mode, an expected result since the Lamb is not an internal mode but is guided mostly by the ground surface.

We then consider the dispersion curves for the one-node, two-node, three-node modes, their behavior as the Brunt period is approached, as well as their pressure variation solutions as a function of height for 10 min, 6 min and 4.6 min periods.

Finally, we consider the application of some of our result to the ALOHA campaign of 1993 in which many short-period wave structures at mesospheric height levels have been observed.

Formulation

The dispersion formula linking the "guided modes" computed by the first school to the reflection coefficient used by the second school is given by:

$$R(\omega, k)e^{2ika} = E(k) + \sum_{n=0}^{\infty} \left(\frac{k}{k_n} \right)^4 \frac{\lambda_n}{k - k_n} = R_a(k)$$

$$R(k) = \text{reflection coefficient}$$

$$a = \text{height of the upper boundary} \quad (1)$$

$$E(k) = R_a(0) + k\dot{R}_a(0) + \frac{k^2}{2!}\ddot{R}_a(0) + \frac{k^3}{3!}\ddot{\ddot{R}}_a(0)$$

$$\lambda_n = \text{Res } R_a(k_n)$$

where k is the vertical wave vector above the upper boundary. The set $\{k_n\}$ are the complex wave vectors computed by the methods of the first school and to which they correspond on a one to one basis. For the special case when they are purely imaginary they correspond either to the fully guided modes (positive imaginary), or virtually guided modes (negative imaginary). Thus, the modes computed by the first school become simple first order poles in the reflection coefficient. We should point out that, other than on the imaginary axis, the poles can only occur in the lower-half complex plane because one can show that a complex pole with a positive imaginary part would violate flux conservation (the analytic properties of R has been discussed in Tuan and Tadic (1982)). We should also point out that the set $\{k_n\}$ would be slightly different if a different atmospheric table were used.

Each of the complex poles (with negative imaginary parts) would have respectively corresponded to a partially guided mode if it were far enough away from neighbouring poles, and/or very close to the real axis. If, on the other hand, the poles are closer to each other than they are to the real axis, then from (1) they would interfere with each other to destroy the guidance mechanism and what remains would merely form a general background to the reflection coefficient. The method used by the first school without

the benefit of the dispersion formula would therefore always greatly exaggerate the number of partially guided modes. In practice, only the two poles closest to the real axis correspond to real partially guided modes, i.e. the Lamb and the S_2 modes. The λ_n are the residues which provide the relative "weights" to the poles. Again, only two values of λ_n are very large and, again, they correspond to the Lamb mode and the S_2 modes. For fully guided modes, on the other hand, there is no interference and the method would work, since, instead of the radiation condition, we would then have an exponentially decaying upper boundary condition (corresponding to poles on the positive imaginary axis) and the vertical wave flux is conserved (it is zero everywhere; the exponential and the rigid surface ground boundary conditions produce a vertically stationary wave).

Our purpose is to use (1) to compute the reflection coefficient and hence also the phase shift and then compare the latter with the phase shift computed by the usual phase shift analysis using the methods of Francis (1973) and Yu et al (1980) from the second school. If the phase shift computed by these two totally different methods agree, then we would have established the connection between the set $\{k_n\}$ computed by the first school using the radiation boundary condition plus the rigid surface condition and the phase shift computed by the second school using only the rigid surface condition.

Fig. (1) shows the long-period poles in the complex k_x -plane instead of the k_n (see (1)) in the complex k_z -plane (the two are simply related by the Hines' dispersion relation for the uniform upper-half space). k_x is used here instead of k_z to facilitate comparisons with Reddy's work which used only the complex k_x -plane as well as a different atmospheric model. Other than the difference in atmospheric models, we used essentially the same technique that Reddy and others in the first school used for computing these poles. By long period we mean anything above 30 min. when the wave period is sufficiently long compared to the Brunt period that the pole locations would not change from a change in the wave period. Reddy (1969) was primarily concerned with only the long-period gravity modes and did not investigate what happens when the periods is lowered to the Brunt period range. The results for long periods show little difference in the important poles, i.e. the poles closest to the real axis where the real physics is.

The second school (Francis (1973), (1975) and Yu et al (1980), merely compute the reflection coefficient as a function of real k (as opposed to complex k required by the radiation condition). Whenever the phase of the reflection coefficient changes suddenly by π , we identify a resonance or partially guided mode. Equation (1) above establishes the connection between the two different schools. The reflection coefficient for real k is expressed in terms of both the complex and the purely imaginary poles, k_n . Whilst all this theory has been developed in the paper by Tuan and Tadic (1982), there has never been an explicit numerical verification of the theory based on realistic model atmospheres.

In this paper we use a COSPAR atmospheric model together with the multi-layer techniques developed by Reddy (1969) and others to compute the complex and imaginary poles. We then use an extension and generalization of a theory first developed by Hu (1948) which makes use of the symmetry properties of the reflection coefficient (in Hu's case, the Heisenberg S-matrix) to compute the residues, λ_n . The techniques used by Reddy and others (Friedman (1966), Midgley and Liemohn (1966) etc.) have been extensively described in the literature and will not be discussed here. We will need, however, to develop the technique and method for computing the residues.

We know that, in general,

$$R(k) = \frac{G(k)}{G(-k)} \xrightarrow{k \rightarrow k_n} \frac{\text{Res}R(k_n)}{k - k_n} \quad (2)$$

As $k \rightarrow k_n$, we expand $G(k)$ and $G(-k)$ about k_n . We know that $G(-k)$ has zeros at k_n and $-k_n^*$ (Tuan and Tadic (1982), Therefore,

$$G(-k) = (k - k_n)(k + k_n^*)\phi_n(-k) \quad \text{where } \phi_n(-k) = \text{analytic func. of } k. \quad (3)$$

Using (2) and (3) we obtain:

$$R(k) = \frac{(k + k_n)(k - k_n^*)\phi_n(k)}{(k - k_n)(k + k_n^*)\phi_n(-k)} \quad (k \text{ close to } k_n) \quad (4)$$

We may, of course, include more and more nearby poles, k_n , k_{n+1}, \dots, k_m where k_m can be quite far away so that $|k_m| \gg |k|$. Equation (4) then becomes:

$$R(k) = \frac{(k+k_n)(k-k_n^*)}{(k-k_n)(k+k_n^*)} \frac{(k+k_{n+1})(k-k_{n+1}^*)}{(k-k_{n+1})(k+k_{n+1}^*)} \dots \frac{(k+k_m)(k-k_m^*)}{(k-k_m)(k+k_m^*)} \frac{\phi_m(k)}{\phi_m(-k)} \quad (5)$$

Since k is close to k_n and k_m is very far away, the last fraction involving k_m is very close to one. Since ϕ_m contains zeros which are further away still from k , we may conclude that the ratio, $\phi_m(k)/\phi_m(-k)$, is also very close to one and may be approximated by unity. Re-writing (5) in terms of the residue, we obtain for k close to k_n :

$$R(k) = \frac{\bar{\lambda}(k_n)}{k-k_n} = \frac{\bar{\lambda}_n}{k-k_n} = \frac{\lambda_n e^{-2ik_n a}}{k-k_n} \quad (6)$$

Comparing (6) with (5) we have an expression for the residue, λ_n , at $k = k_n$. We have found that the two residues corresponding to the two poles most responsible for the S1 and S2 modes are at least a factor of 5 larger than the next largest residue among the ten poles we have examined.

From the basic definition of R_a , clearly $R_a(0) = 1$. The derivatives of R_a in the entire function in (1) can then be evaluated from (5) and (1). In this way we can compute all the parameters in the dispersion formula given by (1). From (1) we can then compute the phase shift for the reflection coefficient. We can also compute the scattering cross section, σ , from (1) where

$$\sigma \sim |1 - R|^2$$

The above equation provides the scattering cross section for a gravity wave initially propagating downwards from sufficiently high altitudes where we may approximate the atmosphere by an uniform isothermal half space. Owing to the rigid surface boundary condition at the ground level, there is no transmission, only reflection back into the half space. We may then write σ in terms of the phase shift

remembering that in the absence of transmission $|R|^2 = 1$. We may then write

$$R = e^{2i\delta} \quad (7)$$

where δ is the phase shift and is a function of the horizontal phase velocity (or k_x and through the dispersion relation, k_z , for fixed frequency). It is equal to half the phase angle defined by Francis (1973). The phase shift, according to this second school, is then given by:

$$k_z \cot[k_z a + \delta(v_x)] = \left. \frac{\psi'}{\psi} \right|_a \quad (8)$$

where ψ is the normalized pressure variation (below the upper boundary) and can be computed from equation (2) in Yu et al (1980). (8) can then be used to compute the phase shift. A plot of this phase shift as a function of horizontal phase velocity is given in Fig.5 of Yu et al (1980) which shows two relatively sudden changes by π units at phase velocities corresponding respectively to the Lamb and the S2 modes. The reflection coefficient at a , for any real values of k_x , or k_z at fixed ω , can be determined from (7). So much for the second school.

The same reflection coefficient can also be found from the dispersion formula given by (1) with the residues computed from (5) and (6) and the poles computed with methods similar to those used by the first school. Fig. 2 shows a comparison of the phase shift computed from the two entirely different schools. As can be seen, for both schools there are only two locations where the phase shift undergoes a relatively sudden change of π units. This Figure shows that by introducing the dispersion formula most of the guided modes obtained by the first school do not really constitute guided modes. In computing the phase shift using (1) and the poles computed by the first school, we have included ten poles. Figure 3 shows how little difference there is between using ten poles and just using the two most important poles for the Lamb and the S2 modes. The other poles just provide a background effect without any guiding effect,

although if each pole were there alone without any neighbours and if its residue is sufficiently large, it can be partially guided. The proximity to other poles with comparable residues effectively destroy the guidance mechanism.

Fig.4 shows the two peaks of the reflection cross section which reach a maximum at the Lamb and the S₂ modes where the phase shift undergoes a phase change by π . Fig. 5 shows the behavior of the phase shift as the period is decreased. The degree of the guidance, as measured by the steepness of the climb of the phase shift over π units, is also weakened. Fig. 6 shows the migration of the poles over similar decreases in period as in Fig. 5. The two important poles migrate away from the real axis while the distant poles migrate closer to the real axis. In this diagram, however, the scale is such that we cannot perceptibly see any such effect in the S₁ or Lamb mode (the negative imaginary part being exceedingly small) and only a very tiny just barely perceptible migration away from the real axis for the S₂ mode. We see also that at a period of 15 minutes the Lamb and the S₂ remain partially guided. The overwhelming dominance of the two important poles in the phase shift produces a net loss of wave guidance as the period is shortened.

Fig.7 shows the complete migration of the Lamb and S₂ modes as the period varies from long period (30 min or more) to the Brunt period range. The poles first migrate to the negative imaginary axis to become virtually guided modes and then up the imaginary axis to become fully guided modes. The interesting point here is that the S₂ mode (solid squares), a less severely partially guided mode than the Lamb mode at long periods, actually ultimately becomes a more deeply guided fully guided mode (i.e. its wave vector is more positive imaginary) at the Brunt period range.

In Table 1 we list the fully guided modes for 10 min., 6 min., 4.6 min., 4.2 min., and 4 min. waves. For all these fully guided modes the real part of the vertical wave vectors are extremely small. In the table 1 we indicate the modes by using the mode number. The phase velocity decreases when we increase the mode number. For 10 min. and 6 min. , 9 fully guided modes are listed. It should be noted that we can have a large number of fully guided modes with very small horizontal phase velocities. Present calculations did not consider the modes with very small horizontal phase velocities.

For the 4.6 min. period there are only 4 fully guided modes and one of which (the 70 m/sec wave) comes close to an observed 76 m/sec wave at the same period during the 1993 ALOHA campaign. Furthermore, the 70 m/sec wave has two-node mode, (Fig. 8). This means that the phase of the OH airglow oscillations should be 180° out of phase reversal between the observed OH and the green lines (Fig. 10, see also Taylor et al (1995)). This does not necessarily mean that we have correctly explained the observed phenomena since there are many other questions concerning the observed event on that night. But it does show that waves or instabilities with so small a period and two digit phase velocities do occur in nature and when they occur they must be fully guided.

When we shortened the period, the number of fully guided modes becomes less and for example at 4.2 min. we have only two fully guided modes, one of which is the Lamb mode. Finally, at 4 minutes there are no internally guided gravity modes, only the Lamb mode remains, as expected since the Lamb mode is primarily guided by the discontinuity at the ground surface. Interesting point here is that we do not have one-node mode for the period range 4.6 minutes to 13 minutes. for 4.7 minutes to around 4 minutes we have only the mesospheric duct in the Brunt period profile. Starting around 4.7 minutes there is a another mode (phase velocity is 282 m/sec) popping up. This mode is a one-node mode and the phase velocity of this mode decreases drastically as period further shortened.

We should point out that the labeling of the modes by the number of nodes make sense since the number of nodes for fully guided mode remains the same for each fully guided mode. But it should be point out here that if we have a substructures in Brunt period (or Brunt frequency) curve there might be a change of nodes for a given mode for different period. A partially ducted mode will always have an infinite number of nodes. The S_2 mode appears to be a two-node mode and the horizontal phase velocity goes from a high of about 250 m/sec at long periods to 38 m/sec at the short period end. this is the mode produced by reflections between the ground and the sharp temperature rise at the base of the thermosphere when the period is short.

Figure 9 shows the behavior of the S_2 mode at long and short periods. in the literature the short-period modes in general are labeled by different names from the long-period ones. In particular,

the S_2 mode is labeled as L_2 at the short-period end. Our analysis shows that since both refer to the same pole, perhaps the only unambiguous way to label the modes is through their individual migratory trajectories. One may argue, however, that since, as just mentioned, the ducting mechanism for the S_2 at the long period end is different from the short period end, the same mode represented by same pole ought to acquire different labels at different periods. For short periods (within the brunt period range), S_2 has 2-node structure and it is unchanged with periods. When we have the period 5.1 minutes, it can be seen that the S_2 mode wave function transfer from tropospheric duct to mesospheric duct. At 4.6 min. the wave function is entirely in the mesospheric duct.

Figure 10 shows the solution for normalized pressure variation for the two-node mode, three-node mode and four-node mode for periods 10 min., 6 min. and 5 min. For a given mode (i.e. given no. of nodes), the smaller the wave period the more severely guided the wave. The zero-node mode can only exist in a lone mesospheric duct, sufficiently far away from the ground to avoid the guidance effect from the ground. With a tropospheric duct, fairly close to the ground, the zero-node mode is difficult to form owing to the guidance effect of the ground. For the two-node mode (S_2 mode), one can clearly see that there is a transformation from tropospheric duct to mesospheric duct around 5.1 minutes. These transformation occurs when we have 'kissing' in the dispersion curves.

Fig. 11 shows the dispersion curves for the first 6 fully guided gravity wave modes. They all show a sharp drop to zero at a cut-off period which is the local brunt period at the bottom of the trough. For the period around 13.2 minutes, it seems that these fully guided modes vanish. For the range of 7-13 minutes, the phase velocities are not appreciably changing with period. But for short period end of the brunt period range (period from 4 to 7 minutes), phase velocity is changing drastically with period. At any given period, however, the modes with less nodes have considerably higher phase velocities. The dashed lines show the small square region where the observed (Oct. 10, 1993 ALOHA campaign) 4.6 min. and 76 m/sec wave is located. We see that it can only be the two-node mode. What is more remarkable is that there is an observed phase reversal in the 557.7 OI and the OH emission response at 95 and 87 km respectively (Fig. 12), which would again require a two-node mode (Fig. 8).

There is a feature of these modes we wish to emphasize. For these short periods, there are certain places where two curves come together and then part again. The behavior of the dispersion curves is as though the behavior of one is being taken over by the other and vice versa. What is happening in these 'kissing' places is that the energy concentrated in one atmospheric duct transfers to the other one. For more details of these energy exchanges, one can find them in the papers of Fritts and Yuan, (1989) and Jones, (1970). Fritts and Yuan used an analytical Brunt profile suited for both atmosphere and ocean.

Objections against this interpretation can be raised on the fact that the actual "Wall" event has, in addition, (1) a sharp front and (2) a strong dc component in both the OH and the OI airglow. (1) may not be a valid objection since a linear monochromatic wave can in practice possess what appears to be a sharp front with relatively small higher Fourier components. (2) is much more difficult to explain. One explanation, first proposed by Ed. Dewan, is that we have a Bore on which an instability in the form of a wave is carried. This would explain the dc airglow structure as well as the "wall" front. There are two problems with this explanation: one is that a bore possesses bulk motion which does not agree with observation (there is little horizontal wind, certainly not at 76 m/s along a more or less meridional direction). The second problem is that the explanation does not allow for the phase reversal in the emission response.

The second explanation, first proposed by Dick Pickard, is that there is a soliton. The soliton (sometimes referred to as a Bore) does not possess bulk motion and is basically a large-scale nonlinear wave packet. The soliton can have an induced Brunt oscillation (Tuan et al (1979) which, in the mesospheric region, is about 4.6 min. The spatial structures can occur as a consequence of linear instability theory and would have to be guided in the mesospheric duct resulting in the possibility of a two-node mode. Furthermore, the soliton can also have a sharp front like a "wall". Our problem is (1) to get the soliton to travel at 76 m/sec., (2) to have a soliton big enough to cover the entire sky so that it may serve as a carrier for the Brunt instability (Tuan et al, (1979). A lot more work has to be done before any definite conclusion can be made.

Summary

In this paper we have shown that, for long-period partially guided modes, a comparison of the phase shift computed from phase-shift analysis in which the effect of partial guidance only shows up implicitly, to the phase shift computed from the dispersion formula in which the partial modes (and other modes) are explicitly present, reveal only the Lamb and S₂ modes; all the other modes thought to exist by the first school are merely background to the reflection coefficient. Furthermore, these two modes are basically due to only two poles in the reflection coefficient, poles which are much closer to the real axis with much larger residues than any of the other poles.

As the period is gradually reduced the poles migrate, first to the negative imaginary axis to become virtually guided modes (in analogy with virtual bound states in nuclear physics), then to the positive imaginary axis where all the poles become observable fully guided modes. Thus, most of the poles which merely contribute to the background effect at long periods, become full fledged, fully guided modes at the short-period end. Eventually, as the period falls below the Brunt period in the Duct, all the guided modes vanish and we are left with only the Lamb Mode which remains because it does not owe its existence to either the Brunt-period or the temperature profile.

We next consider the application of the guided mode theory to a particularly spectacular ALOHA event. It appears that explanations satisfactory on some aspects of the observation can lead us into trouble on other aspects, and there is no all round satisfactory explanation. Three important features in the theory of short-period ducting should be pointed out: (1) as the period approaches the Brunt period range, all modes are fully ducted and they all (except for the Lamb mode) drop very sharply to very low horizontal phase velocities; (2) there is a 2-node mode which comes closest to the observed "wall" event (Oct. 10, 1993, ALOHA Campaign) in period and phase velocity; the mode occurs at a very sensitive region in the dispersion curve in which a small variation in period brings a large change in phase velocity, thus making a fortuitous agreement unlikely; (3) the same 2-node mode also shows a phase reversal between the peaks of the OH and the OI emissions. Further work on this problem is in progress.

Finally, we wish to point out that the appearance and disappearance of modes, the degree of interference between the ground, the tropospheric and the mesospheric ducts, the ambiguities in the use of nodes to define a particular ducted mode etc, are difficult to determine from purely numerical models. One possible quantitative study to understand precisely the mechanisms that govern the above mentioned behavior can be made through an exact analytic model. Preliminary results here seem to show considerable promise in improving our understanding of guided modes.

REFERENCES

- Francis, S. H., Acoustic-gravity modes and large-scale travelling ionospheric disturbances of a realistic dissipative atmosphere, *J. Geophys. Res.*, 78, 2278-2301, 1973a.
- Francis, S. H., Lower atmospheric gravity modes and their relation to medium-scale travelling ionospheric disturbances, *J. Geophys. Res.*, 78 8289-8295, 1973b.
- Francis, S. H., Global propagation of atmospheric gravity waves: A review, *J. Atmos. Terr. Phys.*, 37, 1011-1054, 1975.
- Friedman, J. P., Propagation of internal gravity waves in a thermally stratified atmosphere, *J. Geophys. Res.*, 71, 1033-1054, 1966.
- Fritts, D. C. and Yuan, Li, An analysis of gravity wave ducting in the atmosphere: Eckart's resonances in thermal and doppler ducts, *J. Geophys. Res.*, 94,, 18455-18466, 1989.
- Hu, N., On the application of Heisenberg's theory of S-matrix to the problem of resonance scattering and reactions in nuclear physics, *Phys. Rev.*, 74, 131-140, 1948.
- Jones, W. L., A theory for quasi-periodic oscillations observed in the ionosphere, *J. Atmos. Terr. Phys.*, 32, 1555-1566, 1970.
- Midgley, J. E. and H. B. Liemohn, Gravity waves in a realistic atmosphere, *J. Geophys. Res.*, 71, 3729, 1966.
- Pfeffer, R. L. and Zarichny, J., Acoustic-Gravity wave propagation in an atmosphere with two sound channels, *Pure and App. Geophys.*, 55, 175-199, 1963.
- Reddy, C. A., Ducting of internal gravity waves in a temperature and wind-stratified atmosphere, Internal Gravity and Acoustic waves- A Colloquium, NCAR *Tech Notes* TN-43, pp. 229-257, Natl. Center for Atmos. Res., Boulder, Colo., 1969.
- Richmond, A. D., The nature of gravity wave ducting in the thermosphere, *J. Geophys. Res.*, 83, 1385-1389, 1978.
- Tuan, T. F., R. Hedinger, S. M. Silverman and M. Okuda, On gravity-wave induced Brunt-Vaisala oscillations, *J. Geophys. Res.*, 84, 393, 1979.
- Tuan, T. F. and D. Tadic, A dispersion formula for analyzing 'Modal Interference' among guided and free gravity wave modes and other phenomena in a realistic atmosphere, *J. Geophys. Res.*, 87, 1648-1668, 1982.
- Wang, D. Y. and T. F. Tuan, Brunt-Doppler ducting of small-period gravity waves, *J. Geophys. Res.*, 93, 9916-9926, 1988.
- Yu, L., T. F. Tuan and H. Tai, On 'potential' well treatment for atmospheric gravity waves, *J. Geophys. Res.*, 85, 1297-1305, 1980.

Gravity wave modes (period=10.0 min)

Mode number	$k_x(km^{-1})$	$V_p(m/sec)$
1	0.033	316.0
2	0.044	237.9
3	0.054	193.9
4	0.067	156.1
5	0.074	141.4
6	0.087	120.4
7	0.097	107.4
8	0.109	96.1
9	0.121	86.6

Gravity wave modes (period=6.0 min)

Mode number	$k_x(km^{-1})$	$V_p(m/sec)$
1	0.055	316.0
2	0.093	186.6
3	0.108	162.1
4	0.169	103.3
5	0.211	82.7
6	0.235	74.3
7	0.301	57.9
8	0.344	50.7
9	0.370	47.1

Gravity wave modes (period=4.6 min)

Mode number	$k_x(km^{-1})$	$V_p(m/sec)$
1	0.072	316.0
2	0.095	238.6
3	0.326	69.9
4	0.628	36.2

Gravity wave modes (period=4.2 min)

Mode number	$k_x(km^{-1})$	$V_p(m/sec)$
1	0.078	316.2
2	0.551	45.3

Gravity wave modes (period=4.0 min)

Mode number	$k_x(km^{-1})$	$V_p(m/sec)$
1	0.083	316.3

Table 1: Fully Guided Gravity Wave Modes for Periods 10, 6, 5, 4.6, 4.2, 4.0 min.

PARTIALLY GUIDED GRAVITY WAVE MODES (PERIOD=3.49 HOURS)

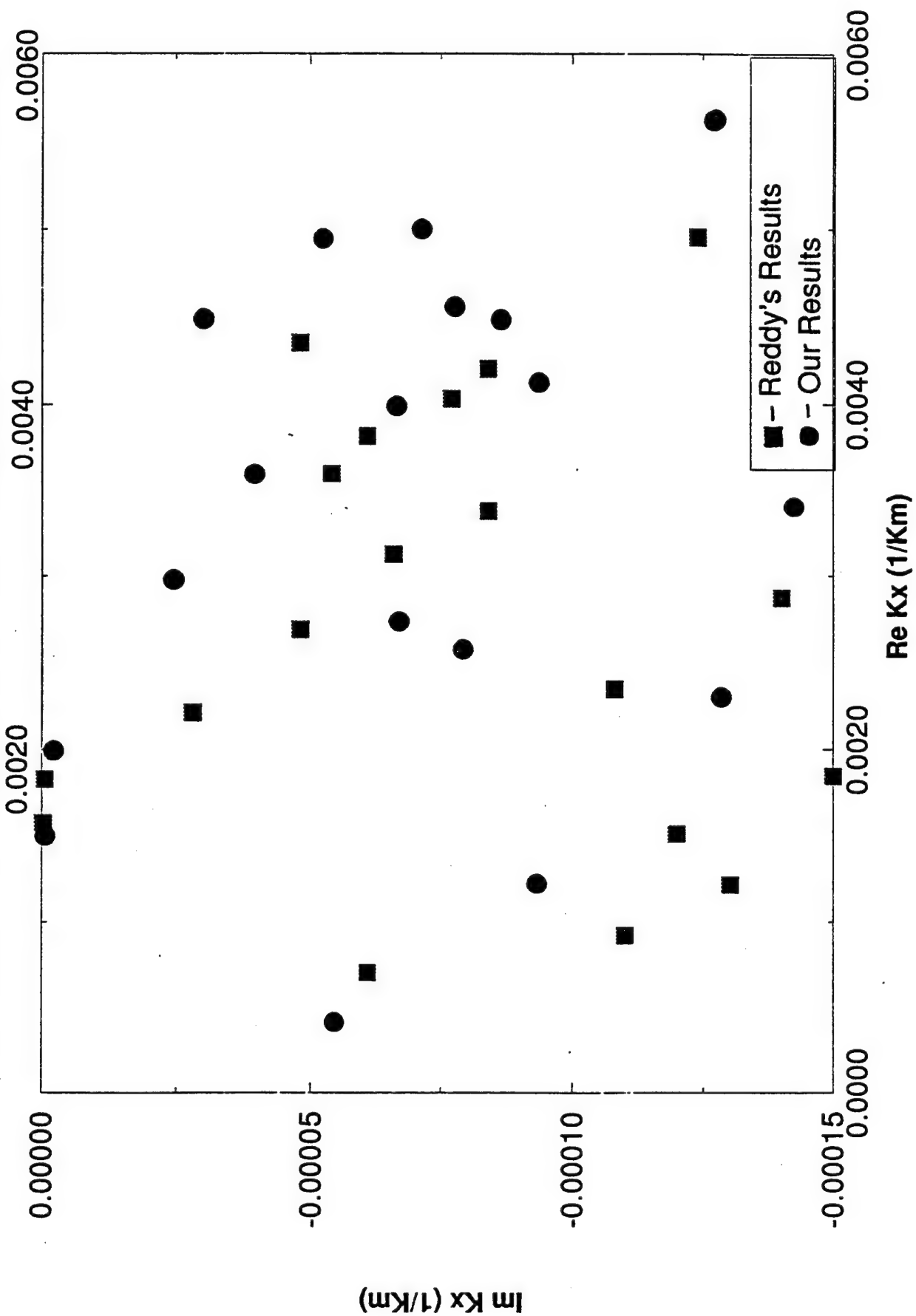


FIGURE 1

Phase Shift (Period=30 min.)

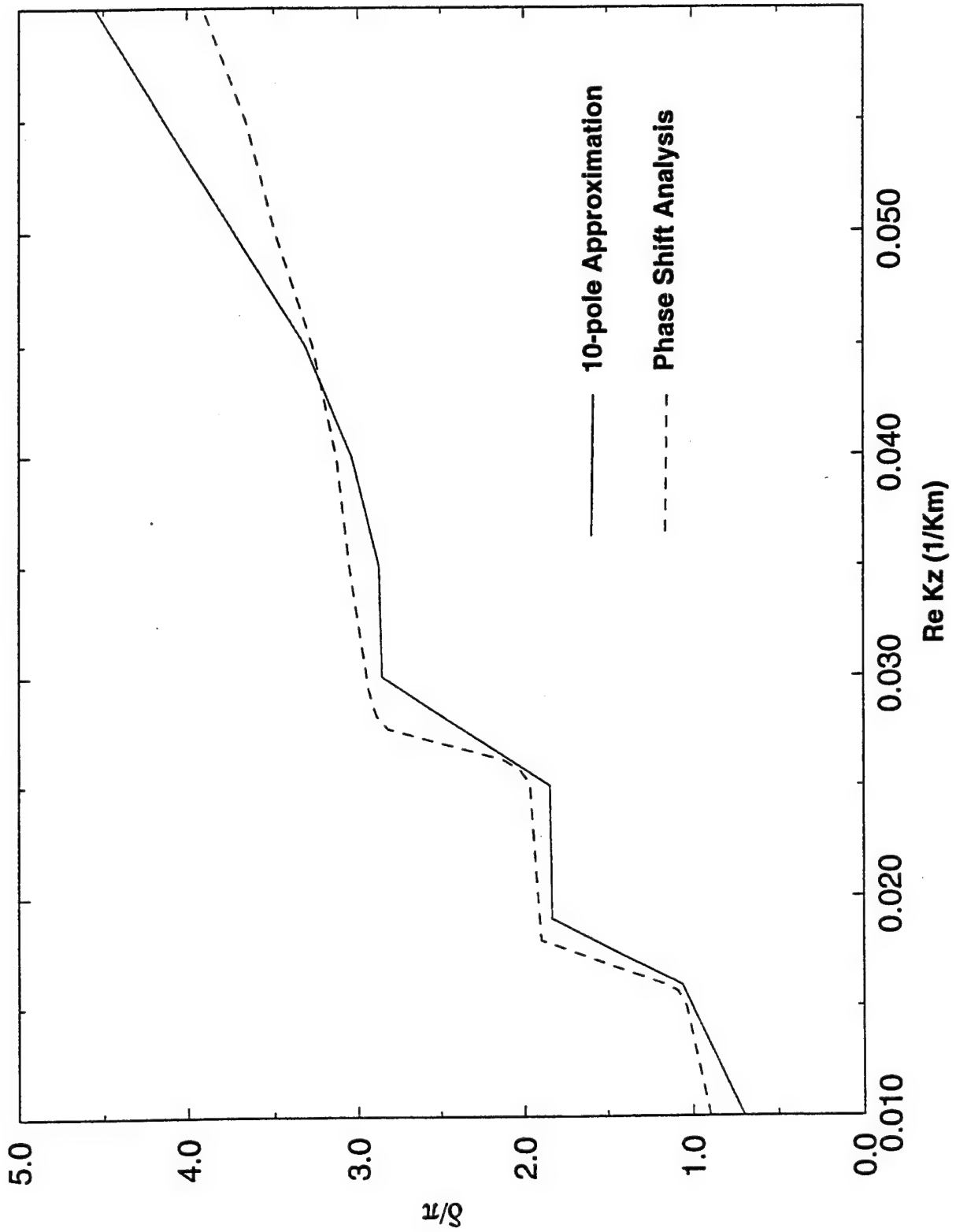


FIGURE 2

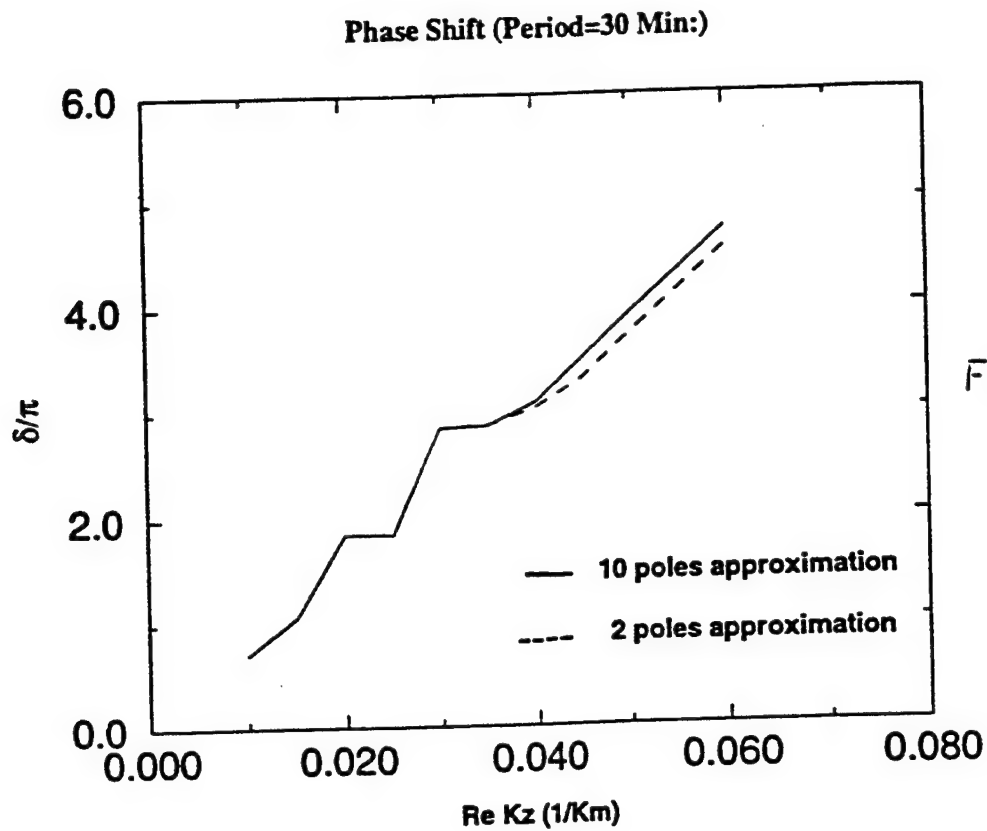


FIGURE 3

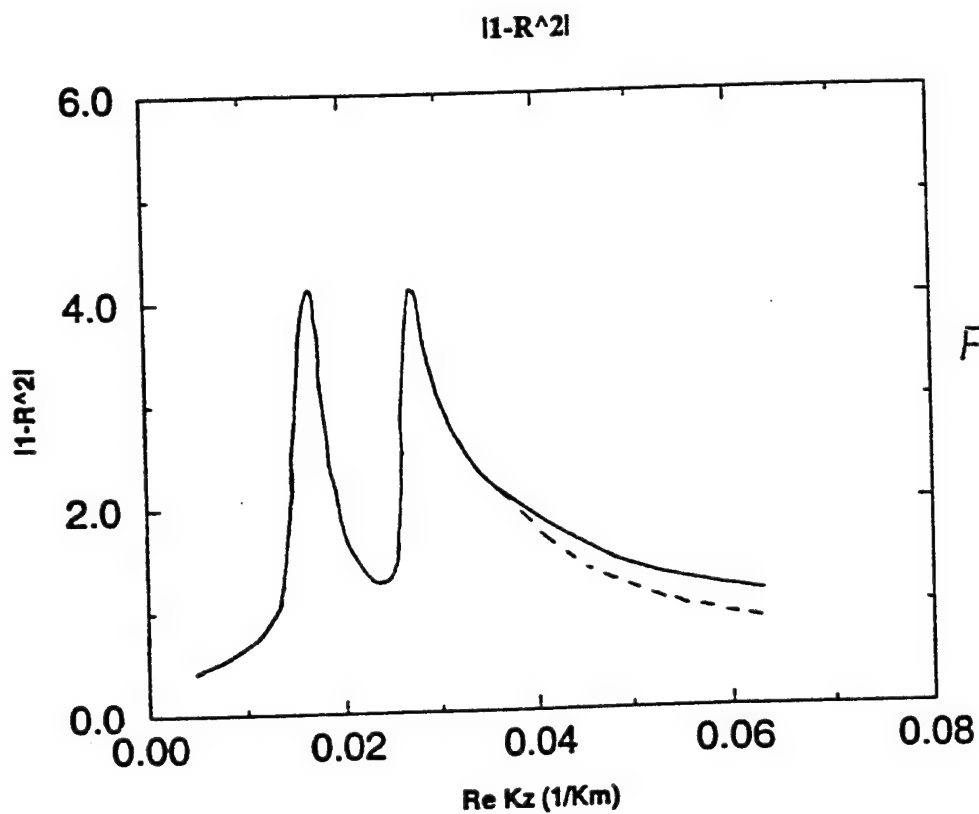
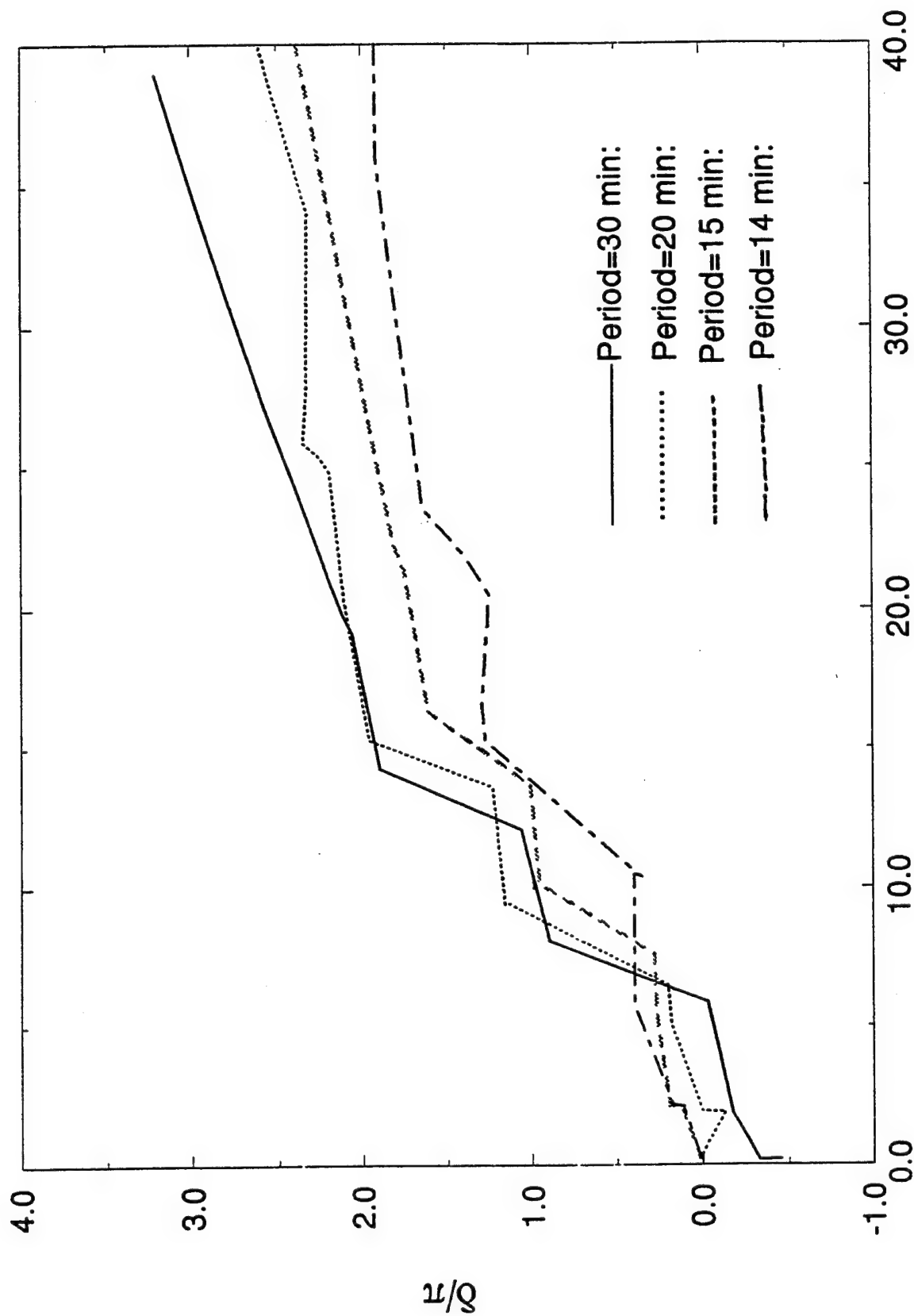


FIGURE 4

Phase Shift



λ^2 (Sec^2/Km^2) FIGURE 5

Migration of Kz for some gravity wave modes

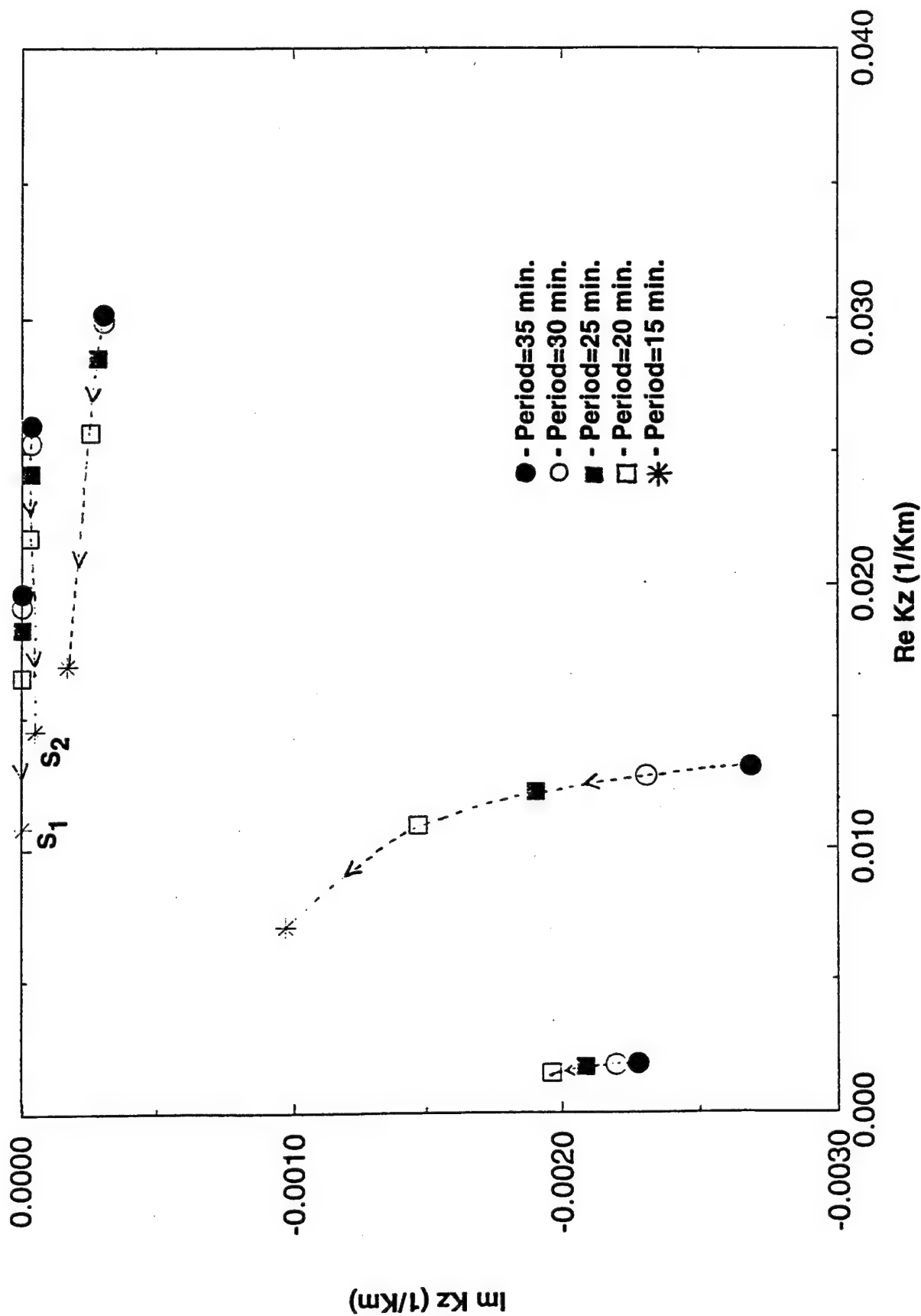


FIGURE 6

Migration of S1 and S2 modes

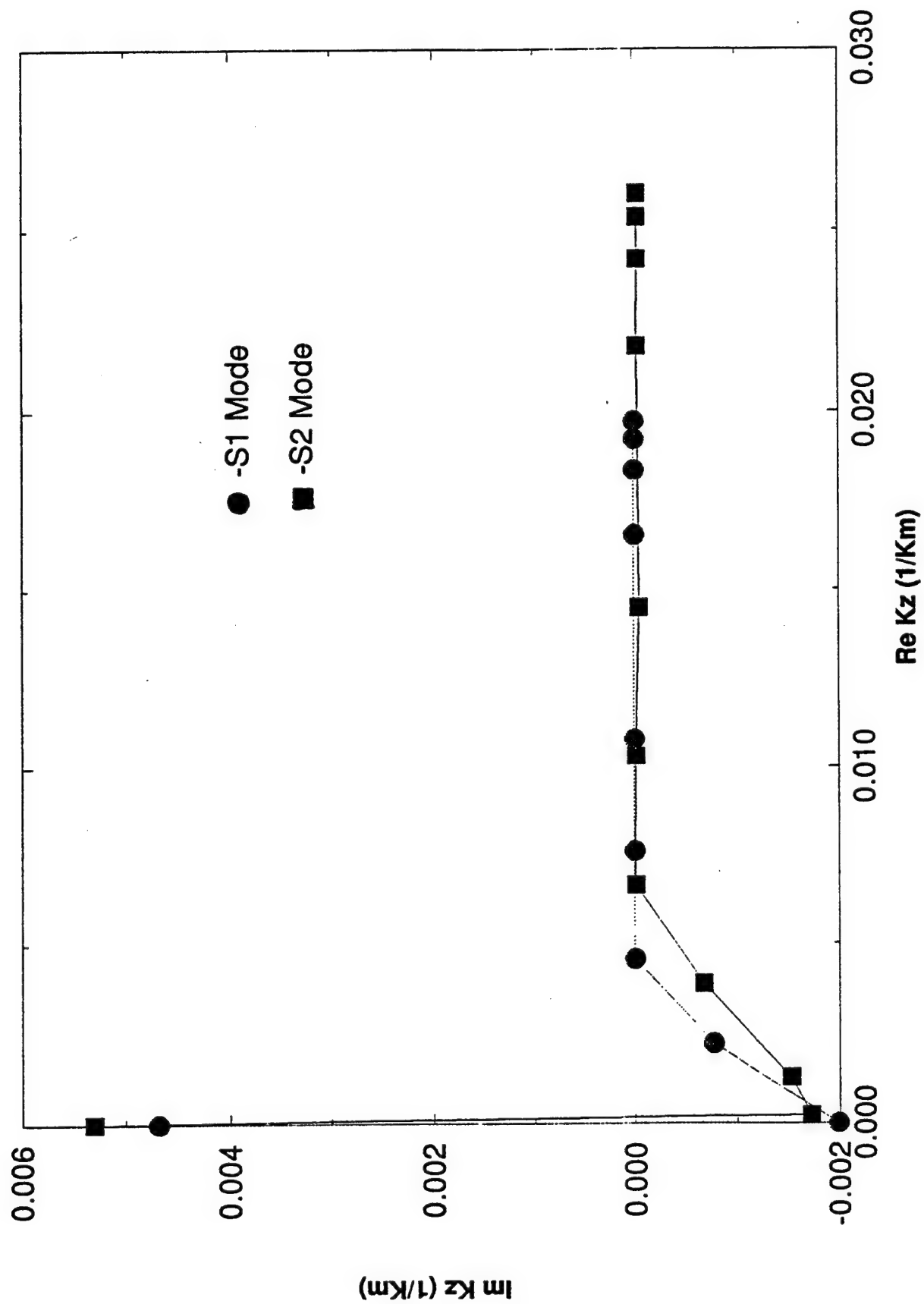
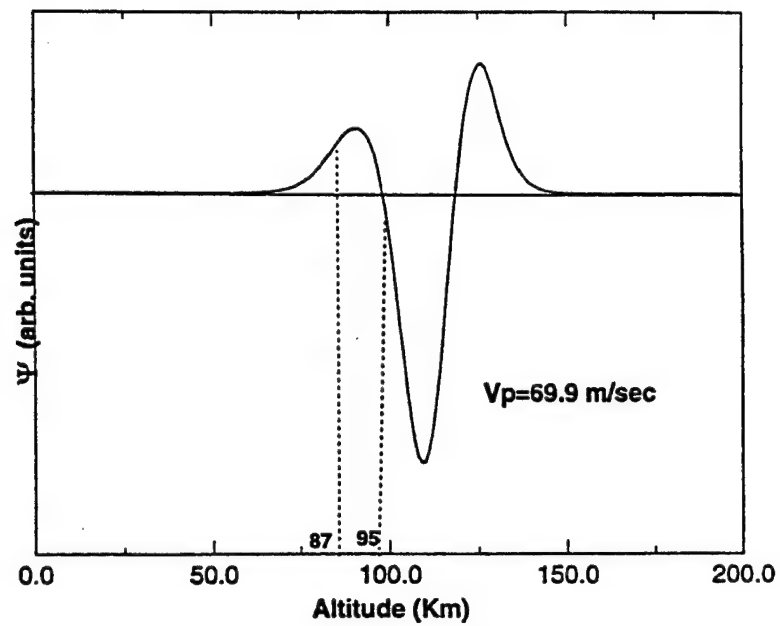


FIGURE 7

A Gravity Wave Mode for Period=4.6 min.



Kinetic Energy Distribution

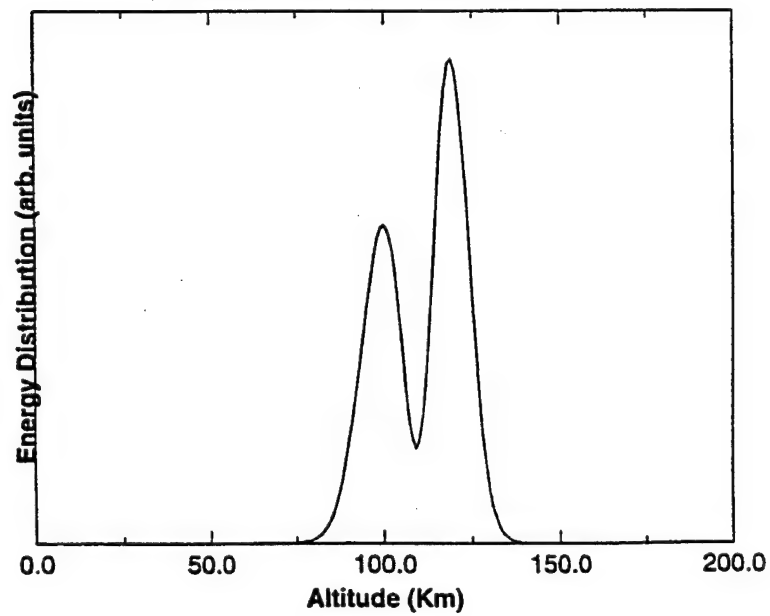
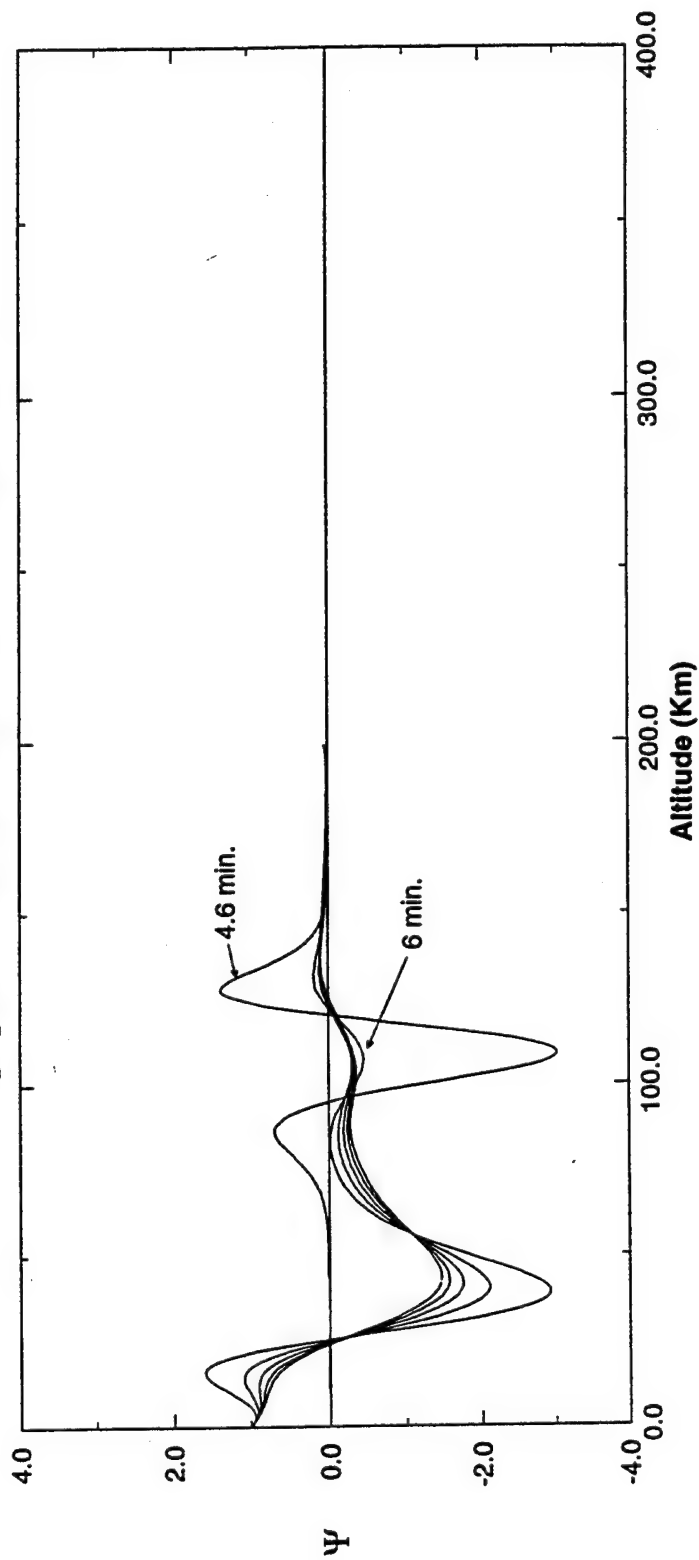


FIGURE 8

Changing behavior of S2 mode for different short periods



S2 mode for Period=2 hours

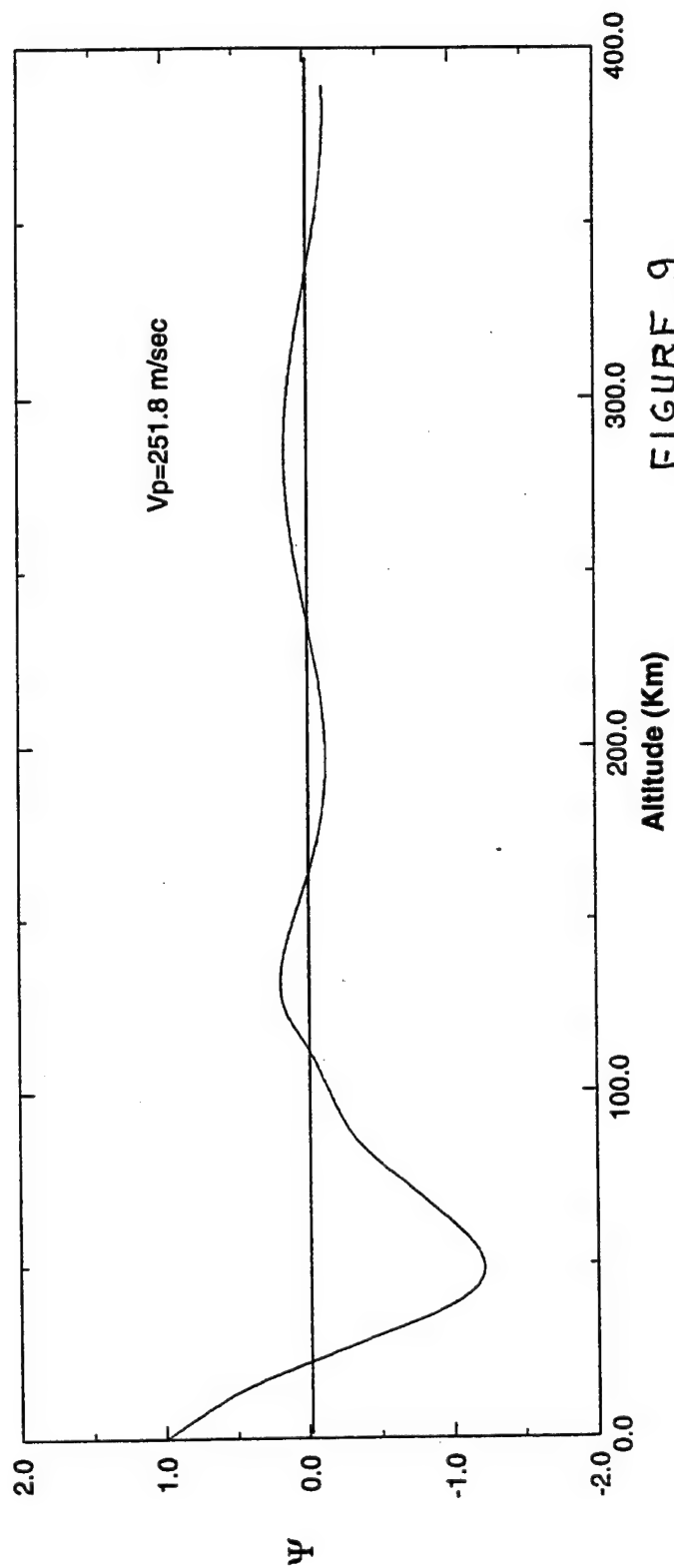


FIGURE 9

Period (min.)

2-node mode

3-node mode

4-node mode

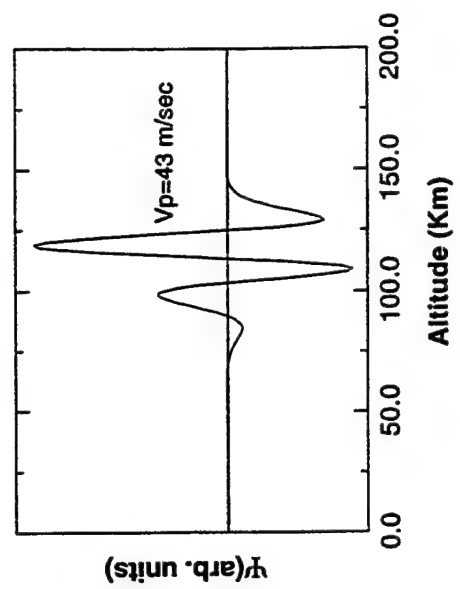
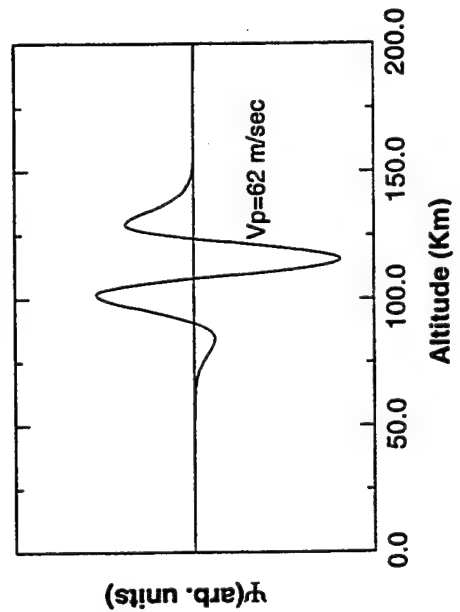
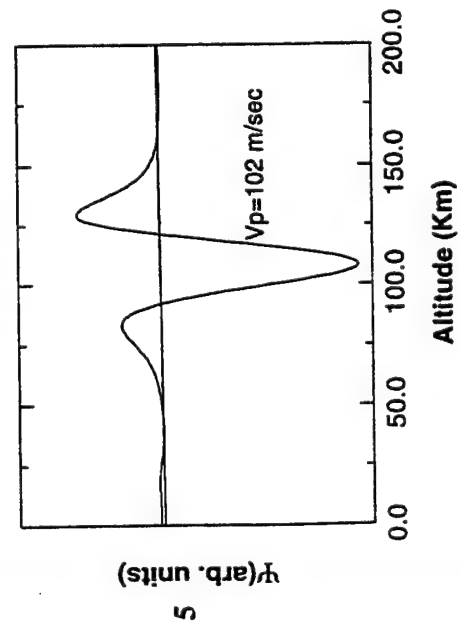
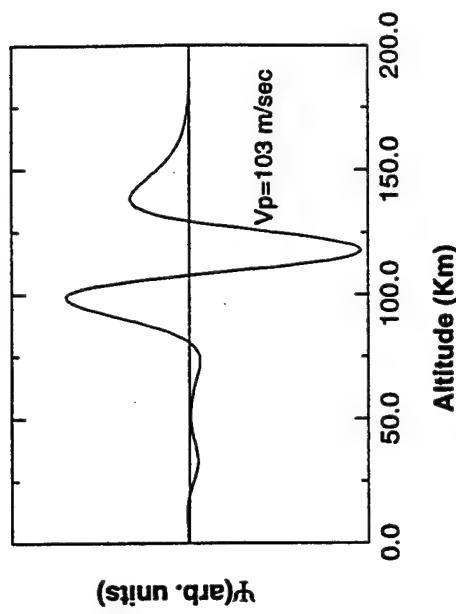
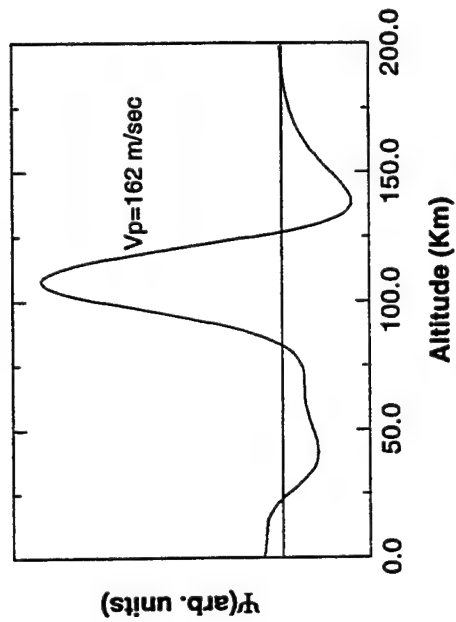
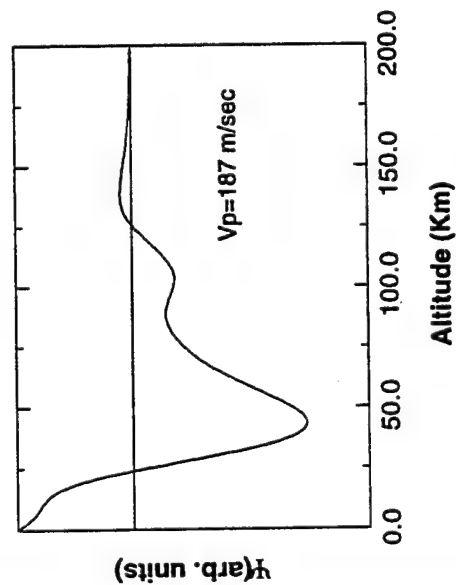
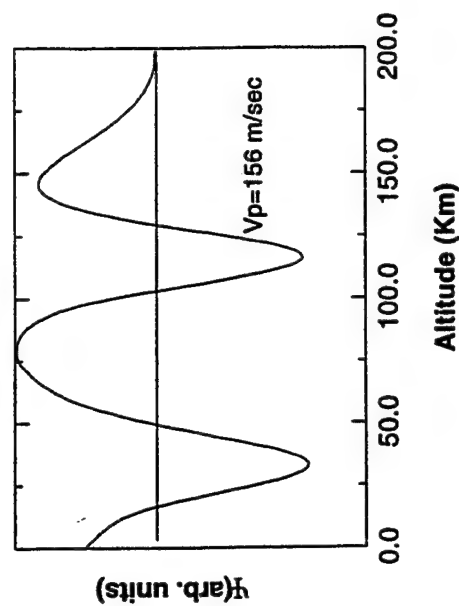
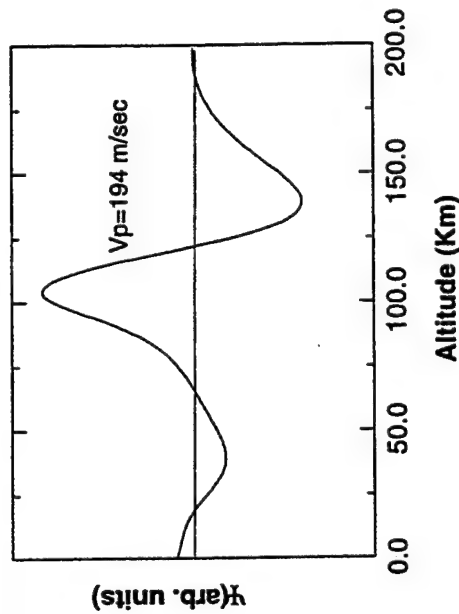
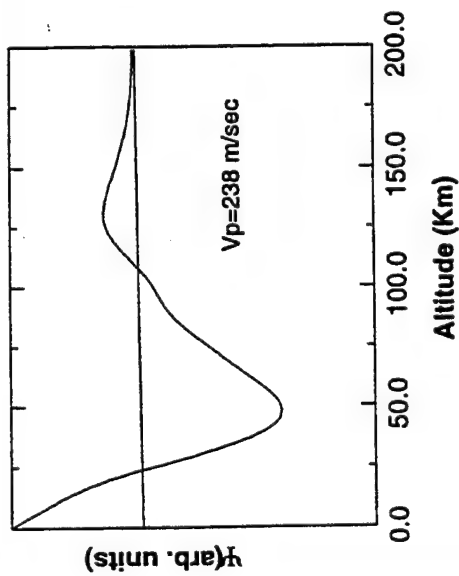


FIGURE 10

Dispersion Curves for Fully Guided Gravity Wave Modes (For smoothed c and Brunt period profiles)

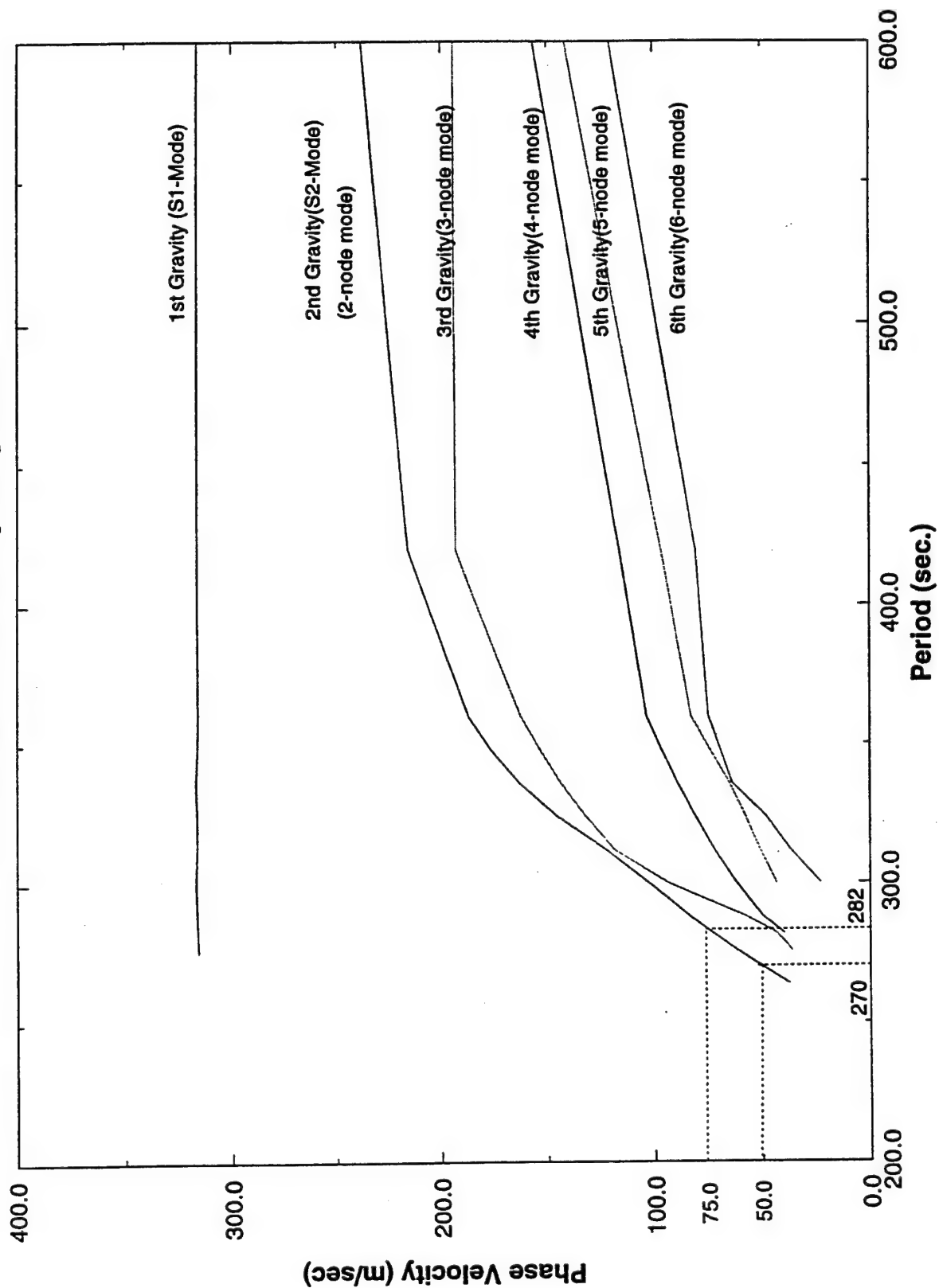


FIGURE 11

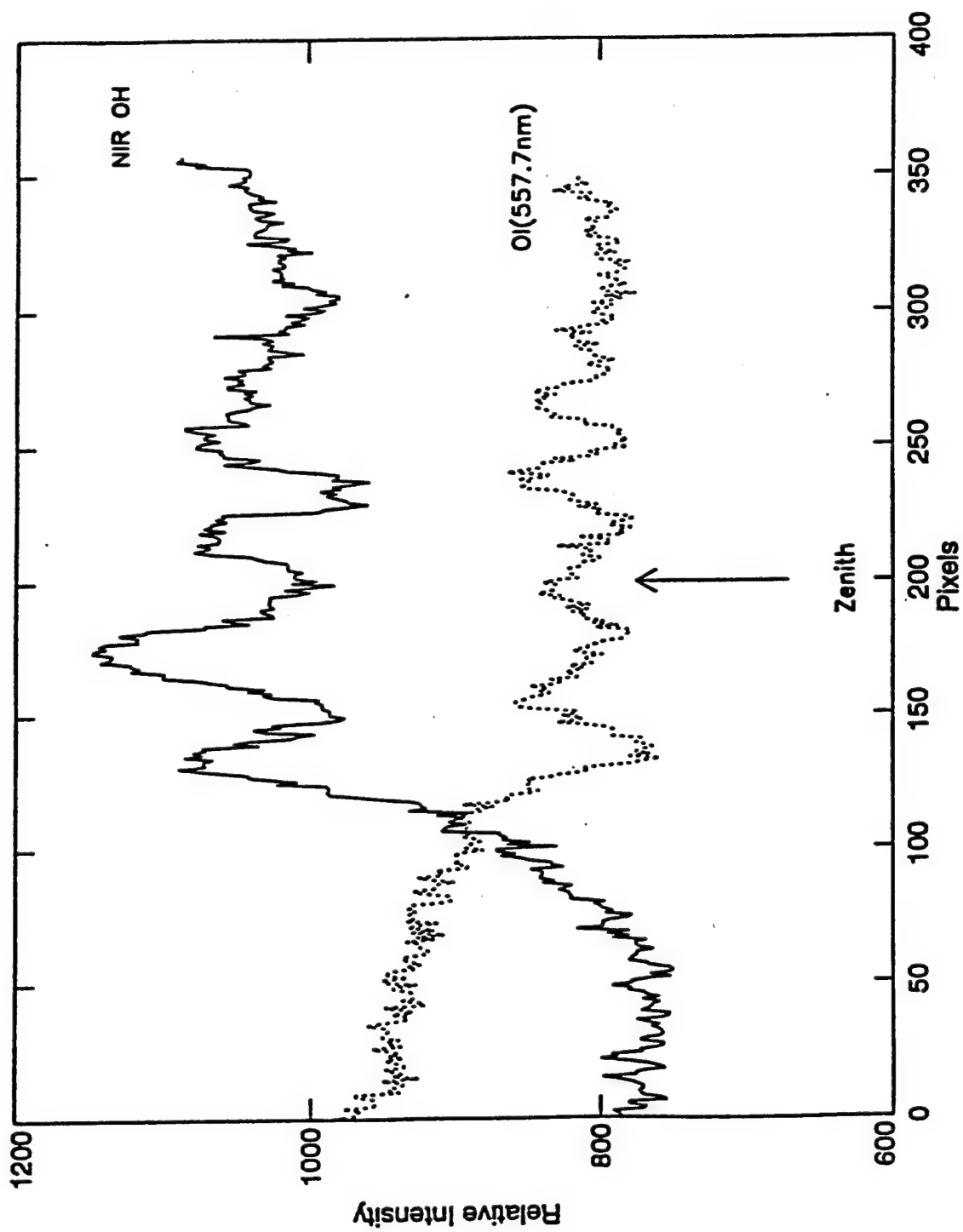


FIGURE 12

6 Nonlinear Response of Minor Atmospheric Species and the OH Emission Layer to Linear Gravity Waves (GW) in the Presence of Realistic Horizontal Winds; the effects of Critical Layers on the Response

1. Introduction

We begin this Chapter with an investigation of the effects of GW on typical minor species density profiles. We shall see that the nonlinear response can be important at certain height levels in the profile and that the winds can enhance as well as diminish the wave-induced diffusion arising from the nonlinear response. We have in the past examined the effect of nonlinear response due to linear GW but did not include any consideration of the winds (Isler et al, preprint, 1995); the wave-induced diffusion in that case does not depend on the direction of wave propagation. In the present work the diffusion does depend on the direction of the wave propagation since the wave frequency is modified by the Doppler shift due to the winds. The density profiles are, of course, also affected by both the winds and the nonlinear response terms. In these calculations we use an isothermal background atmosphere with a realistic wind profile. The latter is based on the NCAR-CEDAR (1990) wind model modified by the tidal wave models of Forbes and Vial (1989). The results show the important effects of the direction of wave propagation on the higher order nonlinear response terms in the density profile.

Since along certain directions of wave propagation critical layers can occur when the propagation velocity equals the wind velocity along the propagation direction, we have decided to investigate the behavior of the minor species in the presence of the critical layer. We use the wave solutions provided in Section V and consider only the first order response for the proximity of the critical-layer region. The second and higher order responses will be used for the non-critical layer region. A brief investigation of the higher order response terms near the critical layer show that they are usually much less than the first order term. Thus, in the following sections we shall (1) derive the perturbation theory for treating the higher order terms in the nonlinear response; (2) use the KBM renormalization technique to remove the secularity to obtain the wave-induced diffusion; (3) show the effect of these terms at different propagation angles on the typical minor species profile; (4) show the wave-induced diffusion velocity as a function of height for

typical small-scale GW; (5) plot the integrated emission profile as a function of propagation angle; (6) consider the response in the proximity of a critical layer region using only the linear response terms.

2. Formulation

The basic equation for the typical minor species with number density, n , are given by:

$$\frac{\partial n}{\partial t} = -\nabla \cdot (n\bar{v}_t) \quad (1)$$

$$\bar{v}_t = \bar{v} + \bar{V}_0 + \bar{k}W_d \quad (2)$$

\bar{v} = GW velocity

where

\bar{V}_0 = wind velocity (assumed horizontal)

W_d = vertical drift velocity

Using plane GW propagating in horizontally stratified atmosphere and assuming that $n = n_0 + n'$ where n' is the total perturbation, we obtain the following equation:

$$\frac{\partial \psi}{\partial t} = -V_{ox} \frac{\partial \psi}{\partial x} - u \frac{\partial \psi}{\partial x} - w \frac{\partial \psi}{\partial z} - S\psi - S - \frac{1}{n_0} \frac{\partial (n_0 W_d)}{\partial z} \quad (3)$$

where

$$\psi = \frac{n'}{n_0}$$

$$S = \frac{\partial u}{\partial x} + \frac{\partial w}{\partial z} + \frac{1}{n_0} \frac{\partial n_0}{\partial z} w$$

and u and w are the horizontal and vertical particle velocities of the GW, assuming plane waves

Expanding the solution in terms of perturbation series:

$$\psi = \lambda \psi_1 + \lambda^2 \psi_2 + \lambda^3 \psi_3 + \dots \quad (5)$$

$$W_d = \lambda W_{d1} + \lambda^2 W_{d2} + \lambda^3 W_{d3} + \dots \quad (6)$$

$$\bar{v} = \bar{i}u + \bar{k}w, \quad (7)$$

we obtain the following partial differential equation:

$$\frac{\partial \psi_n}{\partial t} = -\frac{1}{n_0} \frac{\partial(n_0 w_{d2})}{\partial z} - V_{0x} \frac{\partial \psi_n}{\partial x} - u \frac{\partial \psi_{n-1}}{\partial x} - w \frac{\partial \psi_{n-1}}{\partial z} - S \psi_{n-1} \quad (8)$$

Using a multilayer model and a constant wind velocity for each layer, the solution to the above equation in each layer to the first and second order in λ is given by:

$$\psi_1 = \frac{iS}{\Omega} \quad (9)$$

and ψ_2 is given in terms of ψ_1 by

$$\text{Re} \frac{\partial \psi_2}{\partial t} = -\text{Re} \frac{\partial \psi_1}{\partial x} - V_{0x} \text{Re} \frac{\partial \psi_1}{\partial x} - \text{Re} w \frac{\partial \psi_1}{\partial z} - \frac{1}{n_0} \frac{\partial(n_0 w_{d2})}{\partial z} - \text{Re} S \text{Re} \psi_1 \quad (10)$$

where Ω is the Doppler-shifted frequency and we need to take the real parts everywhere since products of complex quantities are involved.

w_{d1} can be derived from the steady state unperturbed solution

$$w_{d1} = -D \left(\frac{1}{n_0} \frac{\partial n_0}{\partial z} + \frac{mg}{kT} \right) \quad (11)$$

where

- D = the eddy diffusion coefficient
- n_0 = the unperturbed number density
- m = the molecular mass of the minor species
- T = the temperature

Using the KBM renormalization method to remove the secularity, we obtain:

$$\frac{1}{n_0} \frac{\partial(n_0 w_{d2})}{\partial z} = (1-|R|^2)(k_x D_1 \cos \phi + k_z D_2) \left(\frac{1}{n_0} \frac{\partial n_0}{\partial z} + \frac{1}{H} \right) \quad (12)$$

$$\text{where } D_1 = \frac{\overline{uw}}{2\Omega}, \quad D_2 = \frac{\overline{w}^2}{2\Omega} \quad (13)$$

$$\cos \phi = \frac{k_z}{(k_z^2 + \eta^2)^{1/2}} \quad (14)$$

and \overline{u} and \overline{w} are the envelopes of the GW velocity fields. Since we are dealing with an uniform isothermal atmosphere within each layer, they are simple exponentials. It is easy to verify by substitution that the solution to (12) within each layer is given by:

$$w_{d2} = (1 - |R|^2)(k_x D_1 \cos \phi + k_z D_2) \quad (15)$$

From (13) the drift velocity increases exponentially (i.e. $\propto \exp(z/H)$) in an isothermal atmosphere. As can be seen, the vertical wave-induced drift velocity vanishes for a stationary vertical wave ($R = 0$). Figure 1 shows typical vertical drift velocity as a function of altitude. For a wave with a horizontal phase velocity of 70 m/s and a period of half an hour, it is of the order of 2 to 3 cm/sec at OH peak heights. It is less than one percent of the typical vertical wave velocity which is of the order of a few meters per sec. (see Table I). Fig. 2 shows the response of a generic minor species profile to a GW of 30 m/sec and a period of 30 min. without the wind and at an altitude of 87 km. Figure 3 shows the temporal response of the same profile with a realistic climatological zonal wind. As can be seen there is a considerable difference. The wind appears to have rounded off the sharper edges in the troughs, due no doubt in part to the much smaller third order response term (given by successive long and short dashes).

Figure 4 shows the spatial response in the OH emission profile in the presence of winds. There is clearly a difference arising from the higher order (second and third) terms. The GW in this case is propagating along an azimuthal angle of 158° (approximately North West). Clearly the direction here is very important. The same wave propagating due south would produce no significant spatial response (see Figure 5). Figure 6 shows the response of a minor species profile to a GW propagating along the zonal direction when there is a critical layer. Since our calculation is strictly numerical, we can only approach a critical layer. The dashed line indicates where we can no

longer continue with the numerical method. The critical layer occurs at about 93 km.

In computing the integrated brightness we will use only the primary reactions without quenching:



The integrated brightness is then given by:

$$B = k \int_{75}^{110} [H(z, \Omega)][O_3(z, \Omega)] dz \quad (17)$$

where $[H]$ and $[O_3]$ are the total concentrations of H and O_3 and include the unperturbed concentration plus the first three order corrections; k is the chemical rate coefficient and Ω is the Doppler-shifted frequency (the intrinsic frequency). Figure 7 shows the integrated brightness of OH perturbed by a gravity waves with period of 30 min and phase velocities of 60, 65 and 70 m/sec. As can be seen the wind affects the total brightness only if the wave propagates along certain directions and the effect is not very significant.

3. Critical layers

To study this difficult problem we use only the first order linear response of the minor species. From (9) we obtain:

$$\psi_1 = \frac{n'_1}{n_0} = \frac{i}{\Omega} \left(\frac{\partial u}{\partial x} + \frac{\partial w}{\partial z} + \frac{1}{n_0} \frac{\partial n_0}{\partial z} w \right) \quad (18)$$

where u and w are no longer given by the isothermal Gravity Wave model but by the optical model used in Section 4. Since the x and t dependence for the optical model remains the same as the Hines model, i.e. they are both sinusoidal, we may rewrite (18) as:

$$\begin{aligned}\frac{n'_1}{n_0} &= \frac{i}{\Omega} \left[\frac{g}{c^2} + \frac{\omega_b^2}{g} - \frac{\Omega^2}{g} + \frac{1}{n_0} \frac{\partial n_0}{\partial z} \right] w - \frac{1}{mN_0 g} \frac{\partial(\Delta p)}{\partial z} \\ &\approx \frac{i}{\Omega} \left[\frac{1}{H} - \frac{\Omega^2}{g} + \frac{1}{n_0} \frac{\partial n_0}{\partial z} \right] w - \frac{1}{mN_0 g} \frac{\partial(\Delta p)}{\partial z}\end{aligned}\quad (19)$$

where m is the average major species mass, N_0 , the major species density, and Δp , the pressure variation. The second line of (19) is obtained from the first by using the uniform isothermal formula for the Brunt frequency. We can also eliminate the pressure derivative by simply using the coupled first order GW equations to obtain:

$$\frac{n'_1}{n_0} = \frac{i}{\Omega} \left[\frac{g}{c^2} + \frac{1}{n_0} \frac{\partial n_0}{\partial z} \right] w + \frac{1}{c^2} \frac{\Delta p}{mN_0} \quad (20)$$

Using the Optical Model for w and Δp we obtain the linear response for the hydrogen density profile in Figure 9. The GW is based on a particular observed GW by Mike Taylor in May 1988 at the Mountain Research Station in Colorado (Taylor et al, 1993). It has a horizontal phase velocity of 30 m/sec, a period of 15.5 min, and propagates with an azimuthal angle of 50° . The wind profile for May at Colorado along the direction of wave propagation is shown in Figure 8. The critical layer is marked by the dashed line at about 97.5 km. The only free parameter we use here is the magnitude of the GW which could not be directly measured. In keeping with linear approximation we have used a velocity and pressure wave amplitude corresponding to a 2% major species density perturbation at a height of 90 km.

4. OH emission profile and the critical layer.

We have not yet obtained the OH emission profile with a realistic atmosphere and wind profiles. In this section we use only the Optical Model in an isothermal atmosphere instead of the more realistic model of Section 4. For the wind profile we use the simple analytic approximation to the climatological profiles at Colorado for local midnight. A zonal profile for May, June and July is given in Figure 10. Thus, using the integrand of (17) for the luminosity profile, we obtain Figure 11 for a GW with a horizontal phase velocity of 30 m/sec propagating in the zonal direction. Fig. 12 shows the response of the OH luminosity profile to the same GW propagating

along a direction of 135° . In Figure 11 there is a critical layer at slightly below 95 km, whereas the critical layer disappears in Figure 12. The same GW can therefore produce critical layers along certain directions and fails to do so along others. This is of course due to the fact that the projection of the wind profile along some directions may just not be strong enough for critical layers to occur within the height range of the luminosity profile.

Bibliography

- (1) Forbes, J. M. and F. Vial, Monthly simulations of the solar semidiurnal tide in the mesosphere and lower thermosphere, *J. Atmos. Terr. Phys.*, 51 (7/8), 649, (1989)
- (2) Isler, J. R., X. Li, T. F. Tuan, F. He and R. H. Picard, Perturbation treatment of the nonlinear response of minor atmospheric species to linear gravity waves, preprint (1995)
- (3) National Center for Atmospheric Research (NCAR) CEDAR Data Base Catalog, Boulder, Colo., (1990)
- (4) Taylor, M. J., E. H. Ryan, T. F. Tuan and R. Edwards, Evidence of preferential directions for gravity wave propagation due to wind filtering in the middle atmosphere, *J. Geophys. Res.*, 98, 6047, (1993)

Second order drift velocity $Wd2$

$T=30\text{min}$ $V_x=70\text{m/s}$

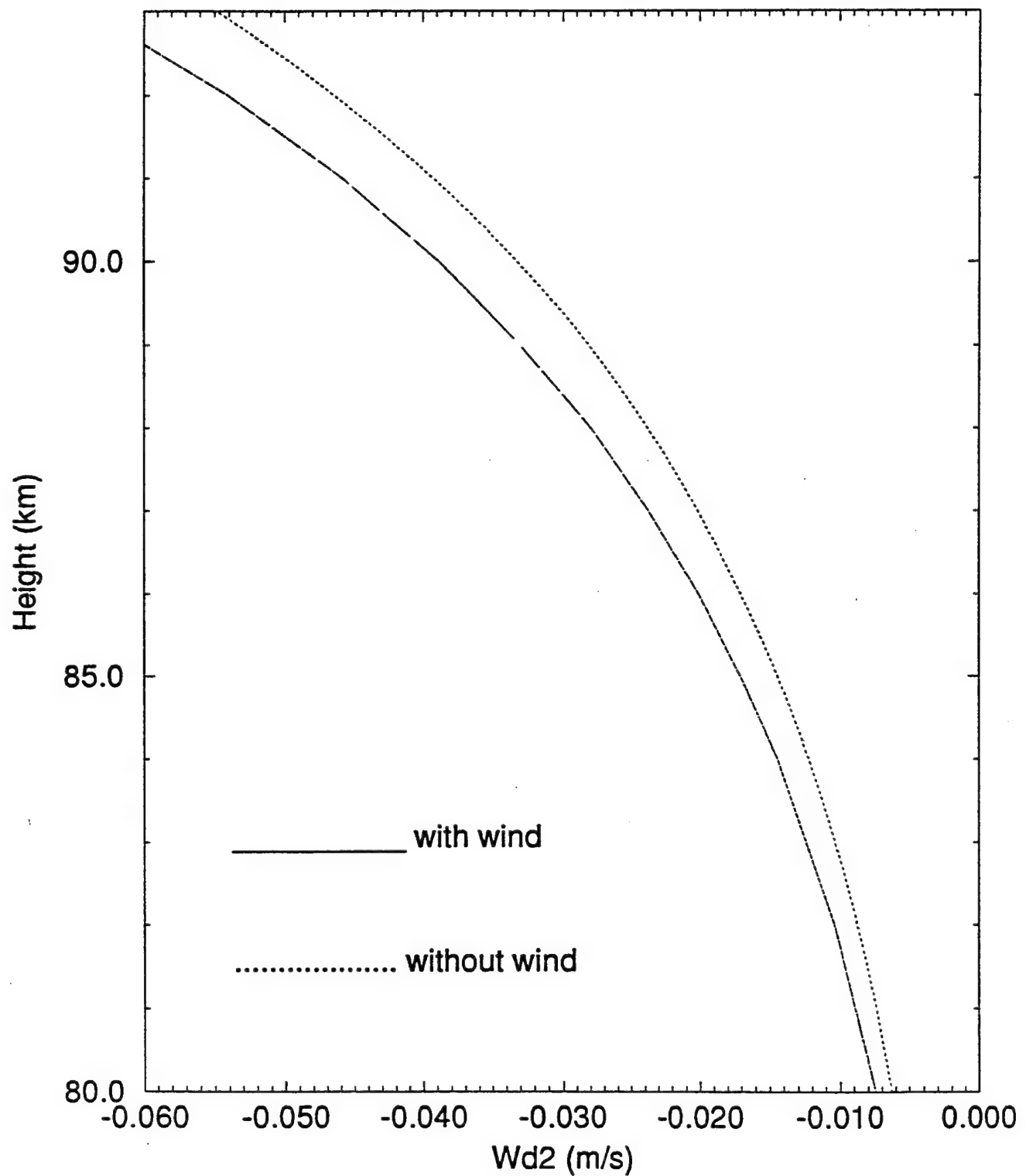


FIGURE 1

Response of the 'generic' profile without wind

T=30min Vx=30m/s Z=87km

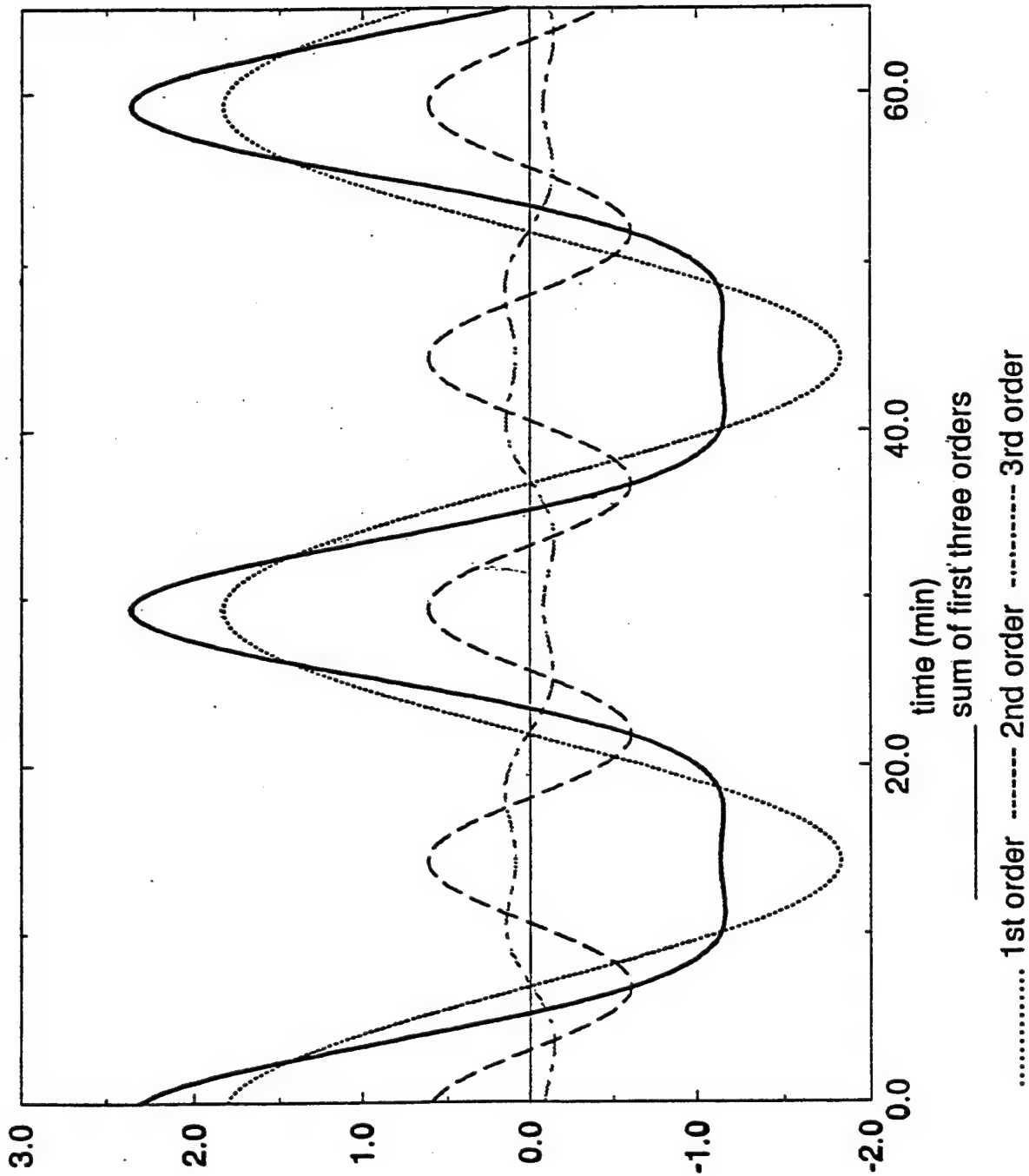


FIGURE 2

Response of the 'generic' profile with zonal wind
 $T=30\text{min}$ $V_x=30\text{m/s}$ $Z=87\text{km}$ $V_{ox}=-29\text{m/s}$ (against phase velocity)

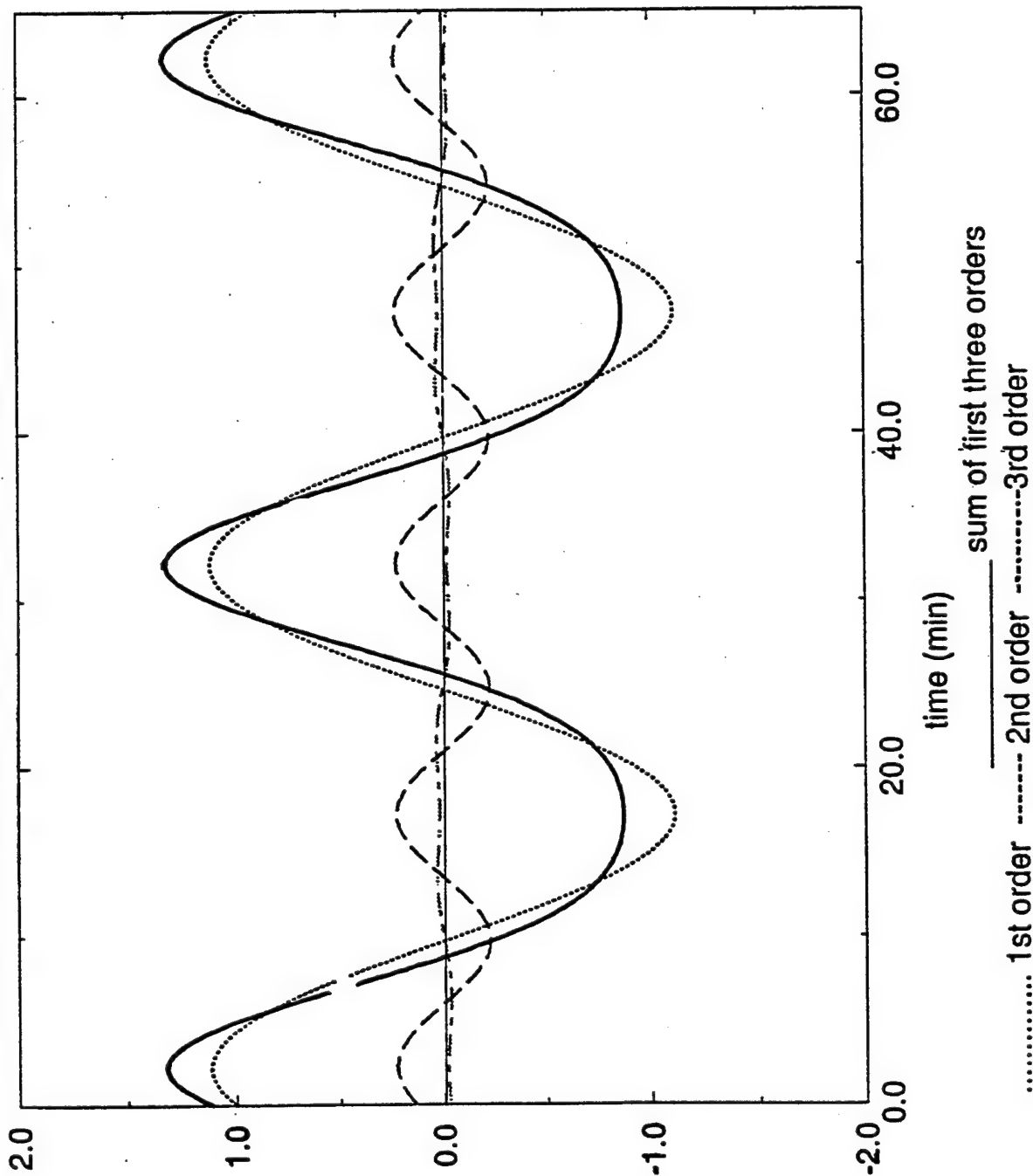


FIGURE 3

density profile of OH

T=30min vx=60m/s a=1.8E3 angle=157.5

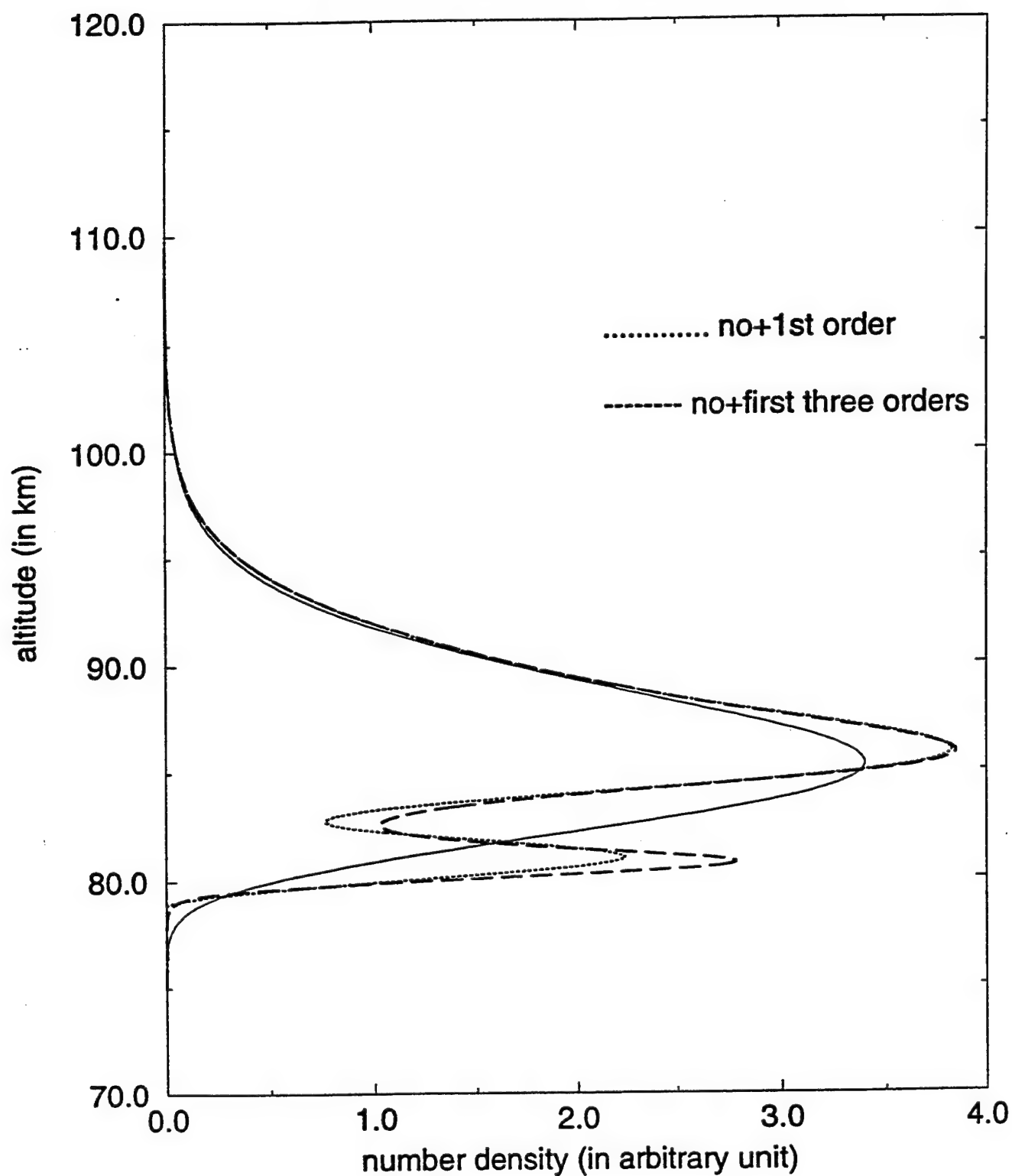


FIGURE 4

density profile of OH

T=30min Vx=60m/s a=1.8E3 angle=270

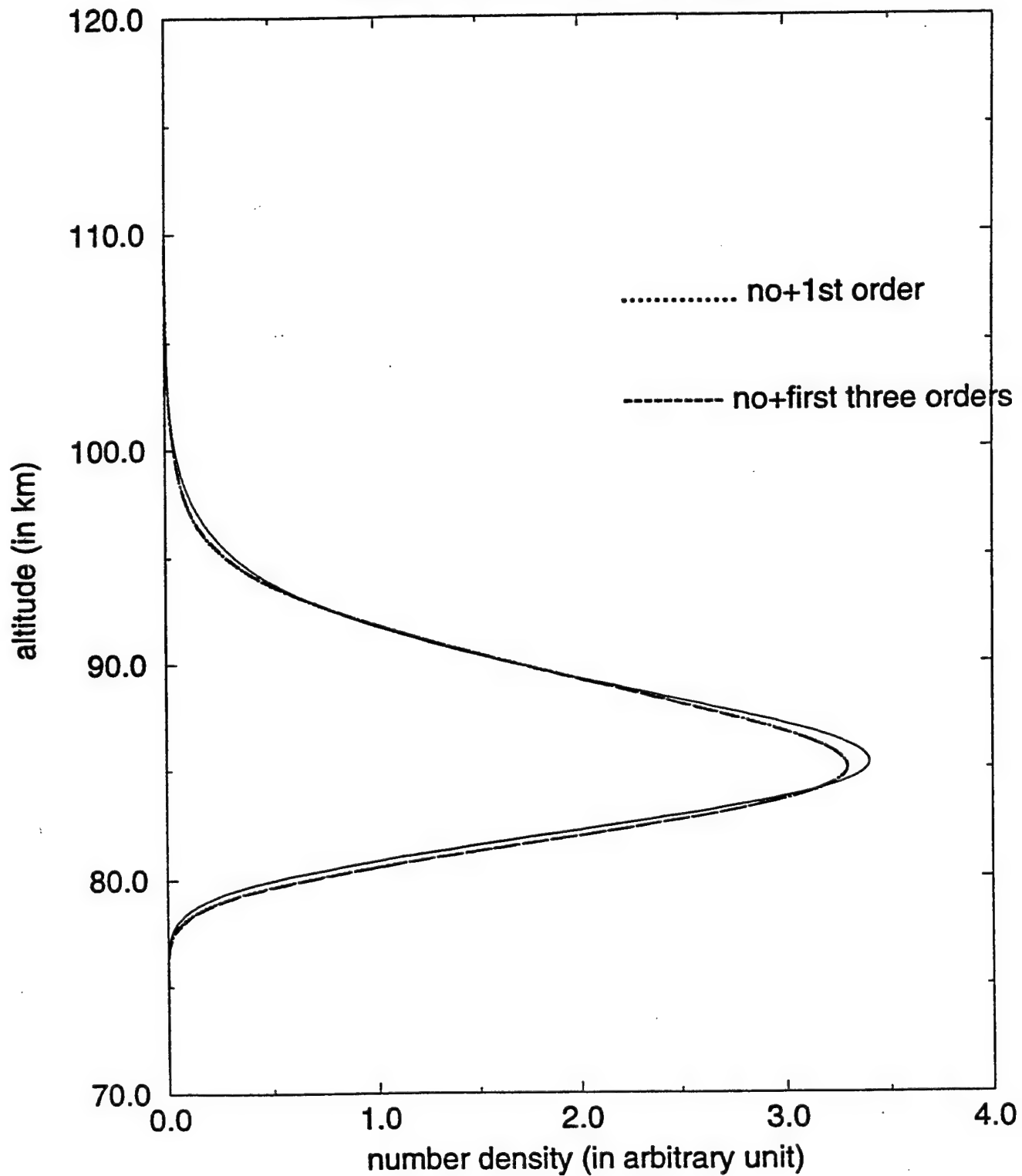


FIGURE 5

O3 T=20min Vx=20m/s A=0.03 with wind

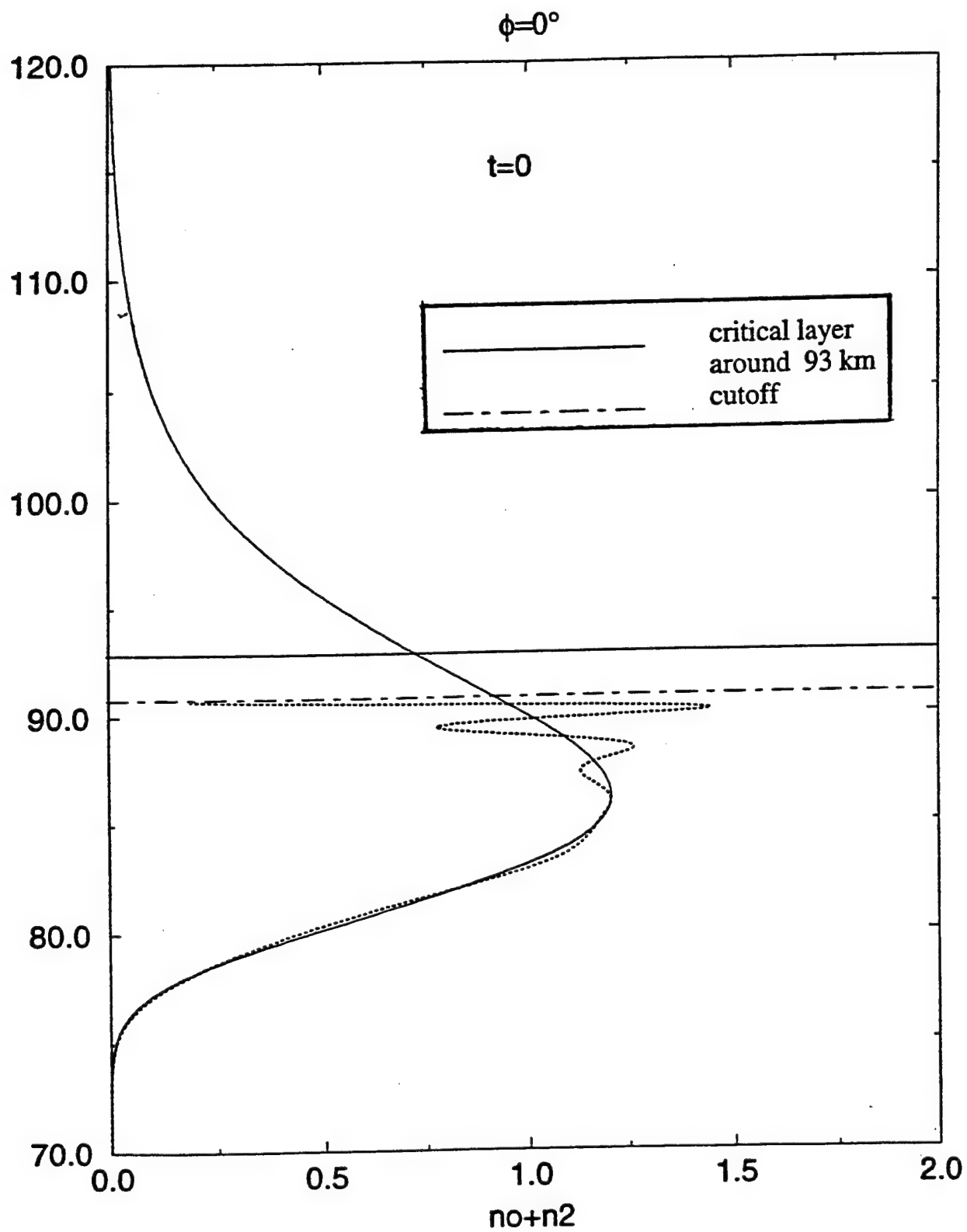


FIGURE 6

Averaged integrated brightness of OH

T=30min a=1.8E3

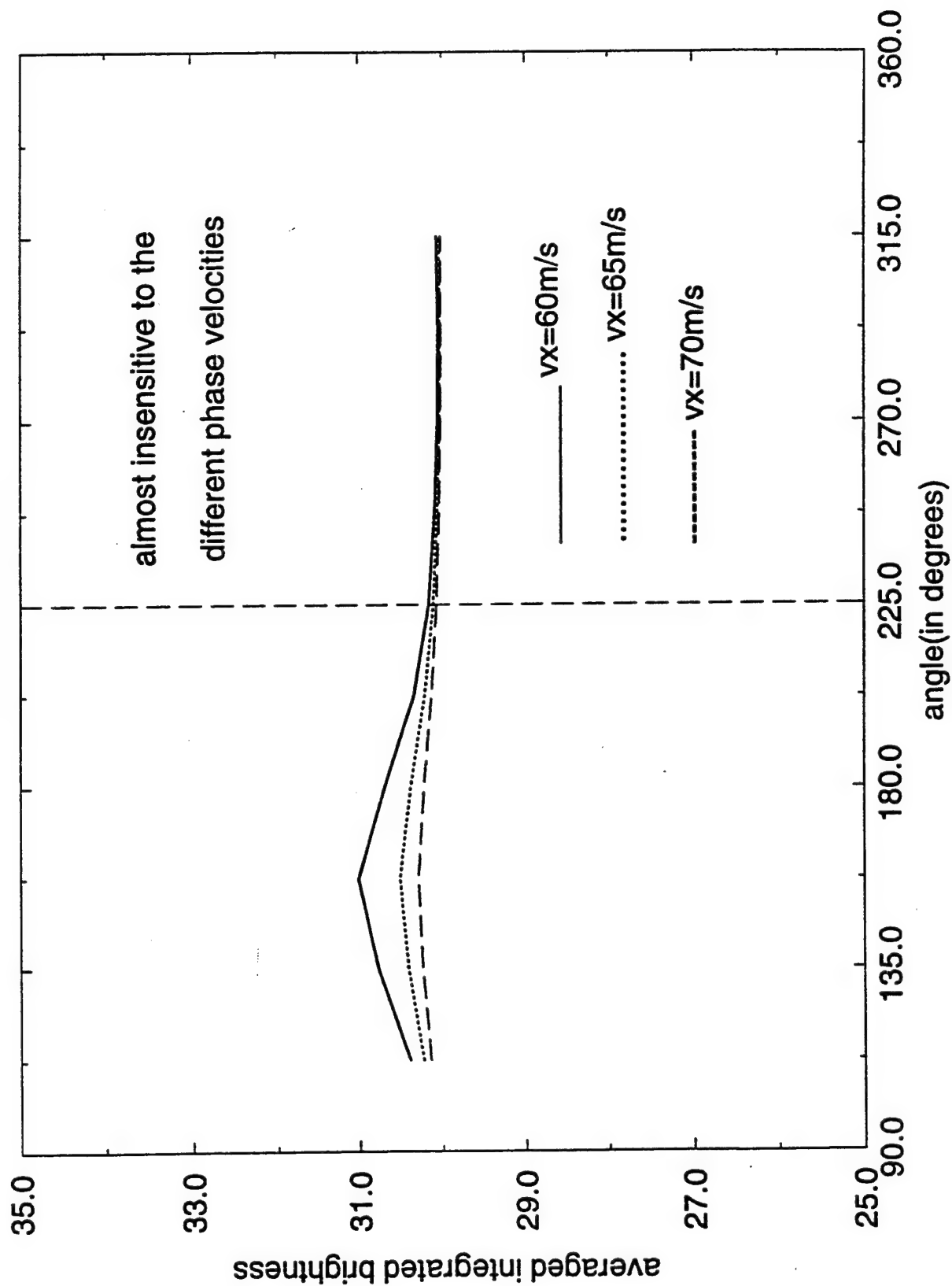


FIGURE 7

horizontal wind profile

$a=50$

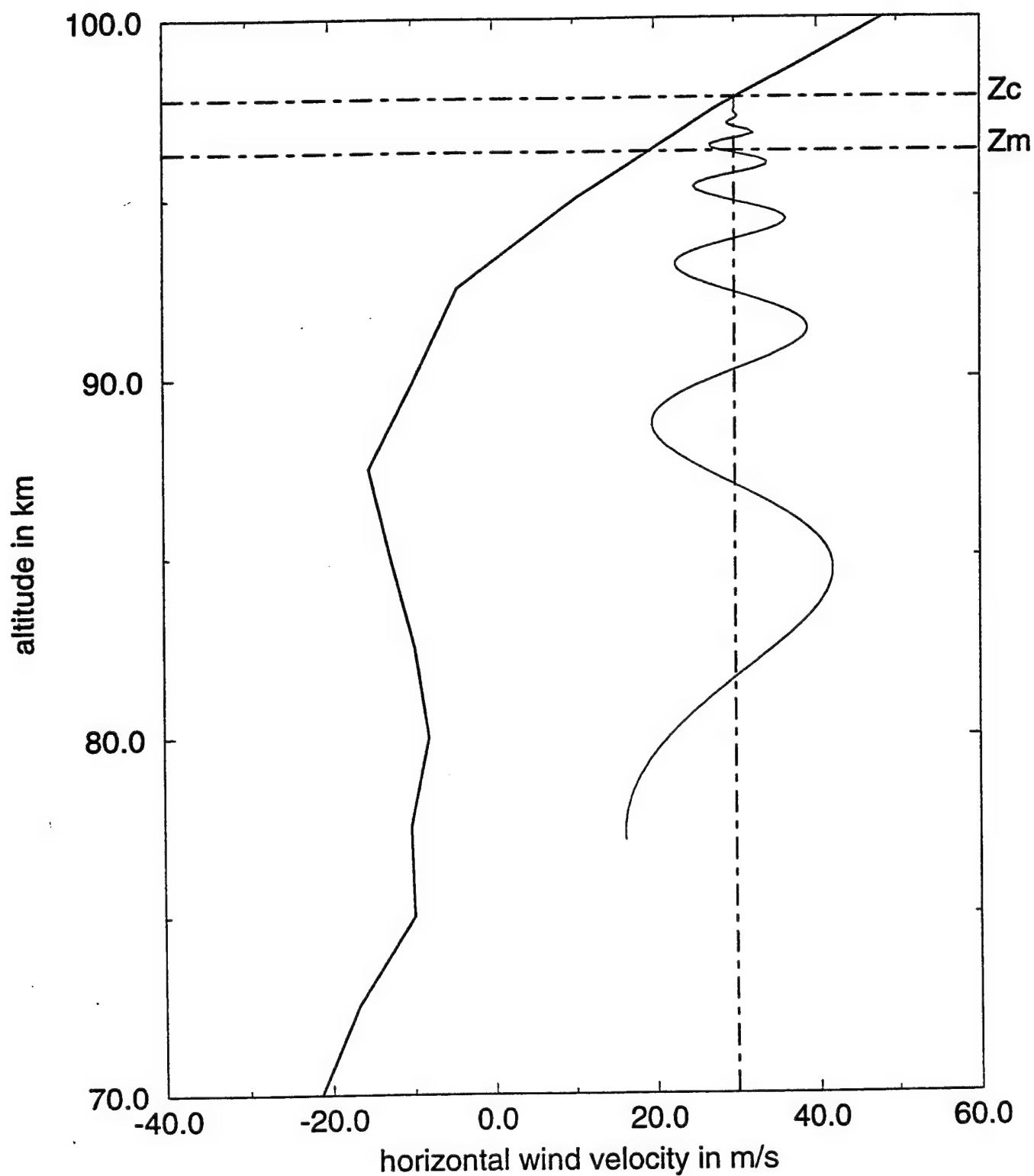


FIGURE 8

hydrogen density profile

T=15min, Vx=30m/s, a=50

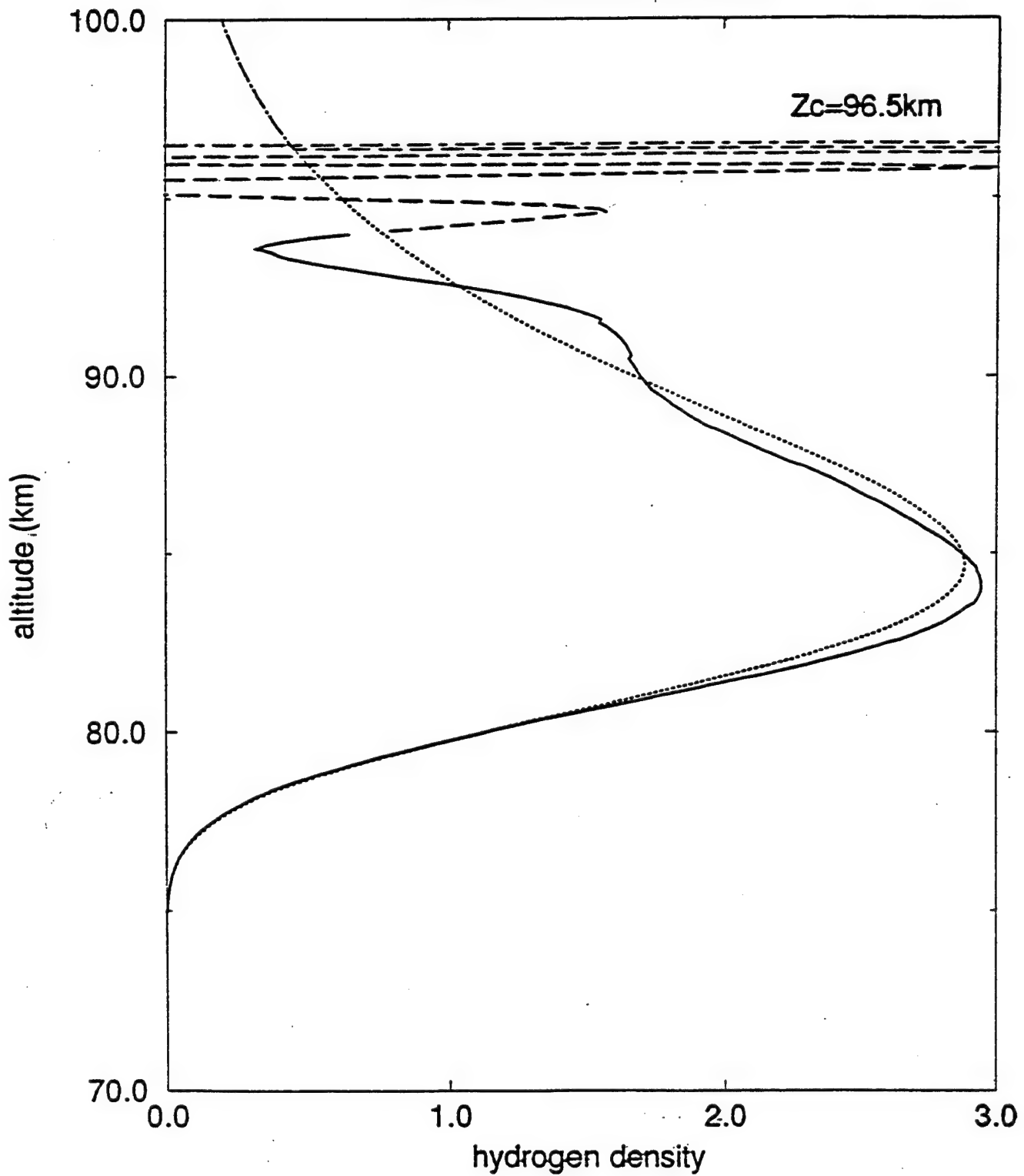


FIGURE 9

Wind for Colorado at Local Midnight ($\odot = 0$)

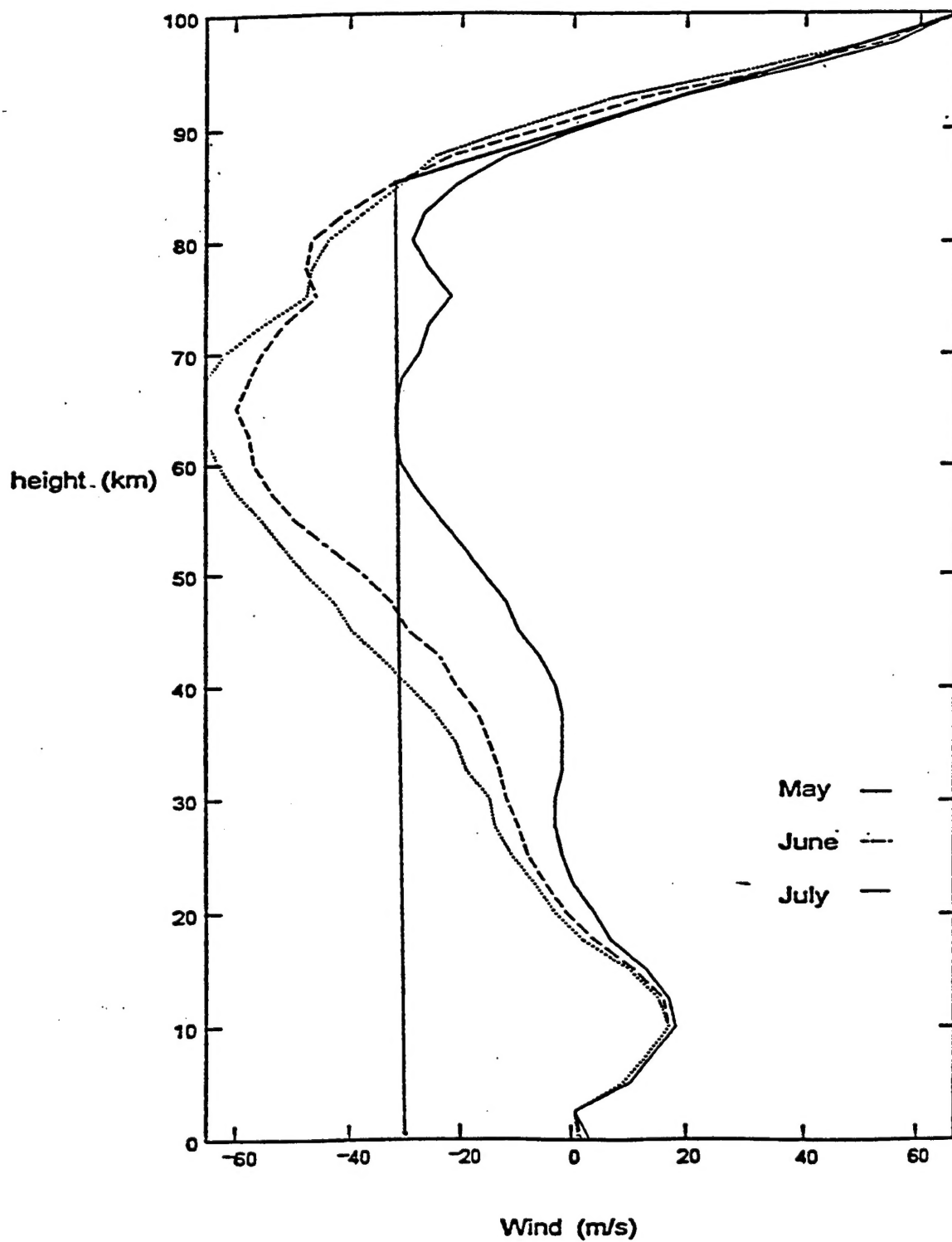


FIGURE 10

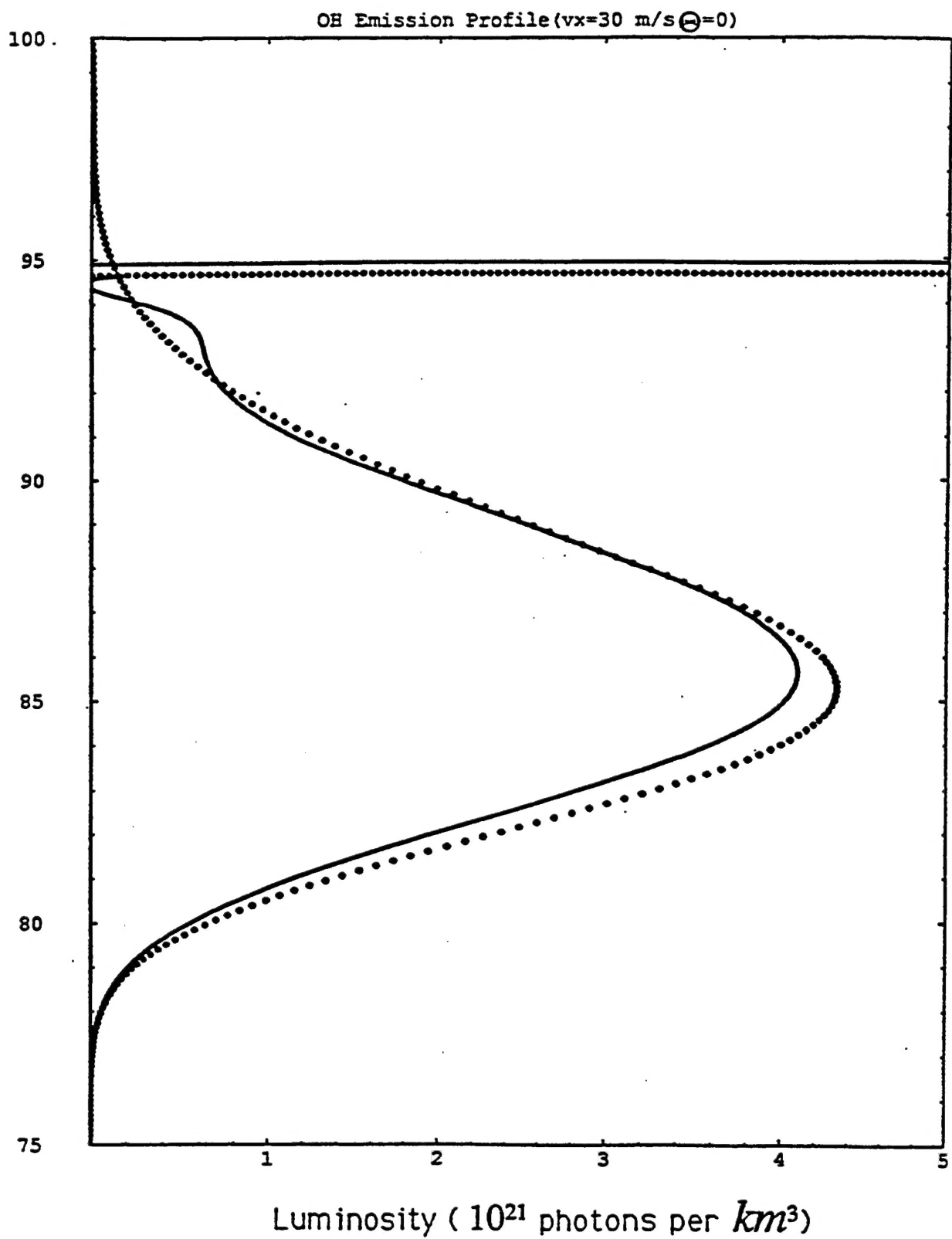


FIGURE 11

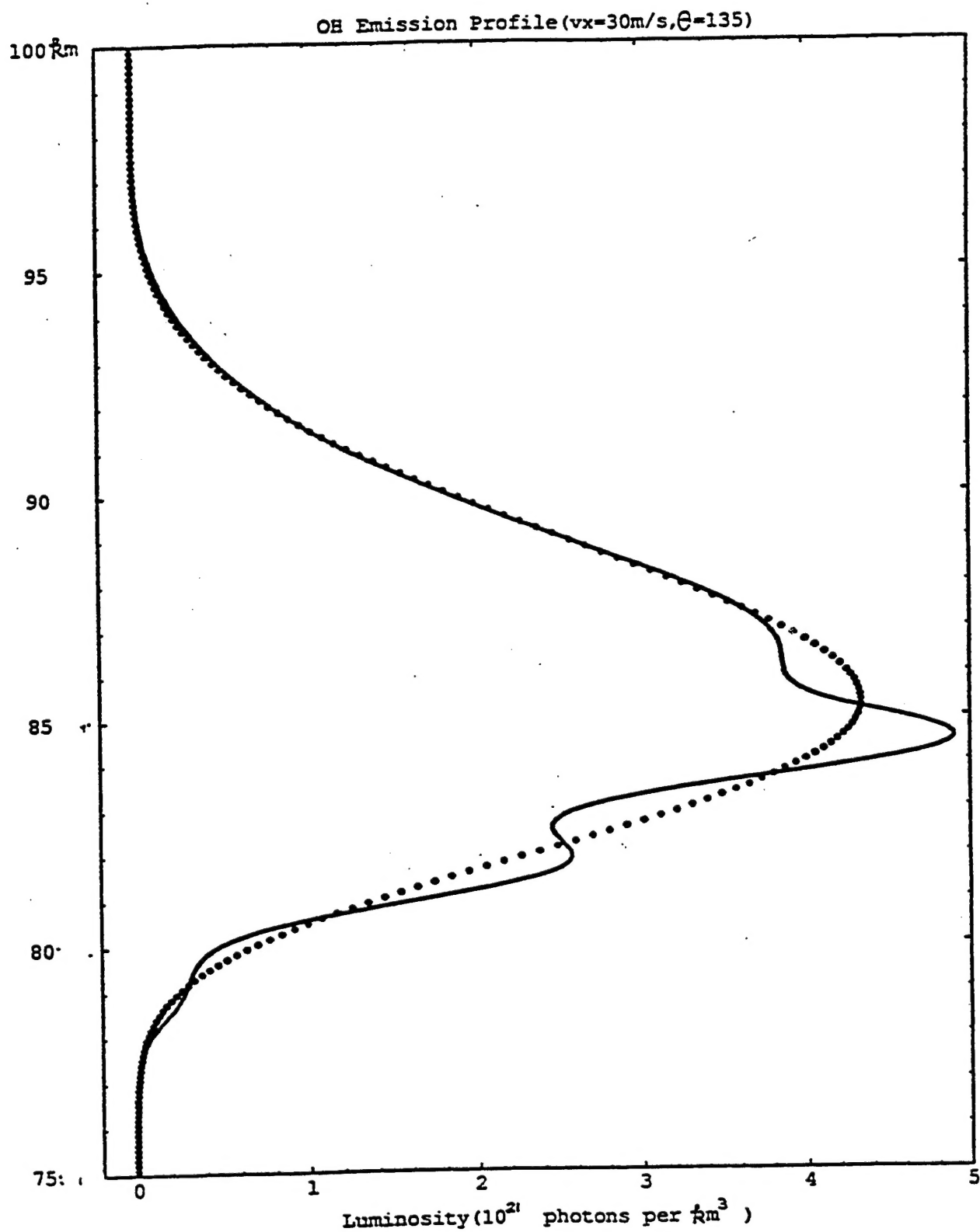


FIGURE 12

Generic profile

T=30 min $V_x=70$ m/s

Z (km)	Without Wind			With Wind		
	Wd1/Wz	Wd2/Wz	$\frac{Wd1+Wd2}{Wz}$	Wd1/Wz	Wd2/Wz	$\frac{Wd1+Wd2}{Wz}$
86	17.8%	0.7%	18.5%	16.5%	0.7%	17.2%
87	8.0%	0.7%	8.7%	7.0%	0.8%	7.8%
88	3.7%	0.8%	4.5%	3.5%	0.9%	4.4%

Hydrogen

T=30 min $V_x=70$ m/s

Z (km)	Without Wind			With Wind		
	Wd1/Wz	Wd2/Wz	$\frac{Wd1+Wd2}{Wz}$	Wd1/Wz	Wd2/Wz	$\frac{Wd1+Wd2}{Wz}$
80	3.5%	0.4%	3.9%	3.2%	0.5%	3.7%
81	2.6%	0.4%	3.0%	2.4%	0.5%	2.9%
82	1.4%	0.5%	1.9%	1.3%	0.5%	1.8%

TABLE I